Master of Science Thesis

Characterization of junction flow under the influence of passive flow control devices
An experimental study with large-scale tomographic PTV technique

Ka Hin Yeung

November 23, 2017

Aerodynamics

TU Delft

Characterization of junction flow under the influence of passive flow control devices

An experimental study with large-scale tomographic PTV technique

Master of Science Thesis by

Ka Hin Yeung

to obtain the degree of Master of Science in
Aerospace Engineering at Delft University of Technology,
to be defended publicly on Thursday November 23, 2017 at 02:00PM

An electronic version of this thesis is available at http://repository.tudelft.nl/
Thesis Registration Number: 178#17#MT#FPP

TUDelft

Delft University of Technology

Preface

It has been already two years since I set foot in Delft for the first time. During this times of my master I have learnt the the most important concepts in Aerospace Engineering. And now it is time to say goodbye and set out on a new journey.

This research project finalises my master program in Aerospace Engineering: Flight Performance and Propulsion in the Delft University of Technology. During this research period, I had the opportunity to work within the field of my interest in experimental aerodynamics, not to mention the experience of operating at the front-line with the latest PIV technology. I would like to thank my supervisors Dr. Andrea Sciacchitano and Ir. David Faleiros for proposing such interesting topic and the guidance that I received during this research period. Also a special mention to all technical staffs in the Aerodynamics Labs., Nico van Beek, Frits Donker-Duyvis, Peter Duyndam, Dennis Bruikman, Leo Molenwijk and Stefan Bernardy, who gave me invaluable advices for my experimental setup.

My warm regards goes to all the friends and company that I got during the times working in the legendary basement, sharing hours long studies, joyful moments with the sincerest laughter and encourages during the tough days.

Lastly and most importantly, I wish to express my greatest gratitudes to my family for supporting me far away from where I am, telling me to not give up no matter what and the sun always rises again tomorrow, without whom I would not be standing here today as an Engineer.

Ka Hin Yeung
Delft, November 2017

Abstract

Junction flow denotes the fluid phenomenon where the flow on a flat surface encounters a protuberance. This type of flow, which is highly three-dimensional, turbulent and unsteady, usually leads to the generation of a Horseshoe vortex at the obstacle's leading edge. Existing extensive experimental and numerical studies focus on the inception of such vortex, as it exhibits a bi-stable behaviour which persists downstream in the vortex legs. In a practical situation such as wing-fuselage juncture, the created vortex interacts with the flow around the aircraft. Consequently, the interference drag increases and the wake can reduce the effectiveness of the stabilizers. To tackle these effects, control devices are implemented to alleviate the strength of the vortex, being leading edge fairing the most widely used device.

In this research project the junction flow is subjected to the influence of different control devices: leading edge fairing, vortex generators and the novel antifairing are tested. The flow field is captured with the state-of-the-art large-scale tomographic PTV technique. The aim of this project is to characterize the vortical structures associated with each passive control device.

The time-averaged flow field results show the fairing is the most efficient device in reducing the presence of the Horseshoe vortex, but it is also the one which contaminates a larger wake area with the vortex wake. The vortex generators are the worst performer both in the mitigation of the vortex and the turbulence level in the wake. Nevertheless, the performance of such control devices highly depends on the location of the vortex generators. Thus, it is speculated that an optimal position exists which can yield better results. The antifairing shows minimal differences in the velocity field and the vortical structures compared with the reference case, but with a slightly lower turbulence level.

An auxiliary experiment with stereoscopic PIV is performed to the wake of the junction, in which the momentum deficit, a good indicator of the drag, is calculated for the different configurations. The leading edge fairing shows minimal drag reduction associated with the HSV of just about 1-2%. The VG once again have proven not being very effective with an increment of 4%. A reduction of more than 15% is measured for the antifairing case. Although the associated flow topology assimilates to the reference case.

This study investigates the HSV system around the junction as a volume. In comparison with most of the previous experimental studies on the subject, performed mostly with planar PIV

and limited to just a few planes, the volumetric measurement can deliver more information with a single measurement. Therefore, it can better define the flow topology and vortical features and facilitate the understanding of the control devices working mechanisms.

Table of Contents

List of Figures

List of Tables

Nomenclature

Abbreviations

BF	Bluntness Factor
HFSB	Helium Filled Soap Bubbles
HSV	Horseshoe Vortex
IPR	Iterative Particles Reconstruction
LOLS	Line Of Low Shear
MDF	Momentum Deficit Factor
OTF	Optical Transfer Function
PIV	Particle Image Velocimetry
PTV	Particle Tracking Velocimetry
sPIV	Stereoscopic Particle Image Velocimetry
STB	*Shake-the-Box*
tomo-PIV	Tomographic Particle Image Velocimetry
tomo-PTV	Tomographic Particle Tracking Velocimetry
VG	Vortex Generator

Greek Symbols

δ	Boundary layer thickness	mm
δ^*	Boundary layer displacement thickness	mm
δ_z	Depth of View	mm
$\epsilon_x, \epsilon_y, \epsilon_z$	Uncertainty of the principal components of velocity	m/s
Γ	Circulation	m^2/s
μ	Dynamic Viscosity	$Pa \cdot s$
ω	Vorticity	s^{-1}
ρ	Density (fluid)	kg/m^3
ρ_p	Seeding particles density	kg/m^3
$\sigma_x, \sigma_y, \sigma_z$	Standard deviation of the principal components of velocity	m/s
τ_p	Seeding Particles Relaxation Time	s
θ	Boundary layer momentum thickness	mm

θ_x, θ_y	Camera pitch and yaw angle	deg

Latin Symbols

C	Particles concentration	$bubbles/mm^3$
d_i, d_o	Distance to image and object	mm
f	Focal length	mm
f	Frequency	Hz
$f\#$	F-stop number	mm
H	Boundary layer shape factor	-
l	Bin cell length	mm
MD	Momentum Deficit	$kg \cdot m/s^2$
N_{un}, N_{eff}	Number of uncorrelated and effective samples	-
Q	Q-criterion vortex identification method	s^{-1}
R_0	Wing model leading edge radius	mm
R_{xx}, R_{yy}, R_{zz}	Principal components of Reynolds stress	m^2/s^2
Re	Reynolds number	-
Re_θ	Reynolds number based on momentum thickness	-
Re_c	Reynolds number based on wing model chord	-
Re_T	Reynolds number based on the wing model maximum thickness	-
$Re_{\delta*}$	Reynolds number based on displacement thickness	-
S_T	Wing model leading edge nose perimeter	mm
St	Strouhal number	m/s
t	Time	s
U_∞	Freestream velocity	m/s
X_T	Chordwise distance to the maximum thickness	mm
AoA	Angle of Attack	deg
AOV	Angle of View	deg
c	Wing model chord	mm
DOV	Depth of View	mm
FOV	Field of View	mm
h	Wing model span	mm
M	Magnification factor	-
T	Wing model maximum thickness	mm
U, V, W	Principal Components of Velocity	m/s
x, y, z	Streamwise, spanwise and normal direction to the wing model	mm

Chapter 1

Introduction

Junction flow is a common fluid dynamic phenomenon which can be found in numerous engineering applications. It occurs immersed in a flow where a protrusion is placed on a flat surface. Besides, the outcome of its presence also affects the performance of the engineering design.

Some of the common applications where junction flow is encountered are bridge foundation pier and attachment between wing and fuselage of aircraft. In the first case, the riverbed of the pier deteriorates from the continue scouring motion of vortices generated in the junction area. As a result, more portion of the pier is exposed and could lead to catastrophic failure if left unattended. According to Shukri (2017), scour is a potential cause for up to 60% of bridge failure in the United States. On the other hand, the highly turbulent nature of the junction flow causes additional interference drag to aircraft. Additionally, the unsteadiness of such flow is responsible of a reduction in aircraft stability as well.
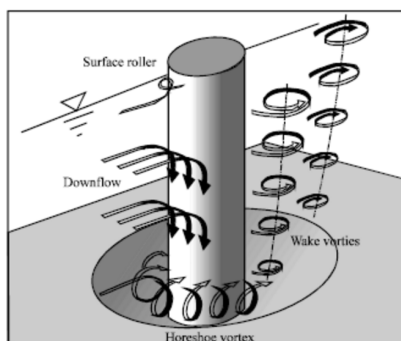
Figure 1.1: Flow and scour pattern of a cylinder pier (Melville and Coleman, 2000).

Figure 1.2: Oil flow visualization of DLR F6 model at wing-fuselage junction (Rudnik et al., 2009).

Besides, the turbulent flow also enhances the heat transfer rate, for this reason it is becoming more noticed in the field of microelectronics. Because electronic modules are every time more compact but become susceptible to heating, whilst traditional heat sink for cooling is no

longer an optimum solution in this micro-system. Hence, cooling system by direct blowing the components is essentially a junction flow.

Because of the large number of applications where junction flow is involved, such kind of flow has been studied extensively in the last few decades. Up to today, this topic is still being investigated to further understand the working mechanisms of junction flows and to learn how to control them.

1.1   Junction Flow

The interest toward junction flow is related to its complexity. In normal conditions, the flow on a flat plate can be simplified as two dimensional. However, when a protuberance is placed on the plate, the velocity field around the object becomes highly three dimensional. In the upstream position of the junction, the boundary layer undergoes a three dimensional separation due to the strong adverse pressure gradient at the union point.

When separation occurs, the shear layer rolls up to form a vortex at the base of the obstacle. In combination with the incoming flow, the vortex is swept down. The shape of the vortex view from above assimilates to a horseshoe, hence it is often called horseshoe vortex(HSV) (Baker, 1978b). According to Bradshaw (1987), the HSV is classified as secondary flow of the first kind by Prandtl's theory. In other words, the vortex is created by the deflection or skew of the existing vorticity upstream of the wing. Such kind of flow is diffused by turbulent and viscous stress.
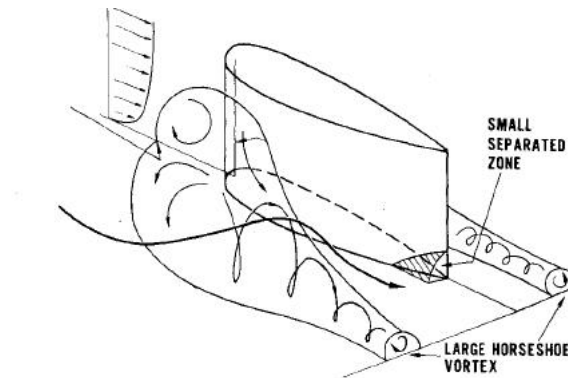
Figure 1.3: Sketch of junction flow (Barber, 1978).

The shape of the horseshoe vortex is shown in figure 1.3. Another feature of junction flow is a corner separation which occurs at the rear region of the obstacle (marked as separated zone). The corner vortex is caused by the gradient in Reynold stresses. Stated otherwise, it is a secondary flow of the second kind in Prandtl's theory or known as stress-induced secondary flow, as suggested by Gessner (1973). Compared to skew induced vorticity, stress-induced flow can only happens in turbulent flows and generally is much weaker.

Although the main separation point is in the corner region (especially in aerodynamic config-

urations), most studies done so far are focused in the horseshoe vortex which appears at the upstream section (Gand et al., 2012).

1.1.1 Horseshoe Vortex

The apparition of HSV system can occur in both laminar or turbulent flow. Although the vortex structure is similar in both cases, the turbulent vortex system is generally simpler, as concluded by Baker (1978b).

Laminar Horseshoe Vortex The laminar HSV system was first investigated by Schwind (1962) using smoke visualization technique, but it was Baker (1978b) who studied the case with quantitative pressure and velocity measurement on a cylinder placed on a flat plate. In Baker's finding, he classified the HSV system into three regimes: steady, oscillating and turbulently unsteady.
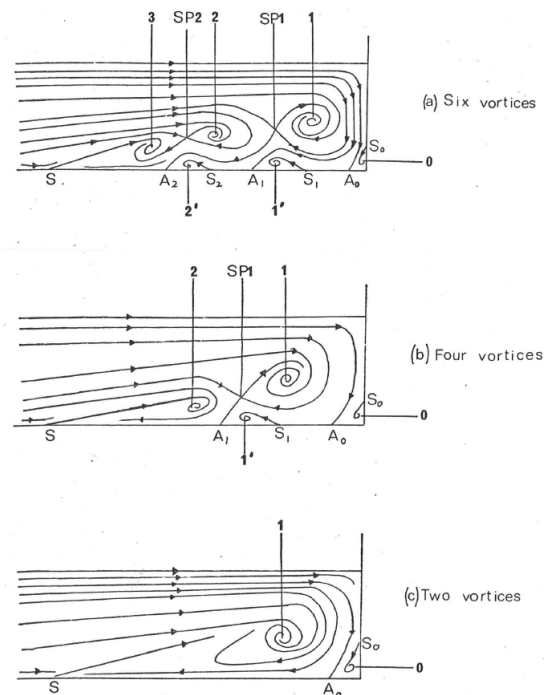
Figure 1.4: Side view of different Horseshoe vortex systems. The numbers denote the vortex present in the system; S, the separation saddle point; SP, the stagnation points and A, the attachment point (Baker, 1978a).

In the steady system at Reynolds number around Re=270, an almost unnoticeable and weak vortex is formed by the separated flow from the obstacle surface, marked as 0 in figure 1.4. This vortex is also called as corner vortex. As the Reynolds number increases, a single steady clock-wise rotating vortex emerges (called vortex 1 in figure 1.4 or main vortex). For higher freestream velocity, hence Reynolds number, a second pair of vortices appears, also a third if the velocity is sufficiently high. The reason for the vortices to appear in pairs is due to the

need of continuity in the velocity gradient. In addition, for a given Reynolds number, the number of vortex systems varies with the obstacle size.

When the Reynolds number is further increased, at approximately Re=2500, the HSV begins to oscillate. In this regard, the main vortex closest to the protuberance moves forth and back in the streamwise direction. The oscillating movement is followed by the other vortices as well. For even higher velocity, the vortex system appears to be turbulent.

Baker (1992) suggested the apparition of a second or third vortex system is the result of the primary vortex core instability with increasing Reynolds number. Such instability causes the vortex to break down into multiple more stable vortices up to a limit of three. The limited number is due to the lack of space in the confined junction region to house additional vortices. Hence the entire vortex system becomes unsteady after this point.

Regarding the topology of the presented vortex systems, it was thought in the early stage that the organization of vortices follows the stair-step mode, see figure 1.5 a. However it was later updated with further investigations. Note the new arrangement does not substitute the previous one, instead, one could transition to another under certain conditions. The new vortex structures were first found by Norman (1972), in which the structures differ slightly (see figure 1.5 b and c).

(a) Stair-step mode   **(b)** Jet maze mode   **(c)** Alternative mode
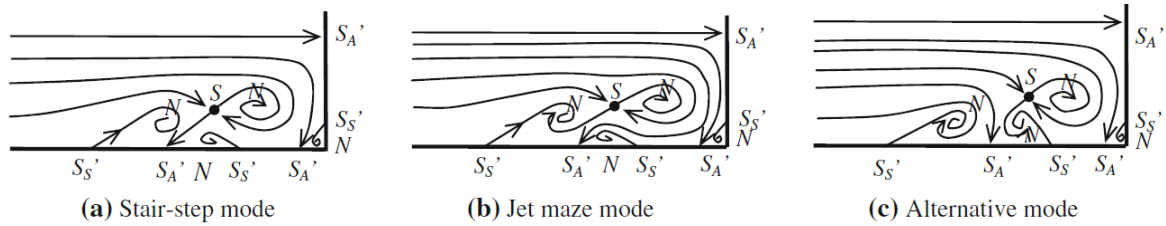
Figure 1.5: Conventional separation saddle point topology for four vortex system (Zhang et al., 2012).

Nevertheless, new discoveries from Visbal (1991) revealed another topology through his numerical calculations. The results suggest the most upstream separation saddle point is not a separation, but an attachment saddle point (shown in figure 1.6 a). Other numerical simulations performed by different authors in later years also presented an attachment saddle point (Hung et al., 1992), as well as in some experimental studies (Coon and Tobak, 1995).

In recent years, Zhang et al. (2012) conducted a measurement with Particle Image Velocimetry (PIV) technique to further investigate the topology. Two more attachment modes were discovered and are structurally similar to the "Jet maze" and "Alternative" modes found in separating vortex system (see figure 1.6 b and c). Furthermore, the most upstream singular point is actually a node[1] rather a saddle point[2] in flow attaching topology.

To emphasize, Wang et al. (2010) had proven all the aforementioned topologies do not deny

---

[1]Singular point where streamlines in the symmetric plane diverge from it.
[2]Singular point where streamlines in the symmetric plane converge towards it, but diverge in the plane normal to the streamwise direction.

(a) Attachment topology A   **(b)** Attachment topology B   **(c)** Attachment topology C
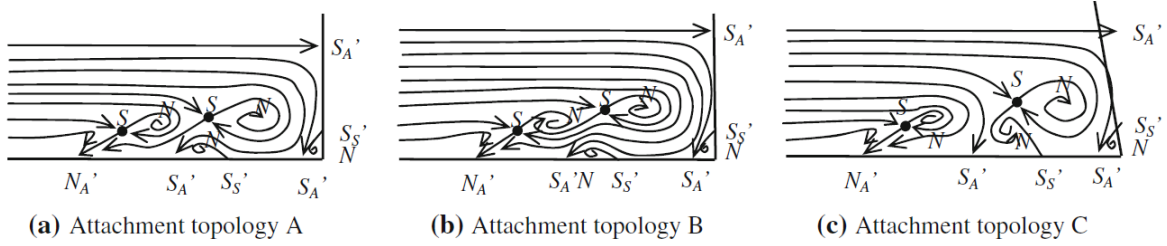
Figure 1.6: Attachment node point topology for four vortex system Zhang et al. (2012).

the existence of the others. In his numerical study, he managed to compute the evolution of laminar HSV which transitions from one type of singular point to another. Years later, the same results were obtained experimentally by Younis et al. (2014). All these species can exist, but some of them are rarely seen in reality and only can be reproduced in a limited range of flow conditions. Nevertheless, all these structures fulfil the Hunt's (Hunt et al., 1978) equation for singular topological rule:

$$\left(\sum N + \frac{1}{2} \sum N' \right) - \left(\sum S + \frac{1}{2} \sum S' \right) = 0 \tag{1.1}$$

The Hunt's equation, N refers to the number of nodes and foci (vortex cores) and S the number of saddle point. The prime notation implies the half node or saddle points, meaning that the streamlines which interact with the singular point are not symmetric in the plane of symmetry.

The transition from separating singular point to attachment point strongly depends on the ratio of boundary layer thickness and obstacle width. A higher ratio gives place to the presence of an attachment node and it transforms to a separation saddle point as the value decreases. In addition, an attachment point is more likely to occurs in a blunter model, as stated in the study of Hu et al. (2015).

Turbulent Horseshoe Vortex   In the investigation of Baker (1978b), he also studied qualitatively the turbulent HSV flow with oil-flow visualization. With this technique, the averaged flow field was captured, shown in figure 1.7. The flow upstream of the protuberance first encounters a primary saddle point or point of flow separation. A second (secondary) saddle point can be distinguished downstream of it. In between the saddles points, an attachment point must take place, otherwise the flow cannot separate a second time. The separation and reattachment of the flow around the cylinder can be recognised by the lines that run through the saddle points. Additionally, the flow immediate to the leading edge of the obstacle separates and reattaches close to the floor, marked as A_0 in the figure. As a result, it creates a corner vortex. The proposed topology is similar to the four vortex system in the laminar HSV.

Later on, Devenport and Simpson (1990) proposed another explanation for the case. The supposed second separation line from Baker is in fact a line of low mean wall shear (LOLS). Although a considerable amount of pigments accumulate, it is not a separation line because the oil streaks can pass through it. In such case, the line of low shear separates the flow into
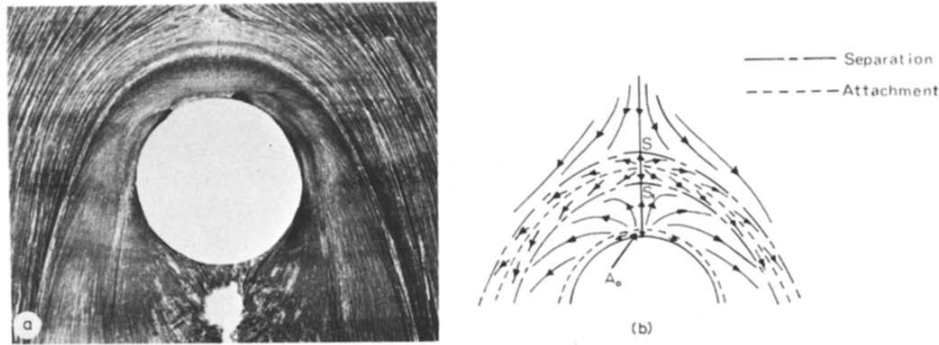
Figure 1.7: Flow around a cylinder-flat plate a) Oil-flow visualization b)Sketch of the flow streamline (Baker, 1980).

two regions: a high surface shear stress in the proximity of the obstacle and a low surface shear upstream of the line. This explanation was later supported by numerical simulations done by Paik et al. (2007) and Escauriaza and Sotiropoulos (2011).

The explanation for the high wall shear stress in the downstream region of the line of low shear was given in another study from Devenport and Simpson (1990). The large shear stresses are associated with the fluctuating velocity in this region. As stated by the authors, the fluctuation follows a bimodal behaviour. Briefly explained, the velocity fluctuation oscillates between two stable position. More details are explained in 1.1.2.

According to Coon and Tobak (1995), the attachment nodes topology of vortex structure could also appears in turbulent junction flow or even in high-speed flow. However, a limited number of studies exist regarding the separation-attachment transition in such condition.

1.1.2 Bimodal behaviour of HSV

The bimodal behaviour concept of horseshoe vortex was first introduced by Devenport and Simpson (1990). This concept defines a vortex does not reside in a stable stationary position but oscillates between two preferred positions. It is also referred as modes by the authors. The bimodal behaviour characteristics were evaluated experimentally through measurements with a three component laser Doppler velocimeter (LDV). Compared to the previous mentioned methods, this technique allows a relatively high acquisition frequency to the velocity measurement non-intrusively. Such method solves the problem back in the experiments of Baker (1978a), where the hot-wire probe caused the vortex system to oscillate irregularly when it was close to the vortex core.

The bimodal behaviour can be identified through multiple probability density function (PDF) across different heights at the mean streamwise position of the HSV core, see figure 1.8. At certain heights, the probability plots present a double peak feature. This phenomenon implies the velocity has two preferred states at that particular position, also referred as bistable behaviour. The two states are named as back-flow mode and zero-flow mode. The right peak
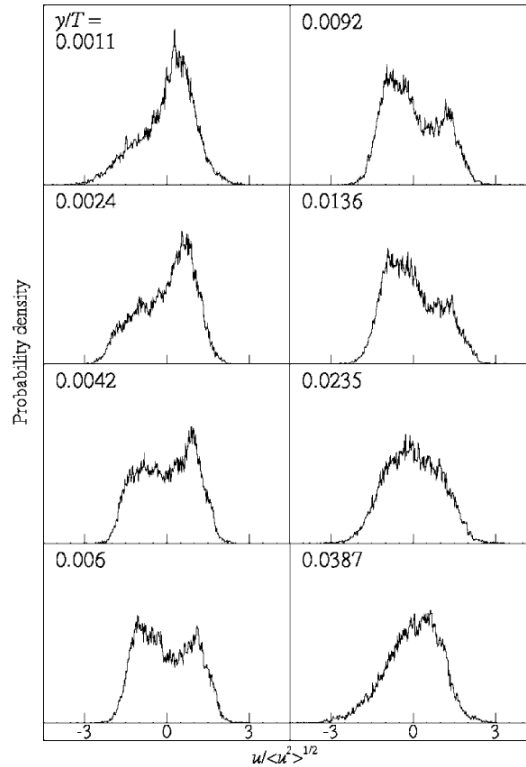
Figure 1.8: PDF of streamwise velocity at mean HSV core streamwise position (Paik et al., 2007).

of the PDFs corresponds to the probability of occurrence of zero-flow mode. It appears as positive due to the subtraction of the mean velocity, but the instantaneous velocity tends to take the value of zero. Similarly, double peak PDFs can also be observed for spanwise velocity. Apart from the two most extreme cases, an intermediate mode is also defined when the flow structure switches from one extreme mode to another.

Back-flow mode is characterize by a "jet flow" between the main vortex and the flat surface, moving against the upcoming freestream flow. Zero-flow is identified when the "jet flow" has lower momentum. Hence it does not have enough energy to flow upstream against the approaching flow but combines with it and is redirected upward. Sketch of both flow modes are shown in figure 1.9.

In the time-resolved study performed recently by Apsilidis et al. (2015) in different Reynolds condition, it shows the zero-flow mode and the intermediate mode present most of the time, while the back-flow mode occurs with less frequency. Also, the authors have included a certain portion of time the HSV structure is so chaotic that does not allow the identification of neither. With increasing Reynolds number, the time occupied by back-flow mode increases with decaying frequency of zero-flow mode.

Nevertheless, the new research also suggests the flow modes and the location where they occur are not correlated, which is contrary to the previous literature. This conclusion can be drawn

with results from surface measurement technique of PIV. This technique allows an almost direct visualization of the instantaneous velocity field; while in the classical literatures, it relies on an indirect measurement with point-wise probe and the time average in each position.

The different modes flow structures are shown in figure 1.9, which is obtained with PIV measurement. In classical studies, the position of the main vortex in the zero-flow mode was thought to be closer to the protuberance than back-flow mode. However, the results shown prove it is not strictly true.

In addition to Apsilidis, Chen et al. (2017) also investigated the multi-modal dynamics of the turbulent HSV system with planar PIV technique, but in low Reynolds number regime. Their study was focused in the transition mechanism between modes and also the time occupied by each in the measurement period.
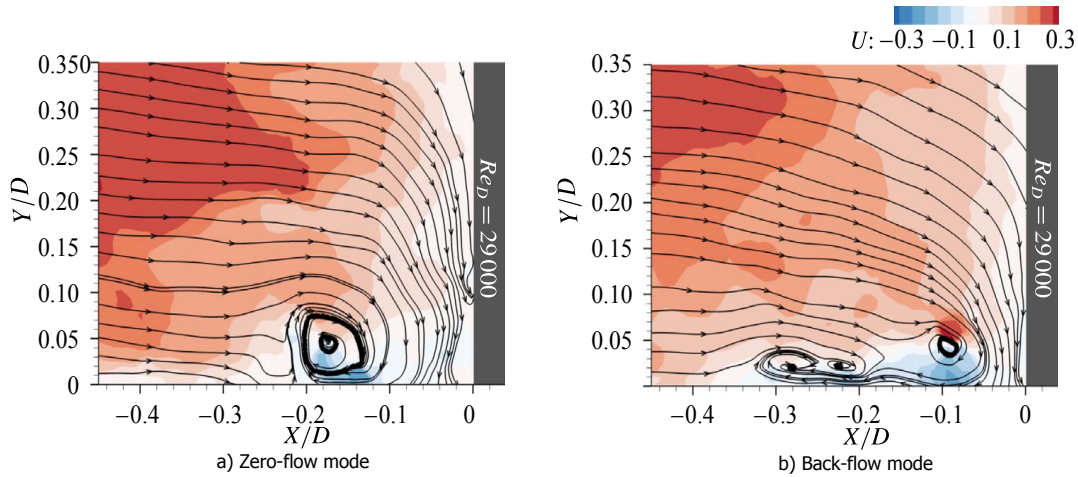
Figure 1.9: Contour plot of streamwise velocity at different flow modes in junction flow Apsilidis et al. (2015).

1.1.3 Horseshoe vortex leg and wake

The HSV system originates in the upstream of the symmetric plane. Later on, the vortex legs stretch around the protuberance and convect downstream. The HSV in the front region and its bimodal behaviour are well-studied. However, the dynamics and properties of the vortex legs have been given less attention.

It is logical to think the vortex legs have similar dynamics as the leading edge HSV. Fleming et al. (1993) studied the time-averaged velocity in multiple cross-section plane of a wing-flat plate model. The authors found the vortex legs have a meandering effect, whose intensity decreases downstream. Such effect is reflected as an elliptical vortex core in the time-averaged vorticity, and becomes more circular with increasing streamwise position. This behaviour is suggested to be intimately related to the bimodal behaviour, as its oscillating strength decay with distance. A similar trend can be observed in the numerical study performed by Fu et al.

(2007), figure 1.10.

Gand et al. (2010a) had performed a spectral analysis between the bimodal behaviour of the main HSV and the meandering effect in a later numerical study. On the first observation, the meandering frequency is lower than the bimodal frequency. For this reason a further spectrum cross-correlation was performed by the authors. They suggested that the meandering effect in the transverse direction is indeed triggered by the bimodal behaviour. Nevertheless, the meandering frequency does not match with the bimodal frequency. It is due to the degeneration of the bimodal pulsation, which becomes more bandwidth further downstream.
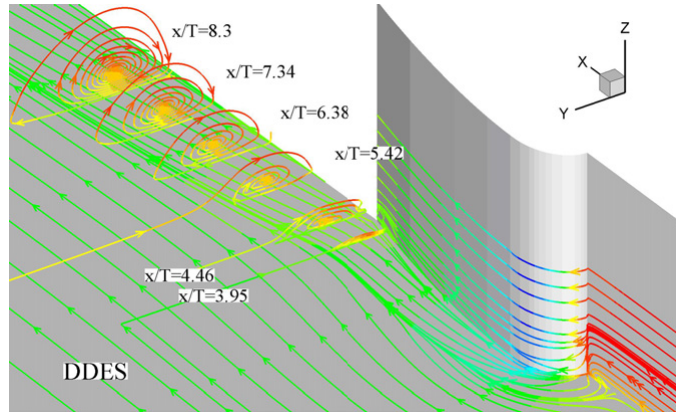
Figure 1.10: Shear stress lines and vortex in the wake of a wing-body junction (Fu et al., 2007).

From figure 1.10, the wake resulted from the vortex leg appears to grow in size and move away from the wing. This change is primarily due to the vortex induced velocities. Additionally, the growth rate depends on the growing of the boundary layer. For instance, if the vortex wake encounters an adverse pressure gradient, the core would grow faster but its peak vorticity decreases (Fleming et al., 1993). Hence, the presence of an adverse pressure gradient favours the diffusion of the vortex legs wake.

1.1.4 Influence Parameters

Since Schwind (1962) pioneered the investigation towards junction flow, numerous studies were conducted by different authors. In addition, the shape of the obstacles subjected to the studies were not limited to simple geometry such as cylinders or wedges, but also to a more practical shape such as airfoils.

In order to correlate the shape of obstacle and their vortex stretching rate (length of the horseshoe vortex), Fleming et al. (1991) proposed a *bluntness factor* (BF) which yields a good representation for obstacle geometry, defined as:

$$BF = \frac{1}{2}\frac{R_0}{X_T}\left(\frac{T}{S_T} + \frac{S_T}{X_T}\right) \tag{1.2}$$

From the equation of BF, R_0 denotes the protuberance leading edge radius, X_T is the chord-wise position of the maximum thickness T of the model and S_T is the distance from the

leading edge along the surface to the maximum thickness, in the case of a cylinder it would be a forth of the perimeter. In the same experiment, the authors found a high value of BF implies a strong and long HSV. This discovery is consistent with Bradshaw's explanation, where for sharp leading edges, hence low BF, the concentrated vortex can get closer to the surface which is then diffused rapidly by viscous or Reynolds stresses (Bradshaw, 1987).

Another parameter was also proposed, named *momentum deficit factor* (MDF). This parameter relates the momentum difference between the inner and outer boundary layer regions. In this matter, for a given high MDF value, a more intense turbulent structure is present close to the wall, as the higher momentum flow tends to flow towards the lower undistorted flow.

$$MDF_x = Re_T \cdot Re_{\theta_x} \tag{1.3}$$

The MDF is equal to the product of the Reynolds number based on the obstacle width and momentum thickness at the measured streamwise position. The MDF is especially useful to compare the HSV dynamics of different studies with various geometry and flow condition. However, since part of the dynamic is associated to the incoming boundary layer thickness, it is usually found the use of Re_{θ_x} is preferred to define the HSV as long as the working geometries remains the same. For this reason, Gand et al. (2010a) opted for the use of Re_{θ_x} in a junction flow study of a NACA0012 to classify different behaviours regimes: for $Re_{\theta_x} \leq 100$, the horseshoe vortex is steady. As the Re_{θ_x} increases up to 1500, the HSV starts the forward and backward motion (bimodal behaviour or modes as reported by Devenport and Simpson (1990)) which is periodic with a transition frequency of 0.05 Strouhal number based on the boundary layer thickness:

$$St_\delta = \frac{\delta \cdot f}{U_\infty} \tag{1.4}$$

δ defines the boundary layer thickness, f is the transition frequency of the HSV and U_∞ the freestream velocity.

The flow becomes more turbulent for even higher Reynolds number. The bimodal behaviour becomes more chaotic and the transition frequency presents a large bandwidth from $St_\delta = 0.001 - 0.11$.

Apart from the aforementioned dimensionless parameters, which defines the geometry of the protuberance and incoming flow boundary layer properties, additional geometrical parameters could affect the strength of the vortices. In an annual review of fluid mechanics (Simpson, 2001), Simpsons mentioned the effect of angle of attack (AoA) and sweep. When a wing with a certain angle of attack is placed on a flat plate, the approaching flow encounters an artificial nose blunter than at zero AoA. As a result, a stronger HSV is generated. In addition, the suction side of the wing suffers from a higher shear stress and turbulent kinetic energy due to the increase in velocity; whilst the leg of the HSV is shifted away from the wing. In terms of the sweep, in back-sweep wing configuration, the HSV head moves downstream and causes the time-averaged separation line to be closer to the wing, an opposite effect was observed in forward-sweep configuration. In the study by San et al. (2014), it shows the Reynolds stress is higher for a backward-sweep and lower in forward-sweep position. This occurring is maintained even the wing is positioned in a certain angles of attack.

1.2 Vortex control

It has been discussed the generation of horseshoe vortex in wing-body junction has usually undesired effect on aerodynamic performance. For instance, the vortex causes additional interference drag on aircraft and the wake is more turbulent, hence it reduces the stabilizer effectiveness. Facing this condition, the aim to reduce or eliminate these outcomes could be achieved by modifying the vortex structures and the surrounding flow field.

1.2.1 Passive control

The vortices and flow separation generated in the junction region are caused by the strong adverse pressure gradient derived from the blunt nose of the protuberance. As consequence, intense velocity fluctuation is resulted. A simple way to reduce the stagnation pressure is by modifying the geometry in the junction region or implementing other elements to modify the flow field. These control methods are the so called passive flow control.

Leading edge fairings are extensions to the wing-fuselage root; their shape allows the transition of boundary layer from the fuselage plane to the wing plane to be more gradual. Such modification is also the most widely used in aviation nowadays, as it is simple and is effective in reducing the vortex strength and interference drag.

Figure 1.11: Picture of leading edge fairing on a commercial Boeing 747. Source:https://www.flickr.com/photos/a380spotter/

The application of fairing in a junction flow can reduce or even remove completely the pressure gradient in the junction. In return the leading edge separation is eliminated. However due to the concentration of vorticity the vortex legs are still formed (Devenport et al., 1992). Rudnik et al. (2009) performed an extended investigation to a DLR F6 model experimentally, whose results served as verification to numerical studies from the AIAA Drag Prediction Workshop with the same model. The frequency analysis from Rudnik has demonstrated the amplitude of the fluctuation is damped at the trailing edge region. Especially at the low frequency band.

Nevertheless, the geometry of the fairing also determines its effectiveness on the overall performance of an aircraft. For instance, during the first decades of aircraft design, the strake shape was defined by trial and error. While it did improve the stability of the vehicle, the total drag could not be reduced but worsened. Van Oudheusden et al. (2004) found a simplified method for fairing designs. Such method is based on attachment line and flow relaminarization. With this design method, the shape of the fairing is obtained from an optimization process, whose requirements are the absence of flow separation and the flow close to the wing root is as laminar as possible. The design had been proved to be viable in wind tunnel experiment with oil-flow visualization. However, no quantitative data was recorded. In later years, Hinson (2012) performed a parametric study with CFD of the wing sweep and strake length. His finding suggested a longer strake is more effective in reducing drag to up to 20 counts compared to wing-flat plate along. Although the improvement is strongly reduced in a full aircraft simulations.
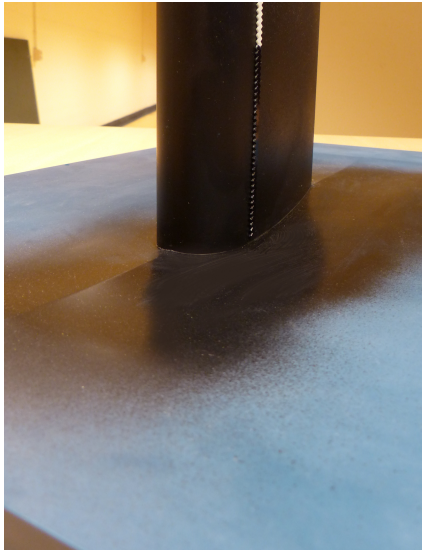
Figure 1.12: Antifairing plate with Rood wing model installed.

Antifairing is a novel design found by Belligoli (2015) in an optimization process of a Rood wing-flat plate junction, in which the flat plate shape was the factor subjected to the optimization routine. Such design assimilates to a dented surface or a scoured junction around the wing. The new prototype indicates a drag reduction of 15% with respect to the baseline CFD simulated case. Regarding the working mechanism of the antifairing, Belligoli speculated that the three-dimensional turbulent flow structure is confined inside the scoured region and does not disturb the airflow over it. An analogy can be found in a recent study on dimpled surface (van Campenhout et al., 2016). The authors had concluded in fact the drag is reduced in a dimple by reducing the strength of the legs of hairpins vortices. Koers (2017) found in a CFD calculation that the drag reduction mainly comes from the antifairing plate. Firstly, the wall shear drag is lower due the deceleration of the flow when it reaches the antifairing dent. Secondly a net negative pressure drag is recorded. However, the reliability of the existing experimental data for verifying the antifairing performance or the vortex structure is questionable.

Vortex generators could also reduce the strength of the horseshoe vortex. Andoh et al. (2009) employed two separated VG in common-up-flow configuration upstream to the leading edge. With this configuration, the generated vortex (longitudinal vortex) and the horseshoe vortex have opposite rotation. As a result, the HSV and global vorticity is reduced. However, this VG arrangement is highly dependent on the pair spacing, and the longitudinal vortex has higher influence on the vortex leg rather the head of the HSV. In view of this issue, Younis et al. (2015) proposed in the application of multiple pairs of VG without spacing in

the symmetric plane, one behind each other in series. With this design, the longitudinal vortices affects immediately the HSV. His results show the two pairs of VG configuration is the most effective in attenuating the strength of the nose of HSV, as the circulation strength remains to 5% of the baseline case.

(a) Pair of vortex generator in spacing configuration (Andoh et al., 2009).

(b) Two pairs of vortex generators in series configuration Younis et al. (2015).
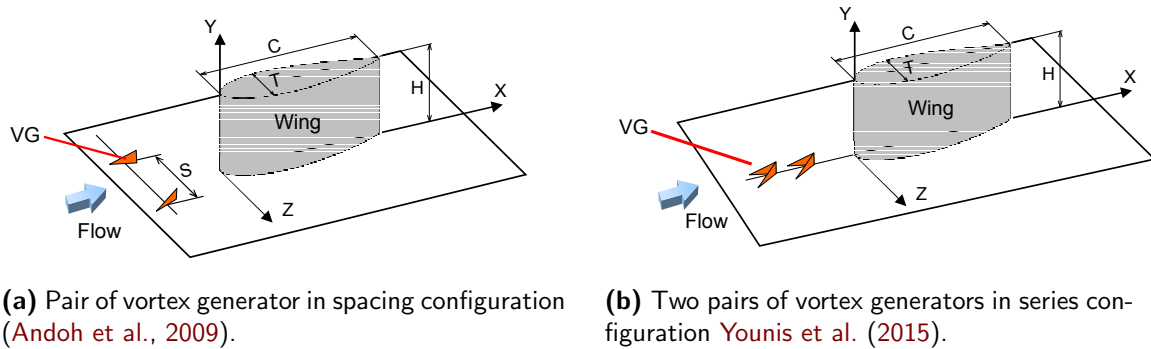
Figure 1.13: Vortex generator as HSV control

Other unconventional ideas were proposed by other authors. For example swept thin cylinder placed in front of the main obstacle (Wei et al., 2008), chamfer like leading edge fairing (Cho and Kim, 2009), or cavity in the upstream position of the junction (Kang et al., 2009). All modifications had shown to be able to reduce the strength of the HSV, but they might not be applicable in practical cases. It is due to the passive flow control devices are often designed for a specific operating condition, whose effectiveness are substantially reduced in off-design condition, such as different flow speed, AoA, cross-flow, etc.

1.2.2 Active control

Active flow control system is another approach for the manipulation of HSV. Compared to passive devices, active systems are more complex as they require external energy source to modify the flow field. Scott Collis et al. (2004) have stated that active flow control systems could be more effective than passive flow control if applied optimally. However, the knowledge in the working mechanisms is still immature. For this reason, the number of studies in HSV control with active system is limited.

Thrift and Thole (2012) conducted an experimental study of the influence of jet injection angle on HSV. The experiment consists of an air blowing slot placed in front of a linear van turbine cascade. He concluded that for an air jet, injected with high deflection angle with the flat surface, increases the turbulent kinetic energy and is accompanied by a larger vortex in the stagnation region. While for lower jet injection angle case, the HSV was effectively eliminated but at the same time the high momentum jet causes higher shear stresses on the plate and upwash flow on the obstruction leading edge.

Bloxham et al. (2008) considered the option of boundary layer removal. The design consists of a suction slot placed in the leading edge and close to the wall. The idea is that the suction slot can remove the adverse pressure gradient in the junction region. With this technique, the

HSV is removed effectively and prevent flow separation. However, an over-suction can have adverse effect and creates additional vortices, which strengthen with higher suction rate.

An even more complex active flow control was proposed by Xu et al. (2016). Two dielectric barrier discharge vortex generators or simply plasma actuators are placed parallel to the symmetric plane and upstream of the obstacle. The device can induce a cross flow towards or away the symmetric plane. As a result, a pair of common-up-flow or common-down-flow vortices are generated respectively. Such configuration has similar effect compared to pair of vortex generator in Andoh et al. (2009) experiment. The suggested results confirm that a pair of common-up-flow vortices can attenuate the strength of HSV, as both have opposite rotating direction.

1.3   Methods of investigation

The earliest researches in the field of junction flow were all conducted experimentally. It was due to the fact that experiments were the only available option for fluid dynamic analysis. Nevertheless with the progress in technology, more advanced techniques were developed. In the last decade, the investigation method started to combine with numerical analysis. As it can perform analysis of multiple configurations with relatively ease. But the trade off between accuracy and computational cost is still deficient.

1.3.1   Experimental methods

Smoke and oil-flow visualization were the most widely used methods to analyse the fluid flow path around objects during the first years (Schwind, 1962). However, these methods can only deliver qualitative information. Pressure tabs and hot-wire anemometry (HWA) were introduced years later (such as studies performed by Baker (1978a,b, 1980)). The new measurement techniques allowed the measurement of pressure on the junction surface and the flow velocity around the stagnation region. Together with the flow visualization information, a more detailed flow field could be reconstructed. For instance the determination of the flow separating location, vortex size or even the dynamics. Despite the advancement, measurements with these techniques are limited to a single point measurement. Hence, if the characteristics of the entire field is of interest, the measurement should be performed to multiple points in space. Furthermore, the probes have to be placed inside the flow of interest, which can cause deviations from the real measurement, especially in the horseshoe vortex, where complex flow structures are confined in a small region.

An improved instrument for velocity measurement is the laser Doppler anemometry (LDA). Compared to HWA, LDA can offer a non-intrusive point-wise measurement of the velocity yet have a relatively high sample rate. Devenport and Simpson (1990) performed the detailed study of the HSV system with such technique back in 1989. The results are stored in the ERCOFTAC database and are still being used in up to date investigation for numerical analysis validation (Ryu et al., 2016).

Many of the recent studies in junction flow have abandoned the use of pressure tabs or hot wire probes. As alternative, the application of PIV or advanced version of it are growing (Westerweel et al., 2013). The transition is made because the study of the flow topology was challenging using point-wise measurement. Due to the fact the source data (velocity measurement made in different location in space and time) is uncorrelated between each other. Consequently, the observed flow features of junction flow deviate from the real case (Apsilidis et al., 2015).

It should be noted that most investigations performed with PIV technique have limited field of view (FOV), in other words, this technique can only measures velocity and flow topology of a small area. This limitation is related to the limited illuminating power and the low scattering efficiency of small seeding particles. The particles must be kept small to maintain good flow tracing characteristics. Newly developed larger seeding particles have shown to be applicable in large-scale PIV, more details will be given in section 2.1.1. Although the PIV technique is more versatile, most experimental studies of junction flow are still performed to the symmetric plane and the leading edge of the junction model. Only a few researches have shown to investigate other regions of interest. For instance, Hu et al. (2015) studied the stagnation region in multiple planes tilted with an angle in respect to the symmetric plane; Gand et al. (2015) performed multi-planar PIV experiment close to the trailing edge and Koers (2017), stereoscopic PIV (sPIV) to the wake downstream of a wing-flat plate model.

1.3.2   Numerical methods

Due to the complexity of junction flow, numerical simulations do not always yield satisfactory results. Gand had emphasized in multiple numerical investigations that Reynolds Averaged Navier-Stokes(RANS) simulations are unsuitable to predict the features of a junction flow (Gand et al., 2010b, 2012). For instance, the separation region of HSV were overestimated. In addition, corner separations were observed in various RANS simulations, although such features were not observed in experimental results. Regardless the discrepancies, the low order simulations have a decent sensitivity towards changes in the incoming boundary layer or AoA.

A more advanced computational method is by means of (Delayed) Detached Eddy Simulations (DDES). Paik et al. (2007) have shown the dynamics of HSV could be simulated with fair accuracy using the DES approach with an adjusted length scale. The drawback is the predicted time-averaged position and size of the main vortex disagree with reference values. The inacurracy of RANS and DES is suggested to be highly dependant on the employed turbulence model. It was later supported by Gand et al. (2012) with the utilization of Reynolds Stress Model for simulating the turbulence. Yamamoto et al. (2012), and further investigation done by Bordji et al. (2016), applied the Quadratic Constitutive Relation in their simulation, which basically is a nonlinear term added to the eddy viscosity turbulence model. Both turbulence model had shown to improve drastically the properties of corner separation. It is due to the corner flow is a secondary flow of second kind, flow that can be resolved by introducing anisotropic terms in the Reynolds stress tensor. In other words, corner flow is of the second order type, for this reason it cannot be solved by linear turbulence model but with equivalent

order or higher.

Results from Large Eddy Simulation are the closest to experimental values compared to other aforementioned methods. It can capture fairly well the separation position and reverse flow caused by the adverse pressure gradient (Ryu et al., 2016). However the precision also comes with an increase in computational cost. Gand et al. (2012) explained the discrepancies of LES from the experimental value are attributed to the dissipation of the HSV in the wake. Such differences are due to the limit of accuracy of the second order solver scheme.

Despite the differences between numerical and experimental results in junction flow analysis, computational analysis has an unique advantage of calculating the entire fluid domain around the model. Hence the reconstruction and characterization of the flow features can be performed with relatively ease. Although verification is sometime troublesome due to limited experimental data in all junction region.

1.4   Discussion

From the literature review it is clear that the topic of junction flow has been studied extensively. Nevertheless, the understanding of such flow is still not fully assimilated. On the one hand, CFD analysis has improved considerably along the years. However, low-order simulations are still not accurate enough to be fully relied on. For this reason most of the current numerical studies have compared its results with experimental data. Furthermore, a considerable amount of studies are focused in the leading edge region where the HSV originates, and only a small portion treats the downstream region. This preference has lead to lack of data for numerical verification, which also limits the definition of the flow features. On the other hand, experiments that have been done so far are all centred in a single area. For instance the leading or trailing edge, adjacent planes to the protuberance, wake region, etc. There have not been yet measurements of junction flow as a whole to identify the horseshoe vortex topology. Moreover, with the exception of the bimodal behaviour, the dynamics of junction flow along the protuberance are even less investigated. As the few literatures that treat the downstream region only examine the averaged velocity data. Although the fluctuation is the cause of high surface shear, scarce data is available to quantify such unsteadiness.

1.4.1   Research objective and questions

Based on the previous arguments, an experimental investigation is proposed to understand the flow structures around a wing-body junction flow. Additionally, passive control devices are implemented to further extend the scope of the current study. The final aim is to understand the flow structure and how it changes under the influence of control devices. Therefore, the objective of this thesis is defined as follows:

Characterization of flow topology around a wing-flat plate formed junction under the

influence of passive flow control devices by means of large-scale tomographic particle tracking velocimetry.

In order to achieve the project goal, the following main questions and subquestions are formulated.

- How is the flow topology around a wing-body junction?

- How passive flow control devices modify the flow field around a wing-body junction?
  - What are the effects of the control devices on the HSV structure?
  - What quantitative values are representative to compare the performance of different control devices?
  - How effective is each control device on the suppression of HSV and/or turbulence level?

In order to answer the research questions, an experimental campaign is carried out using tomographic Particle Tracking Velocimetry (tomo-PTV) measurement technique. In addition, an auxiliary measurement with stereoscopic particle image velocimetry technique in the wake region of the junction flow is conducted, as it could also return relevant information of the HSV behaviour downstream. The junction flow in study is created by installing a Rood wing model on the wall of a wind tunnel test section in conjunction with different control devices.

1.4.2 Motivation

The newly developed seeder for Large-Scale tomographic PIV/PTV has an airfoil shape and is installed inside the wind tunnel. In the end, it is essentially a junction flow introduced to the tunnel's wall, as it is shown in figure 1.14. Consequently, this effect should be noted as the flow characteristics offered by the wind tunnel are modified. The current work serves this purpose: to characterize the junction flow and possible alternatives to compensate for the unsteadiness paired with the used of the seeder.

1.4.3 Thesis outline

In this report, the theory on the employed experimental techniques is explained in chapter 2. The description of the experimental campaign and the setup follow in chapter 3. The data reduction and processing techniques are

Figure 1.14: Seeder in operation installed inside a wind tunnel. Image from Jux (2017).

described in chapter 4. Methods for flow analysis are also defined in the same section. Finally, the results of the junction flow experiment are displayed in chapter 5 and conclusions in chapter 6.

Chapter 2

Experimental methods

Tomo-PTV measurements along the wing-body junction and sPIV measurements in the junction wake can deliver a new perspective into the understanding of the involved flow structures. In this chapter the working principles of these techniques are further explained, together with information of other tools employed to extend its capability.

In section 2.1, the basis of PIV is discussed. In continuation, variations of image velocimetry are presented from sections 2.2 to 2.4, and a brief historical advancement is presented.

2.1 Particle Image Velocimetry

Particle Image Velocimetry (PIV) is a non-intrusive quantitative flow measurement technique. This technique was first proposed by Keane and Adrian (1992) back in the 80s. The operation of PIV is sketched in figure 2.1 and 2.2. Briefly explained, the fluid domain is seeded with tracer particles, which are carried out by the fluid motion. The particles are then illuminated with a laser beam collimated into a plane. Subsequently, two images are taken within a short amount of time. Later on the images are divided into small interrogation windows and undergo a cross-correlation analysis process, which returns the displacement of the tracers at each window. Since the time separation between snapshots is known, the velocity can be derived by the ratio of displacement and time.

In order to achieve such measurement, proper equipment is required. As mentioned previously, tracer particles or seeding, a powerful illumination and cameras are essential in today's PIV. In the following sections, details on the properties and requirements of the equipment are discussed.
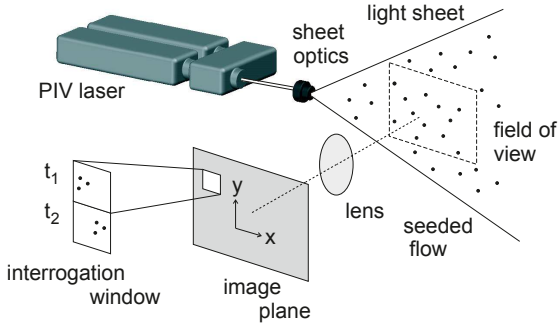
Figure 2.1: Sketch of a PIV set up, image from LaVision GmbH.
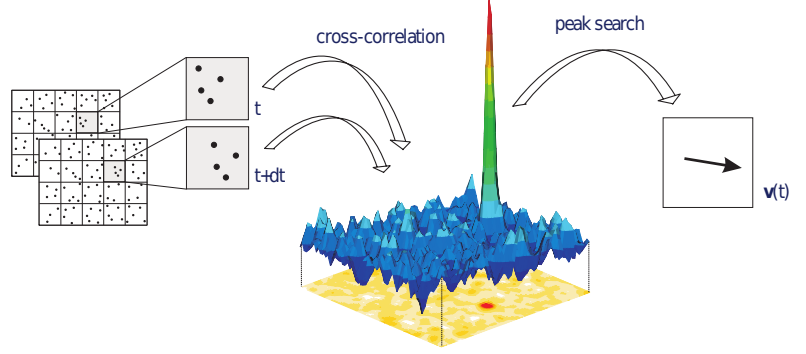
Figure 2.2: Sketch of cross-correlation performed on a particular interrogation window, image from LaVision GmbH.

2.1.1   Tracer particles

Given the fact that most fluids are transparent to naked eye vision, tracer particles or seeding are needed to reveal the fluid motion. Hence, the velocity field determined from PIV is in fact an indirect measurement of the particles velocity rather the fluid velocity. For this reason, tracer particles must present good flow-tracing characteristics in order to minimize the uncertainty in the inferred flow velocity.

When small particles are immersed in a fluid flow, they experience multiple forces from the surroundings. The most relevant for micrometric particle is the Stokes drag, which is proportional to the slip velocity (Raffel et al., 2007). The slip velocity is the relative velocity between particle and fluid, which can be computed from equation 2.1

$$U_s = U_p - U = d^2 \frac{(\rho_p - \rho)}{18\mu} a \tag{2.1}$$

Where U_s is the slip velocity, U_p the particle velocity and U the fluid velocity. On the right hand side, d is the particle diameter, ρ_p and ρ the particle and fluid density respectively, μ the fluid dynamic viscosity and a the acceleration that the fluid experiences.

Additionally, the particle velocity can be expressed as a function of its relaxation time (τ_p) under a step function in velocity change.

$$U_p(t) = \Delta U (1 - \exp^{-\frac{t}{\tau_p}}) \tag{2.2}$$

The relaxation time of the particle is expressed as:

$$\tau_p = d_p^2 \frac{\rho_p - \rho}{18\mu} \tag{2.3}$$

From equation 2.1 and 2.3, it can be deduced that the density for an ideal tracer should be as close as possible to the fluid's density. In practice, if the fluid of study is liquid, this

condition is easily achievable, because tracers used in such studies usually have a similar density as the liquid. However, this is not the case when gas is the medium of study, in which the the seeding is usually three orders of magnitude denser than the fluid. For this reason, microscopic particles are required, as then the slip velocity is compensated and maintained low. For instance, oil droplets used in the stereoscopic measurement performed in this work have a diameter of roughly $1\mu m$.

A quantitative evaluation for the suitability of seeding particles are intimately related to the Stokes number, defined as the ratio of the seeding particle relaxation time and the fluid characteristic time.

$$Stk = \frac{\tau_p}{\tau_f} \tag{2.4}$$

The flow characteristic time is defined according to the flow of interest. In PIV measurements, particles are considered suitable as tracers when their associated Stokes number is below 0.1. Under such condition, the error due to slip condition is typically below 1% (Samimy and Lele, 1991).

Another important characteristic of tracer particles is their ability to scatter light. For particles with a diameter similar or larger than the wavelength of the incident light, the scattered light follows Mie's scattering behaviour. In such condition, the scattered light intensity scales up with the square of the particle's diameter. Additionally, the scatter is highly directional, being the forward direction (downstream from the light source) the strongest in scatter intensity, followed by the backward direction, with the least amount of light being scattered in the perpendicular direction.

The brightest particles are therefore obtained by placing the imaging system downstream of the light source. Nevertheless, such configuration is not always feasible and the system cameras are usually placed perpendicular to the light source for simplicity of the setup.

Helium Filled Soup Bubbles (HFSB) is one type of seeding particles with a diameter of two to three order of magnitude larger, 300 to 1000 μm, than usual oil droplets used in PIV. The larger particles have lighter than air gas, Helium, inside the thin soap shell. Hence their density matches closely that of air, or it is said to have a neutrally buoyant property regardless the larger size. Scarano et al. (2015) have studied the characteristics of HFSB at different Helium-soap flow rate ratio and at optimal condition, the bubbles have a relaxation time in the order of $10\mu s$. Furthermore, Morias et al. (2016) have measured a standard deviation of 50 μs in the particle time response. Because HFSB have higher scattering efficiency, they allow for larger measurement domains and are widely used in today's large-scale PIV/PTV.

Such seeding particles were first used in the 1936 by Redon and Vinsonneau as a means for flow visualisation in wind tunnels. However, most relevant improvements to the seeding generation occurred in the last two decades. Okuno et al. (1993) developed the so called orifice type nozzle for HSFB. It was later improved by Müller and Flögel (2000) and employed in a study of air convection in an aircraft cabin by Bosbach et al. (2009). The nozzle designed by Müller has a production rate of about 50,000 bubbles/s. In Macháček (2002) PhD dissertation, he did

an exhaustive assessment on the bubbles optical properties. The author reported the bubbles present two strong spots of specular reflection on their surface due to the inner refraction and outer reflection of the incident light. However, the two reflection spots are only visible when the bubbles are zoomed in with a high resolution camera. In large-scale PIV measurements, only one single spot would be detected, as the separation between spots is prompt to be smaller than the camera pixel pitch. Moreover, due to the considerably large particle size, the scattering mechanism follows the so called Fraunhofer diffraction (Tu et al., 2017). At this state, particles scattering directionality decreases and the intensity depends on only the particle size.

2.1.2 Illumination

Laser is the preferred light source to illuminate the measurement volume. The advantages of laser over other illumination methods, such as a normal light bulb, are the emission of a monochromatic, coherent and high intensity light. With these properties, the emitted light can be shaped into a defined plane or volume with ease without chromatic aberration[1] and the scattered light from the seeding particles is strong enough to be captured by the imaging system (Raffel et al., 2007).

In PIV investigations, two types of laser are commonly used: Nd:YAG (Neodymium:Yttrium-Aluminium-Garnet) and Nd:YLF(Neodymium:Yttrium-Lithium-Fluoride). The two lasers' fundamental wavelength is $\lambda = 1064nm$ and $\lambda = 1053nm$ respectively, but is turned into visible light by a frequency doubler, $\lambda = 532nm$ and $\lambda = 526nm$ respectively. Nd:YAG laser has typically >200mJ of energy per pulse, with a repetition rate in the order of 10Hz. Nd:YLF laser, on the other hand, has an energy content of about 20mJ per pulse operating at 1kHz, but it can operate up to 10kHz of repetition rate. Given the different laser properties, Nd:YAG laser is used in PIV experiments with a field of study up to $50cm^2$ with a low repetition rate; while Nd:YLF laser is used in time-resolved PIV (TR-PIV) with a reduced FOV up to $20cm^2$ (Scarano, 2013).

For a given FOV, the light intensity is inversely proportional to the thickness of the illuminated region. For this reason, the light intensity in tomographic experiment is generally an order of magnitude smaller than planar PIV. This effect is worsened by the fact the cameras in a tomo-PIV experiment need a small aperture to focus all the particles in the thick volume. Thus, because of limited illumination, the measurement volume usually does not surpass few tens of cm^3 (Scarano, 2013). To overcome the low-light condition in large-scale measurements, light amplification system by reflecting multiple times the incident light inside the measurement volume has been attempted by Schröder et al. (2007) and Ghaemi and Scarano (2010). The amplification system can achieve a gain of 5 times compared to a single pass illumination. However, the system requires also additional mirrors and fine adjustment of the laser beam and mirrors inclination. Today's large-scale tomographic PIV experiments can measure volumes larger than $10,000cm^3$ with the introduction of HFSB as seeding particles (Caridi et al., 2016).

---

[1]Difficulty of a lens to focus due to different diffraction angle of light with multiple wavelength.

2.1.3   Imaging system
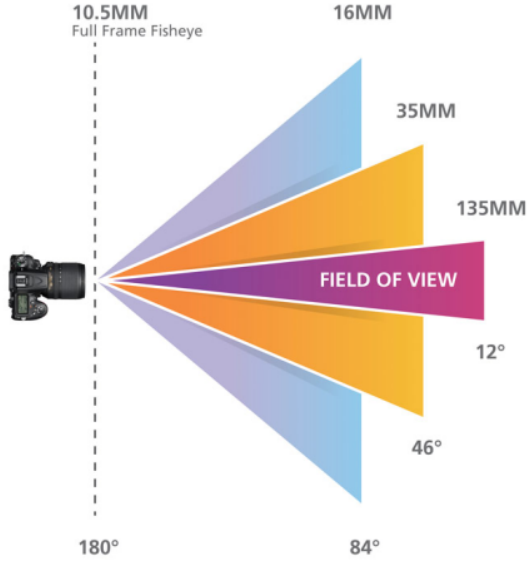
Figure 2.3: Illustration of various focal length and its associated AOV. Image from Nikon.
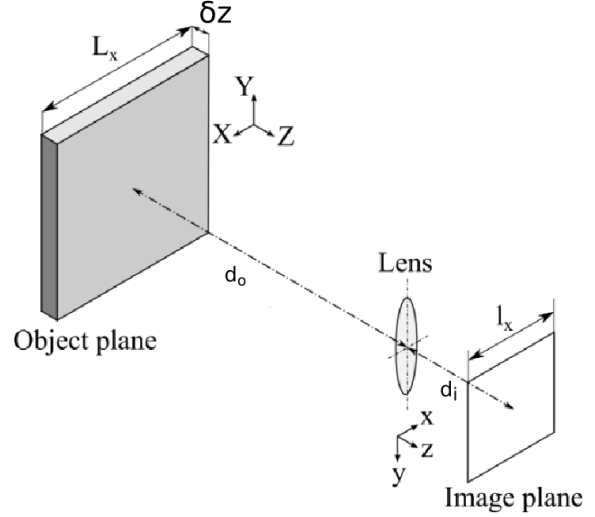
Figure 2.4: PIV optical arrangement. Image adapted from Sciacchitano (2014).

Imaging system in today's PIV experiments consists of CCD or CMOS camera. The camera has to be combined with lens (or objective) in order to focus on objects. The FOV recorded by a cameras is intimately related to the employed lens's focal length (f). For a given distance from a camera to an object, the FOV reduces with increasing focal length. This is due to the angle of view (AOV) becomes narrower as the focal length is increased, as shown in figure 2.3. Since a smaller FOV is projected to the camera sensor, it appears to have a zoomed in effect. A parameter to quantify the zoom effect is the magnification factor (M) (Raffel et al., 2007).

$$M = \frac{sensor\ size}{FOV} = \frac{d_i}{d_o} \tag{2.5}$$

Being d_i and d_o the image and object distance respectively. Through the thin lens equation, the relationship between the focal length, image and object distance can be drawn.

$$\frac{1}{f} = \frac{1}{d_i} + \frac{1}{d_o} \tag{2.6}$$

In addition to the focal length, camera lenses usually have a variable aperture diameter(D) or more commonly quantified with the f-stop number ($f_\# = \frac{f}{D}$). The aperture controls the amount of incoming light that enters to the camera sensor. It also has an influence on the depth of view (δz or DOV) on the object plane.

$$\delta z = 4.88 \cdot \lambda \cdot f_\#^2 \cdot \left(\frac{M+1}{M}\right)^2 \tag{2.7}$$

In tomographic PIV measurement, the laser beam is expanded radially forming a volume instead of a plane. Hence the light intensity is reduced (see section 2.1.2). For the reason the measurement region has a certain thickness, the cameras need to have a thicker DOV than in planar PIV configuration. Hence the need of the smaller aperture mentioned in the previous section. When HFSB are used as seeding particles, the volume size limitation is less restrictive and thereby it is possible to carry out the large-scale PIV measurement.

2.2 Stereoscopic PIV

In planar PIV measurement, the measured velocity field is composed only by projections of velocity vectors on the laser sheet or measurement plane. However, in the case the flow is highly three dimensional, an out-of plane component of velocity is present and needs to be accounted for. Otherwise the measured in-plane velocity is affected by errors due to perspective transformation (Willert, 1997).

In order to resolve the out-of-plane component of velocity, the most straightforward method is by implementing an additional camera into the imaging system. This technique is then named stereoscopic PIV (sPIV), also it is stated to be a two-dimensional three-component (2D-3C) measurement. The two cameras are placed at different positions but record the same measurement plane. The out-of-plane velocity is then reconstructed from the differences between the projected velocities on the two cameras. Nevertheless, to make this process possible, a calibration procedure is required as the camera images have a strong perspective distortion due to the viewing angle.
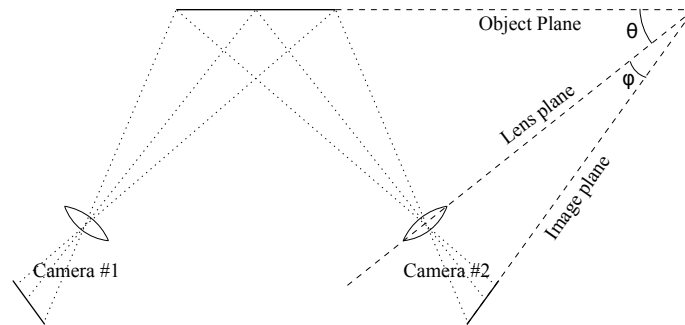
Figure 2.5: Sketch of stereoscopic imaging systen in *Scheimpflug* condition, image from Willert (1997).

Note the imaging system in figure 2.5 is in the so called *Scheimplug* condition. In this configuration, the cameras are positioned at a high deflection angle, summing up the fact of having a low DOV, the images would appear to be defocused on the sides. This is due to the plane of focus is parallel to the camera sensor in normal condition. For this reason, *Scheimplug* adaptors are mounted in between cameras and lenses such that the adaptors can rotate the plane of focus to match the laser sheet.

The calibration process in sPIV consists of two part, first the geometrical calibration and

Figure 2.6: Picture of a Scheimflug adaptor with lens attached.

second, the self-calibration. The geometrical calibration accounts for the perspective distortion on the image. In the geometrical calibration an image of a calibration plate is taken. Given the fact that the dimensions of the plate are known, each point of the image can be mapped back to true dimension. Additionally, the position and viewing angle of the cameras are estimated. The self-calibration process accounts for misalignment between the calibration plate and the laser sheet, in which a disparity map is resulted (Gray and Wieneke, 2007). This map is later applied to correct the mapping function generated during the geometrical calibration to yield a more accurate calibration.

Figure 2.7: Calibration plate used in the current sPIV study.

For the calculation of the out-of-plane component of velocity, first a two-component velocity field is computed for each camera. It is computed as in planar PIV by a cross-correlation method. Then the calculation of the out-of-plane component follows by means of simple

trigonometry. Finally, the true in-plane velocities are also calculated by a similar approach.

$$U = \frac{U_1 \, tan \, \alpha_2 + U_2 \, tan \, \alpha_1}{tan \, \alpha_1 + tan \, \alpha_2} \tag{2.8}$$

$$V = \frac{V_1 \, tan \, \beta2 + U_2 \, tan \, \beta_1}{tan \, \beta_1 + tan \, \beta_2} \tag{2.9}$$

$$W = \frac{U_1 - U_2}{tan \, \alpha_1 + tan \, \alpha_2} = \frac{V1 - V2}{tan \, \beta_1 + tan \, \beta_2} \tag{2.10}$$

U, V, W are the three components of velocity, while the subindices indicate the calculated component from each camera; α is the angle between the measurement plane normal and the camera line of sight in the horizontal plane or yaw angle of the cameras(XZ plane of figure 2.8), and β is the equivalent angle for the vertical plane(XY plane of figure 2.8), or pitch angle.
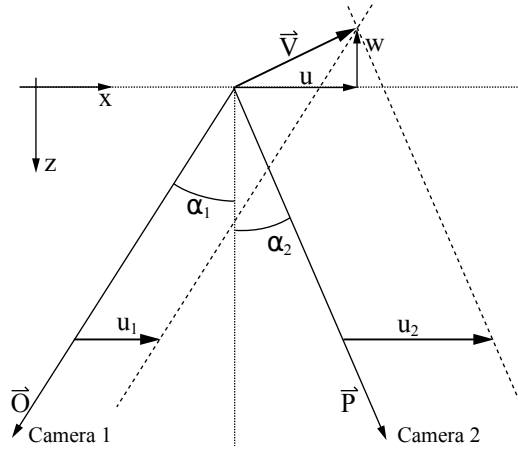
Figure 2.8: Sketch of a vector viewed by a stereoscopic system, image from Raffel et al. (2007).

2.3 Tomographic PIV

Despite the sPIV technique is able to measure the normal component of velocity, the fact that the measurement is performed in a plane has limited the full understanding of complex flow. For instance, the topology of turbulent flow structure is highly three-dimensional, which cannot be fully defined with a 2D measurement such as sPIV (Scarano, 2013).

Motivated by a process which can describe thorougly 3D structures in flows, tomographic PIV (tomo-PIV) was developed by Elsinga et al. (2006). In this technique, the particles in the measurement volume are reconstructed digitally from different views obtained from the cameras. Nevertheless, an exhaustive and almost error-free calibration process is needed to achieve an accurate reconstruction. The velocity field is computed as in planar PIV through cross-correlation of discretized interrogation volume.

The complexity in tomo-PIV is mostly centred in the calibration and reconstruction process. First of all, according to Elsinga et al. (2006), the reconstruction quality of the particles is considered acceptable if the geometrical calibration error is below 0.4 pixels, which is rarely achieved in real experiments. For this reason, the volume self-calibration method was developed for tomo-PIV applications (Wieneke, 2008). After applying this process to the geometrical calibration, the mapping function error can be reduced to below 0.2 pixels.
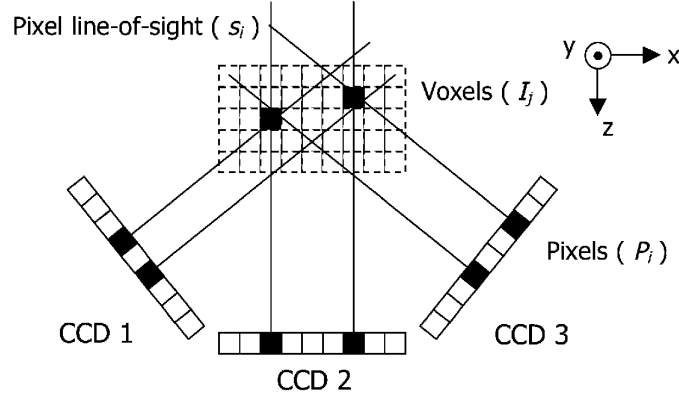
Figure 2.9: Sketch of intersecting line of sight. Image from Atkinson and Soria (2009).

In regards to the reconstruction process, it requires higher computational cost than sPIV. The digitalized measurement volume is composed by a finite number of voxels, each of them has a unique value of intensity reconstructed from the intersection of line of sight (LOS) from the different cameras views. In the first paper on tomo-PIV by Elsinga et al. (2006), the reconstruction method used during the development of tomo-PIV was based on algebraic reconstruction technique (ART) and also its variant Multiplicative-ART (MART). Both techniques express the cameras pixels intensity as a function of the voxel intensity; in such a way, a series of linear equations is formed :

$$P_i = \sum_j W_{ij} I_j \tag{2.11}$$

P_i is the recorded intensity on the ith pixel of the camera, I_j the intensity of the jth voxel, W_{ij} is the weighting matrix which associate the ith pixel intensity of the camera to jth voxel. The (M)ART algorithm is computationally costly because the weighting matrix has large number of elements. Based on equation 2.11, the weighting matrix has $m \times n$ dimensions, being m the number of pixels and n the number of voxels. In a general case, a single camera has roughly 1Mpx of resolution, and a reconstructed volume with 200 millions of voxel, which give place to a matrix with $O(10^{14})$ elements per camera (Atkinson and Soria, 2009).

Other reconstruction techniques were proposed to tackle the memory demanding issue. For instance, Atkinson and Soria (2009) presented the multiplicative line-of-sight (MLOS) algorithm, which considers only voxels with non-zero intensity. This algorithm can reduce drastically the required memory (up to 15 times less) and also in computing time (5.5 times less) as fewer equations are present. However, the number of reconstructed ghost particles[2] is also higher than (M)ART technique.

---

[2]Reconstructed particle which does not exist in the real measurement, but is reconstructed due to ambiguity in camera views.

2.4 Tomographic PTV

Tomographic Particle Tracking Velocimetry (tomo-PTV or 3D-PTV) technique determines the location and intensity of each individual particles that are in the measurement volume. Unlike (M)ART algorithm, particle tracking does not need the reconstruction of the volume, subsequently, neither the weighing matrices. Such characteristic makes tomo-PTV to be memory more efficient than tomo-PIV. Once the particles are identified, they are tracked down across multiple time instances, and the corresponding pathlines (also called tracks) are determined. Tomo-PTV is able to determine accurately the velocity and acceleration of particles, while in tomo-PIV, the velocity field suffers from spacial averaging as it is determined by means of cross-correlation of small interrogation windows. Nevertheless, the PTV technique is only possible for seeding density an order of magnitude lower than PIV (around 0.005ppp), otherwise the occurrence of ghost particles become dominant (Schanz et al., 2016). Recently, PTV in highly seeded flow becomes possible with the introduction of iterative particle reconstruction (IPR) technique (Wieneke, 2013) and Shake-The-Box (STB (Schanz et al., 2016)).

In 3D-PTV, particles are identified through triangulation of the 2D cameras images. This approach only works well on flows with low seeding density as no correction method is included. IPR takes a step further from this point. From the identified particles, the algorithm computes the projections to the different camera views by means of optical transfer function (OTF) (Schanz et al., 2013a). Briefly explained, an OTF is a function which defines the back projected particle shape for a given particle position. The back projected image is compared with the original recorded image and results in a residual image. Three operations are performed to the residual image: the bias in position and intensity between true and triangulated particles is estimated and used to correct the triangulated particles; unidentified particles in the previous triangulation are added; elimination of particles if their corrected intensity falls below a threshold or particles that are within one voxel distance from another. These processes are then used to update the list of identified particles and the reconstruction process is iterated until the cost function (difference in intensity between true and projected particles) is minimum. With this particle identification method, the approach can deal with seeding dentity to up to 0.05ppp Wieneke (2013) with similar performance as MART algorithm.

Another advancement in tomo-PTV is the Shake-The-Box tracking algorithm Schanz et al. (2013b, 2016). This method includes both the IPR technique and previously calculated velocity and acceleration field to assist further velocity field calculation. The STB scheme starts with the initialization of tracks, which basically is the velocity of the identified particles during the first few time steps, e.g. five to ten. This initialization is needed because it assembles the tracks predictor for the algorithm. Schanz et al. (2013b, 2014) have shown the track initialization can be attained by using IPR with high number of iteration to ensure the highest identification quality. While the tracking algorithm detects and connects individual particles to build up trajectories. Another initialization approach is similar to classical tomo-PIV method, where the tracking method is applied to particles reconstructed in the voxel space. Once the initialization is done, particles trajectories are fitted with polynomials and the particles position of the next time-step is extrapolated. The particles position is then back projected to the camera views followed by the same processes as in IPR to correct
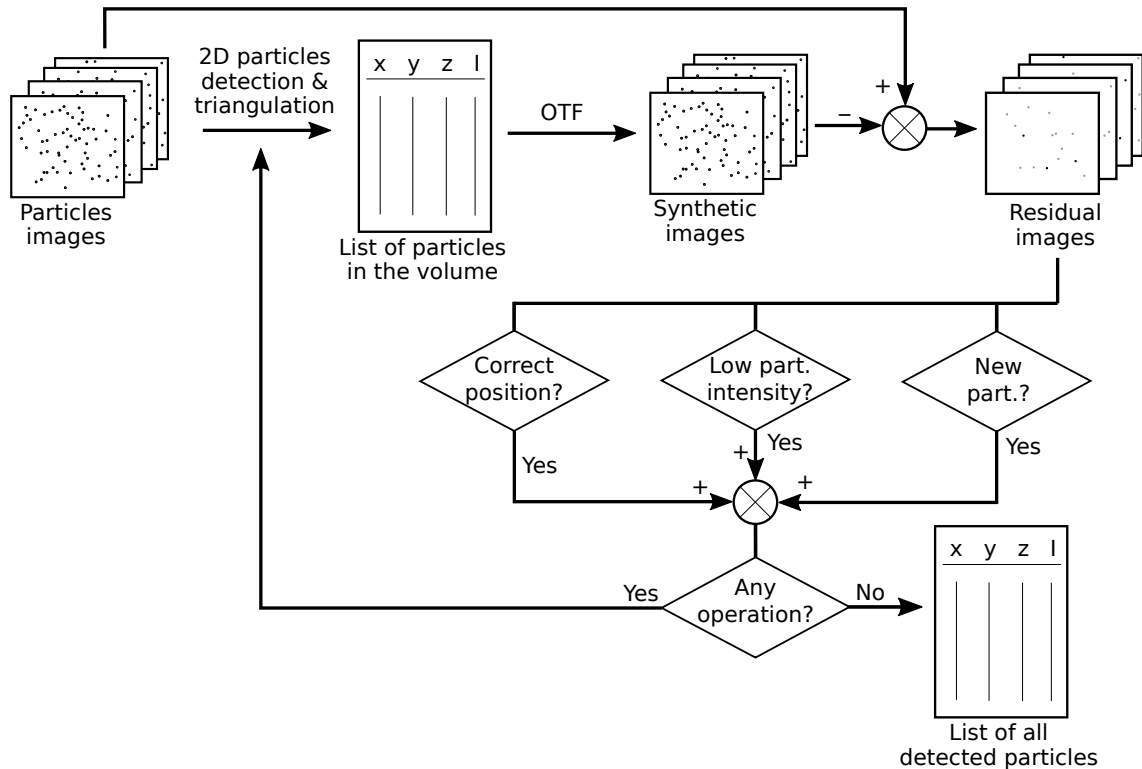
Figure 2.10: Flow chart of IPR.

the particles position (the correction process is called "shaking" by the authors). After the correction is completed, new polynomials are fitted to update the tracks, new positions are extrapolated for the next time step and the STB iterations start over again. It should be noted that during the correction phase, new particles could enter into the measurement volume for the first time. In such case, these particles are then excluded from the built trajectories until further time-steps when a robust predictor is made available for them. On the contrary, a track is concluded and no longer updated when the associated particle exits the measurement volume.

The STB algorithm is considered one of today's most efficient processing methods for tomographic measurements. First of all, it is 5-8 times faster in processing speed than tomo-PIV processing (Schanz et al., 2016), while still have the same or even higher accuracy in velocity estimation. A sample result is shown in figure 2.12, where particles trajectories computed with STB are displayed. Although the velocity information is attached to each particle's track, in other words, represented in Lagrangian frame of reference, the velocity field can be transformed into gridded format as in tomo-PIV (Eulerian frame of reference) with relative ease. However, precision is lost to some extent due to spatial averaging. Finally, data obtained from a tomo-PIV set-up can be potentially processed with STB as long as time resolved data is acquired.
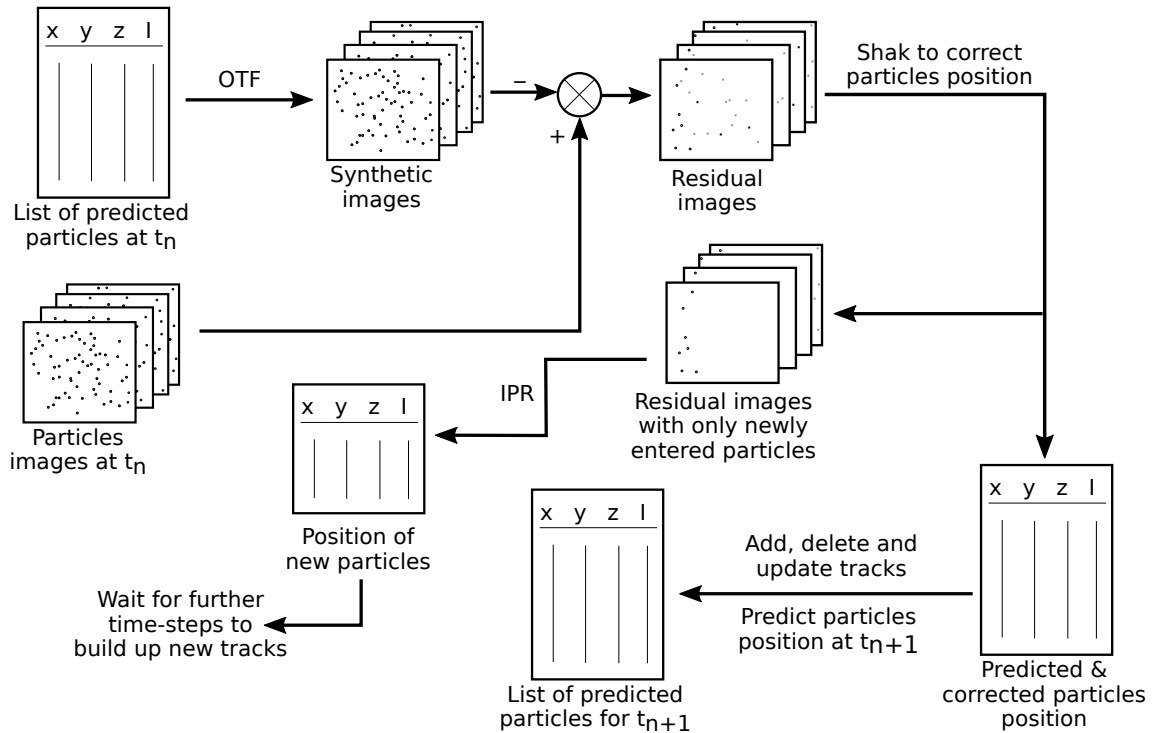
Figure 2.11: Flow chart of STB for a given time-step.
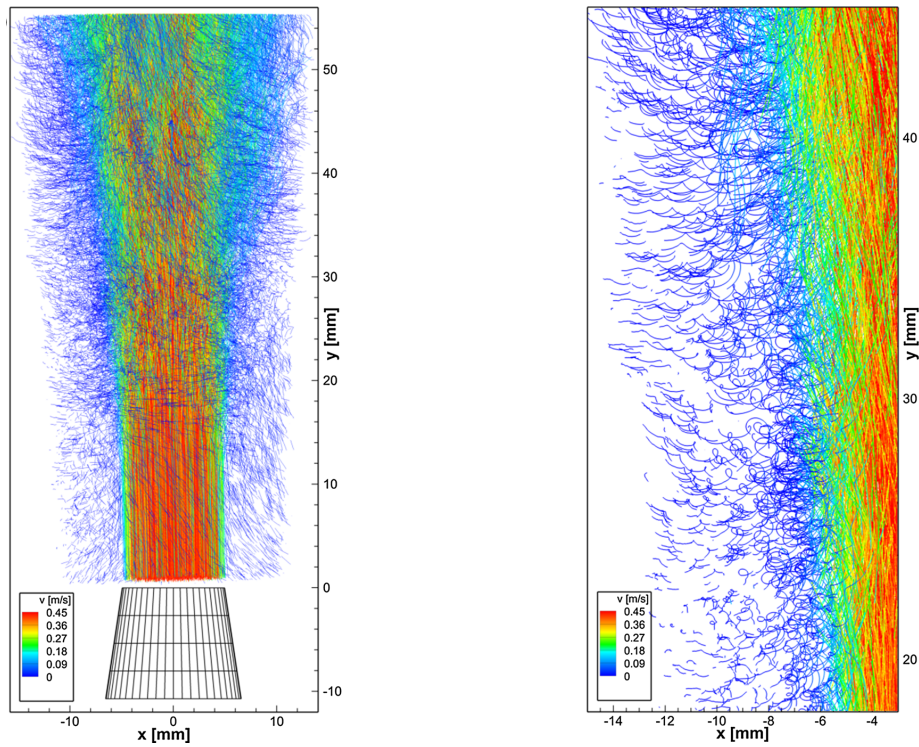
(a) Particle tracks of a water jet experiment.

(b) Close-up view of 2.12a.

Figure 2.12: Water jet experiment processed with STB. Image from Schanz et al. (2016)

Chapter 3

Experimental Setup

The experimental campaign is carried out in the Low-Speed Laboratory of Delft University of Technology. All measurements are performed at freestream velocity $U_\infty = 10 \ m/s$. This chapter describes the details of the wind tunnel facility where the experiments are conducted (section 3.1), the specifications of the wing-flat plate model and the control devices (sections 3.2 and 3.3). The chapter concludes with the definition of the experimental conditions for both sPIV and large-scale tomo-PTV measurements.

3.1   Facility

The junction flow experiment is performed in the M-tunnel at the Low Speed Laboratory (LSL) of TU Delft. The tunnel can be operated as an open jet or as a closed loop tunnel. Depending on the operation mode, the tunnel can deliver wind speeds up to 35 m/s or 50 m/s respectively. The test section is square shaped with a cross section of 40 x 40 cm^2. The test section is about 2 m long, allowing the boundary layer to grow up to a few centimetres before exiting. Besides, the tunnel can be extended with an attachable test section. In the current work, an extended plexiglass test section with 60 cm in length is installed. The ceiling upstream of the extension is tripped with zig-zag tape to achieve a turbulent boundary layer. Before the contraction, the tunnel cross section is about 89 x 98 cm^2. Hence, the contraction ratio of the M-tunnel is about **5.45**. The turbulence intensity is measured in the order of 0.9% operating at 10 m/s.

Figure 3.1: Picture of the M-tunnel. Fog generator and wing tunnel inlet on the left and test section on the right.

3.2   Wing-body Junction

The wing model used in the experiment is based on Rood wing model. This model is a modified NACA0020 with a semi-elliptic nose with major to minor axis ratio of 3:2. The Rood wing was designed by Rood (1984) and later modified by Hasan et al. (1986). Rood designed this wing model specifically for junction flow studies, as he stated "*The blunter nose produces a larger vortex, which leads to spatially more extensive, hence more easily measured flow structure*" (Rood, 1984). For this reason, the same model was used in numerous posterior juntion flow studies, e.g. Devenport et al. (1990); Fleming et al. (1991); Apsley and Leschziner (2002); Ryu et al. (2016) and more.

The wing-body junction is created by installing a Rood wing model on the walls of the detachable plexiglass test section. The wing model has a chord (c) of 200 mm, maximum thickness (T) of 47.5 mm, and span (h) of 400 mm, which is the same as the test section breath. The model's leading edge is located 160 mm downstream from the beginning of the extended test section. Zigzag tape is placed at the maximum thickness of the wing model to force transition on the model. In addition, the transparent test section allows an easy optical access.

The Rood wing model has a bluntness factor value of 0.32, the Reynolds number based on the model's chord is $Re_c = 1.34 \times 10^5$ or $Re_T = 3.18 \times 10^4$ if the model thickness is taken as reference. The momentum deficit factor of the present study is 6.67×10^7, which is about an order of magnitude lower compared to some previous literatures, e.g. Devenport et al. (1990); Gand et al. (2010a); Apsilidis et al. (2015), etc. Although the MDF is lower, a turbulent junction flow is achieved given the fact that the Re_θ is sufficiently high (>1500, (Gand et al., 2010a)), see section 5.1 for details on the boundary layer properties. The reduced value of MDF means a less turbulent HSV structure is present during the experiment.
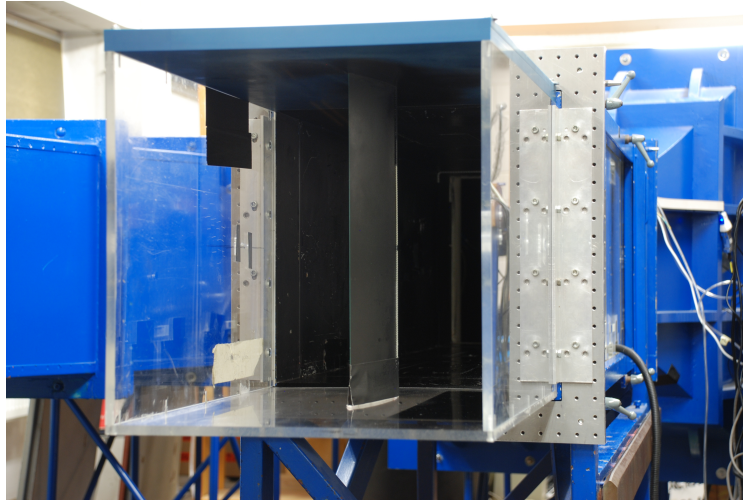
Figure 3.2: Transparent test section with rood wing installed.

3.3 Control Devices

The passive control devices included in the study are leading edge fairing, vortex generators and the antifairing. These devices are selected among the ones discussed in the literature review (see section 1.2.1).

3.3.1 Leading Edge Fairing

The leading edge fairing design used in the experiment follows the works from Van Oudheusden et al. (2004). This design method has proven to be effective in eliminating leading edge separation and promotes relaminarisation of the flow over the wing. In addition, the fairing design is parametric, which means that its geometry can be easily obtained given the shape of a certain airfoil.
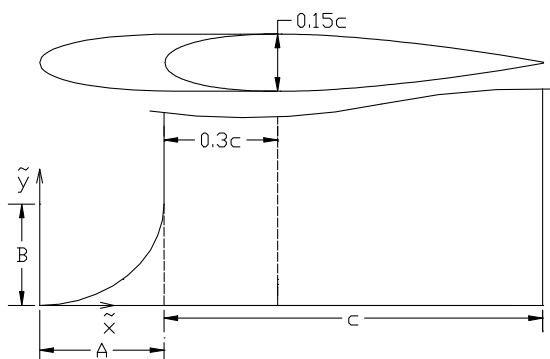
(a) Sketch of the simplified fairing design by Van Oudheusden et al. (2004).
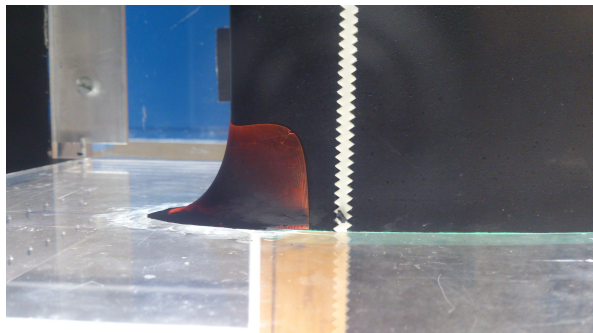
(b) Picture of the fairing installed on the junction model.

Figure 3.3: Fairing design.

The parametric design of the fairing is shown in figure 3.3a. The fairing nose is a stretched curve of the airfoil leading edge, while the fairing spine (the curve tangent to the floor and the airfoil leading edge) is defined by an ellipse with semi axis A and B, figure 3.3a. The fairing used in this work has the value of A=0.14c and B=0.2c. The fairing is designed to be attachable to the junction region. In this way the fairing can be mounted effortlessly and no major modification needs to be done to the wing-plate junction model. The requirement for a fairing insertion design is that it should not add too much thickness to the original model close to the fairing-wing union region. To make the fairing model possible, it is 3D printed with photo-sensitive resin. 3D printing technique is chosen because it can produce walls with a minimum thickness of about 50 μm, which is hardly achievable by machining methods.

3.3.2 Vortex Generators

Vortex generators in common-up-flow configuration create vortices with opposite rotating direction compared to the leading edge HSV. Therefore, the strength of the HSV is mitigated when both vortices are combined.

In the present work, vortex generators both in spacing and series configuration are tested and measured with sPIV at the wake region (see section 3.4.1). The results are processed on the spot and some configurations are discarded for the tomographic measurement due to time constraint.
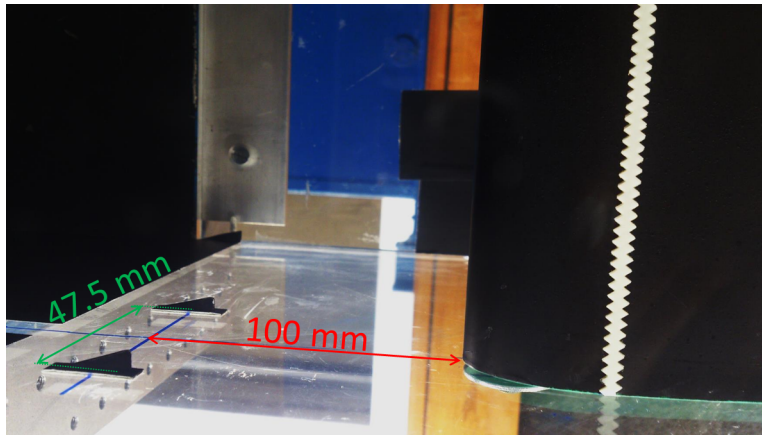
Figure 3.4: Placement of the vortex generators in spacing configuration. The VG are separated 47.5 mm apart.

The triangular-shaped vortex generators are 21 mm long, 6 mm height and 1 mm thick. The deflection angle of the device is 18 degrees with respect to the freestream direction. In the series configuration, two pairs of VG are positioned at $100mm$ (0.5c) and 150 mm (0.75c) upstream of the leading edge. For the spacing configuration, one pair of VG is used and it is placed about 71.25 mm apart (1.5 times the wing model thickness T) and 100 mm upstream from the wing model leading edge (50% of the chord length or 0.5c). However, it is found from the results that this separation distance is not the optimum, hence later on it is changed

to 47.5 mm (1T). The setup of this configuration is shown in figure 3.4.

3.3.3 Antifairing

The antifairing device is included in this study because it has been showed by Belligoli (2015) and Koers (2017) that it outperforms other conventional fairing designs in terms of drag reduction. However, the flow structure and the working mechanism of such device is still unclear.

Since the antifairing has a dented shape on a flat surface, a new plate has to be manufactured and it must have the same dimensions as the test section wall. The manufactured plate is shown in figure 3.5 and a sketch of the antifairing design in 3.6.

Figure 3.5: Photograph of the antifairing with Rood wing installed.
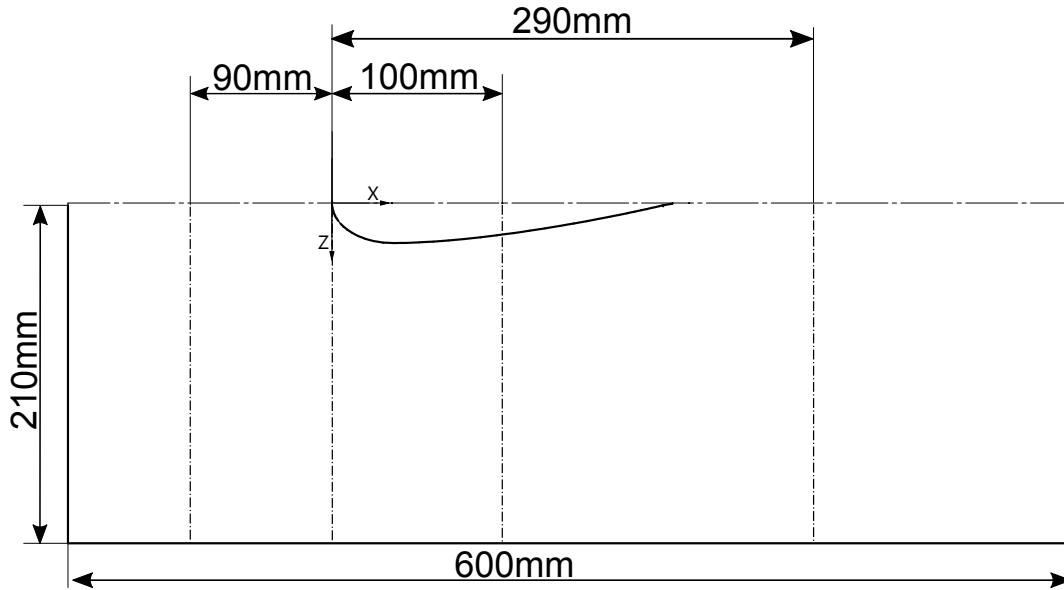
(a) Top view of the antifairing drawing. The locations where the plate contour is extracted are indicated with dashed-dot line.
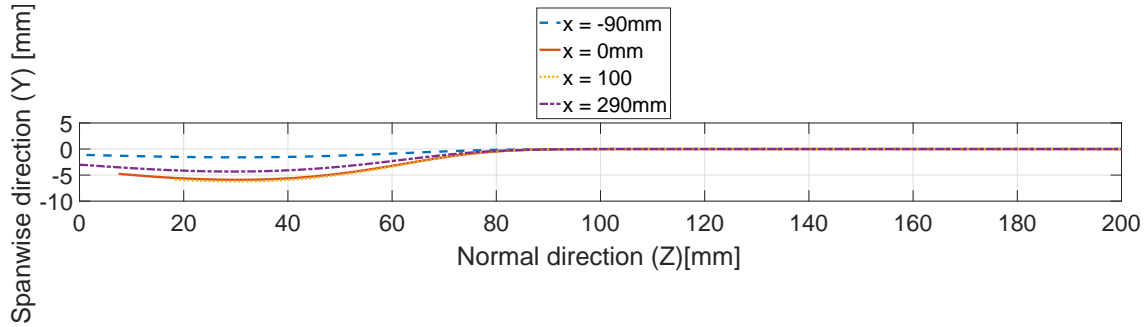
(b) Contour of the plate at different location.

Figure 3.6: Drawing of the antifairing plate.

3.4 Data Acquisition and Design of Experiment

The flow around the junction is measured using two measurement techniques: sPIV and large-scale tomo-PTV. These techniques are based on imaging velocimetry, and thus both share the same illuminating and imaging system. The specifications of the equipment are briefly described in the following paragraphs and the settings are explained separately in each technique setup.

The **imaging system** consists of high-speed cameras FASTCAM SA1 from Photron, distributed by LaVision. The sensor of the cameras has 1024 x 1024 pixels (1Mpx) of resolution and pixel pitch of 20 μm. The cameras have a digital resolution of 12 bits and can record up to 5,400fps at full resolution.

The **illumination** is provided by a Quantronix Nd:YLF high-speed laser, model Darwin Duo.

The energy of each pulse is about 20 mJ operating at 1 kHz.

3.4.1 Stereoscopic-PIV

(a) Isometric view of the sPIV setup.

(b) Detailed view on the sPIV setup. The FOV is marked with yellow dotted line and the camera separation angle is denoted by θ.
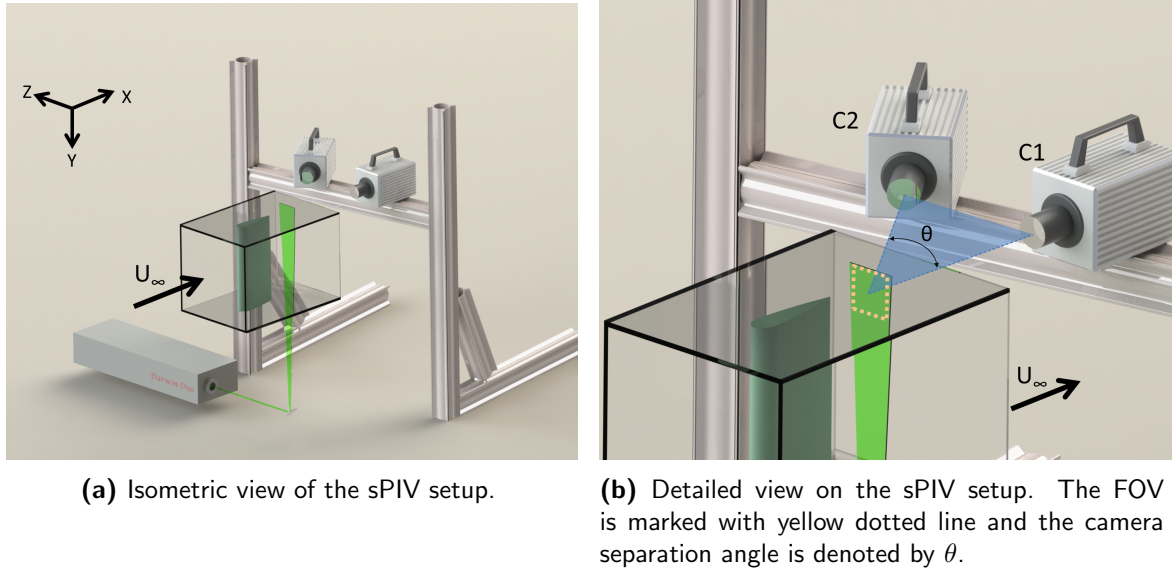
Figure 3.7: Reproduction of the sPIV setup.

Two high-speed cameras are used for the sPIV measurement setup. The first camera is placed downstream and the optical axis is parallel to the flow direction and the other at about 35 degrees. The measurement plane is illuminated through the side of the test section opposite to the side of the measurement domain because the Antifairing plate is opaque. For this reason, the top junction is studied as then the optical setup for the laser is easier (see figure 3.7). The laser sheet is placed orthogonal to the flow direction at 150 mm downstream from the trailing edge and has a thickness of 3 mm.

The cameras are installed with f=105mm objectives and are placed approximately 45 cm downstream of the measurement plane. Given such configuration, a FOV of 93 x 93 mm^2 is achieved and the setup has a magnification factor of 0.22, or a resolution of 10.85 $pixel/mm$. The f-stop is set to 8 in order to focus all the particles illuminated by the laser sheet.

Fog particles are used as tracer and they are injected into the inlet of the wind tunnel.

The stereo-images are acquired in double-frame mode with a time separation (δt) of 90 μs. This time separation allows a particle with freestream velocity to travel approximately one third of the laser sheet thickness. The sampling frequency of pairs of double-frame images is set to 500 Hz.

A summary of the sPIV setup and test matrix is displayed in table 3.1.

Table 3.1: sPIV setup parameters

Imaging

Sensor size	$20.48 \times 20.48 \ mm^2$	Field of View	$93 \times 93 \ mm^2$
Resolution	1024×1024 pixels	Magnification factor	0.22
Objective	$105 \ mm$	Camera distance (C1|C2)	$426 \ mm$ | $495 \ mm$
$f\#$	8	Camera angle (θ) (C1|C2)	0 deg | 35 deg

Acquisition

Mode	Double Frame	Freestream Particles displacement	$1 \ mm$
Seeding	Fog		

Test Matrix

Wind speed	Configuration	f_{sample}	δt	Number of images
$10 \ m/s$	Clean Fairing VG (Series) VG (Spacing 1.5T) VG (Spacing 1T) Antifairing	$500 \ Hz$	$90 \ \mu s$	1000

3.4.2 Tomographic PTV measurement and design of experiment

Three cameras are used for the tomo-PTV measurement. All three are positioned approximately 80 cm away from the wing model in the normal direction. The cameras are equipped with 60 mm objectives and the f-stop number set to 16. The measurement domain of the experiment is about $220 \times 90 \times 70 \ mm^3$. Since the height of the FOV is roughly half of the length, the cameras are set to operate in cropped frame mode of 1024 x 512 pixels. In cropped frame mode, each camera can record more images than in full frame mode before the memory runs out. The magnification factor of the tomo-PTV setup is 0.098, and a digital image resolution of 4.98 $pixels/mm$.

The laser beam is expanded radially from the bottom of the test section toward the upper junction. A knife edge filter is used to limit the depth of the measurement volume.

HFSB is used as seeding particles in this experiment. In order to seed the measurement domain, the seeding rake (see figure 3.8) is installed in the tunnel, upstream of the contraction, see figure 3.9. Each nozzle of the seeding sys-

Figure 3.8: HFSB seeding wing rake.

tem has a production rate of 25,000 *bubbles/s* and can seed a cross section area of $5 \times 5\ cm^2$ (Caridi et al., 2015). The freestream velocity before the contraction is about 1.83 *m/s*. Given these characteristics, a theoretical seeding concentration of 5.5 *bubbles/cm³* is achieved. The seeding rake is composed by four seeding wing of 50cm each and separated 5cm in between. A seeding wing has 20 nozzles installed on it with a nozzle pitch of 2.5cm. The strut which connects the rake to the wind tunnel wall is roughly 40cm long.
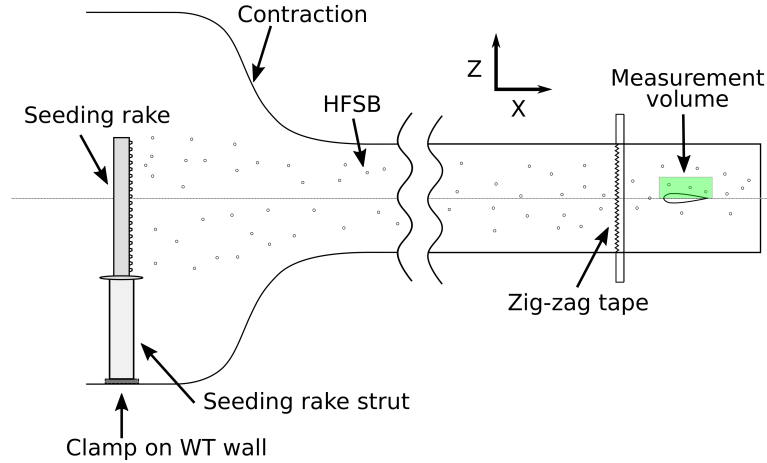
Figure 3.9: Sketch of the seeding rake installation.

A particle displacement of 10 pixels is allowed in between snapshots. This displacement can be attained with an acquisition frequency of 5 *kHz* for the given wind speed. Particle images are acquired in two different modes. The first is time-resolved, which takes images continuously and allows the time evolution study of the HSV structure. However, the analysis of this data is out of this project scope. The second mode is the so called cyclic or burst mode, which consists on the acquisition of multiple uncorrelated sets (each set contains 30 images recorded continuously). Given the fact that statistical convergence can be reached with less uncorrelated samples, images captured in burst mode are used to calculate the averaged velocity field.

For the given concentration, assuming a bin size of $0.5 \times 0.5 \times 0.5 cm^3$, and the statistical convergence is achieved with 500 *bubbles/bin*, about 800 burst cycles are needed. However, more cycles are recorded as in practice the particles density is usually lower than the theoretical value.

The tomo-PTV experimental setup is summarized in table 3.2

Table 3.2: Tomo-PTV setup parameters and test matrix.

Imaging

Sensor size	$20.48 \times 20.48\ mm^2$	Magnification factor	0.098
Resolution	1024×1024 pixels	Camera distance (C1|C2|C3)	$742\ mm \mid 795\ mm \mid 773\ mm$
Objective	60mm	Camera angle $(\theta_x\|\theta_y)$	
$f\#$	16	C1	-4 deg |0 deg
Field of View	$220 \times 90 \times 70\ mm^3$	C2	-6 deg |-21 deg
		C3	-16 deg | 9 deg

Acquisition

Particle displacement	10 pixels ($2.2mm$)	Seeding	HFSB
f_{acq}	$5kHz$		
Mode	Burst	Mode	Time-Resolved
f_{sample}	$25\ Hz$	f_{sample}	-

Test Matrix

Wind speed	Configuration	Acquisition mode	Number of sets	Total number of frames
10 m/s	Clean	Burst	1800	54000
		Time-resolved	1	10000
	Fairing	Burst	1800	54000
		Time-resolved	1	10000
	VG (Spacing 1T)	Burst	1800	54000
		Time-resolved	1	10000
	Antifairing	Burst	1800	54000
		Time-resolved	1	10000
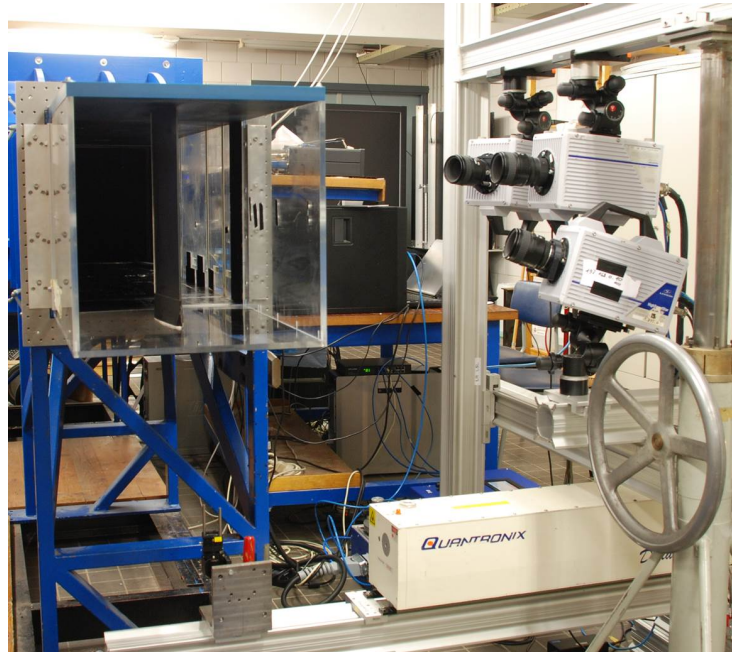
(a) Photograph of the tomo-PTV setup.
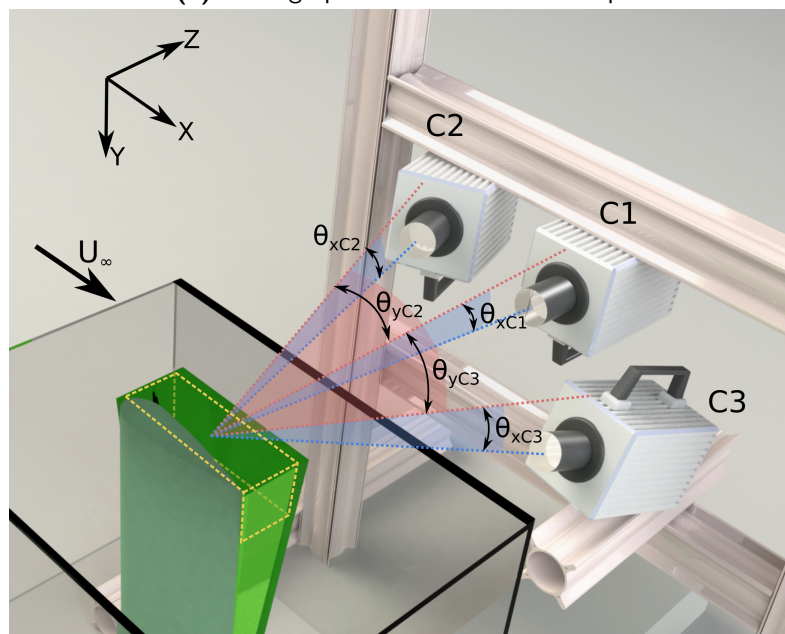
(b) Schematic of the tomo-PTV setup.

Figure 3.10: Picture and isometric diagram of the imaging system.

Chapter 4

Data Analysis and Reduction Techniques

The aim of this project is to reveal the flow topology in the junction flow configuration. In order to reveal and extract it, the data obtained from the experiments has to be processed beforehand.

This chapter starts with a discussion on the procedure to obtain velocity fields from the recorded images. This includes image pre-processing techniques (section 4.1), description on the processing parameters (section 4.2), both for sPIV and tomo-PTV, and post-processing methods of the data (section 4.3). The chapter closes with a survey on flow analysis methods such as vortex identification and strength determination (section 4.7).

4.1 Image Pre-Processing

The raw recorded images usually contain background noise and undesired reflections. Although the latter can be reduced by covering the affected parts with non-reflective paint or foil, the problem could still persist.

To increase the image quality, image pre-processing techniques are implemented. In the current work, image correction by subtraction of the averaged light intensity is employed. As the name indicates, this method computes the average light intensity of a recording in each pixel, which is then subtracted from each individual image. The outcome of this filter is sharper particle images with less noise contamination. This filter is relatively robust if the reflection is constant across the entire recording. Nevertheless, this practice is not suitable for images with low particle intensity, as the subtraction would reduce the particles brightness below a recognisable level.

In the low scattered light case, the subtraction of the minimum recorded light intensity can be used. Although reflections are not removed completely by using this method, this technique

can still yield an improvement on the results while preserving most of the particles.

A sample of light intensity subtracted image is shown in figure 4.1. The unfiltered image shows a strong reflection on the leading edge fairing, which is partially removed in the minimum subtraction filter and almost eliminated in the average subtracted one.

(a) Unfiltered.   **(b)** Min. subtracted.   **(c)** Avg. subtracted.
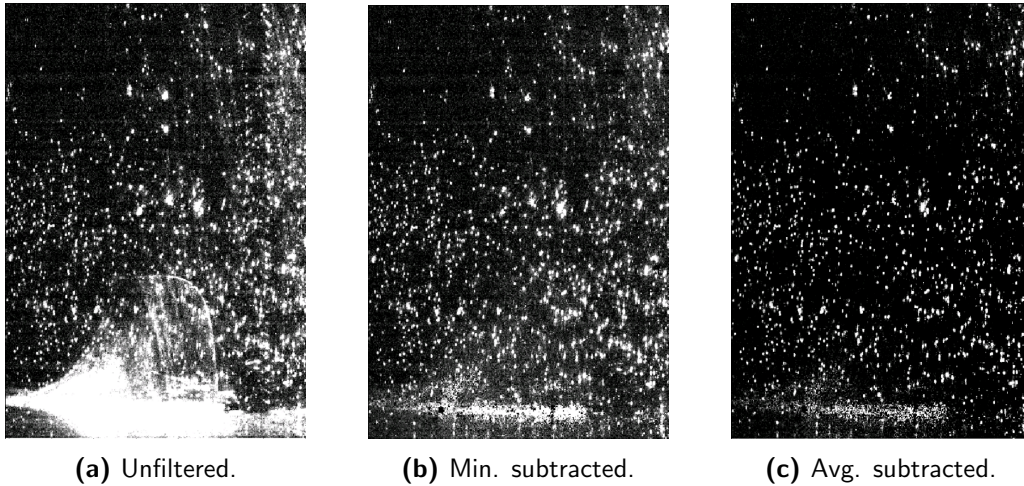
Figure 4.1: Sample of filtered and unfiltered images

4.2   Data Processing Parameters

Two types of processing parameters are discussed in the following sections: one corresponds to the setting of the sPIV experiment and the other the tomo-PTV.

4.2.1   sPIV Processing

Table 4.1: Processing parameters of sPIV measurement.

Processing	
Method	Stereo Cross-correlation
Windos size	32 x 32 pixels
Overlap	75%
Window Shape	Square

The processing parameters of sPIV resemble to the one from planar PIV, as both techniques rely on cross-correlation method to obtain the velocity field.

The processing software *Davis 8.3.* from LaVision is used for the processing of the stereo images. The field is obtained through stereo cross-correlation method. The interrogation windows size is 32×32 pixels with 75% of overlap. Only velocities within two standard deviations are included to calculate the average field. The processing parameters are summarized in table 4.1. With this configuration, the velocity vectors are spaced 8 pixels from the neighbours. Stated otherwise, a vector pitch of $0.73\ mm$ is achieved.

4.2.2 Tomo-PTV Processing

The *Shake-The-Box* algorithm (Schanz et al., 2016) in Davis 8.4. is employed for the computation of the particles trajectories in the tomographic measurement. Due to the complexity of this tool, additional attention should be given. For instance the number of processing parameters is multiple times the number for planar PIV. Thus, all the parameters must be set accordingly to ensure a successful processing.

The STB settings are displayed in table 4.2. It includes the definition of the volume, particle detection criteria, OTF adjustment and an estimate of the particles displacement and acceleration limits. The parameter "maximum relative change in particle shift" is found to have a strong influence on the total number of tracks detected by STB. This parameter defines the allowed shift that a particle can change between time instances, in other words, the maximum acceleration. An assessment on this parameter is carried out to capture as much tracks as possible.

Table 4.2: STB parameters setting.

Category	Parameter	Value	Unit
Particle detection	2D intensity threshold	20	[counts]
	min. particle intensity (of avg. intensity)	0.1	[-]
	Close particles removal	1	[vox]
	Max. triangulation error	0.5	[vox]
Optical transfer function	Size factor	1.1	[-]
	Intensity factor	1	[-]
	Residdum OTF radius	2	[px]
Displacement limits	Max. shift	15	[vox]
	Max. part. shift (abs)	0.8	[vox]
	Max. part. shift (rel.)	40	[%]
Iterations	Shake delta	0.2	[vox]
	Add particles iterations	4	[-]
	Refinement iterations	4	[-]
Tracks settings	Order of polynomial	2	[-]
	Track length	11	[-]

The STB algorithm is executed for multiple limits and the statistics are recorded in the assessment. The statistical results indicate the number of detected particles, the number of tracks and the number of continuous tracks. The collected information is used to generate the plot in figure 4.2. It can be seen that the number of detected tracks increases rapidly for small shift values and it stabilizes at around 40%. This trend indicates that the flow in the junction has a relatively high acceleration. For this reason a considerable amount of tracks are discarded by the code when the limits are set too low. Hence, the "maximum relative change in particle shift" is set to 40%. Note that a higher number of tracks could also introduce more bad tracks in the results, which would need to be filtered in the post-processing

(section 4.3). The parameters on the minimum length of the tracks can also be set. In the
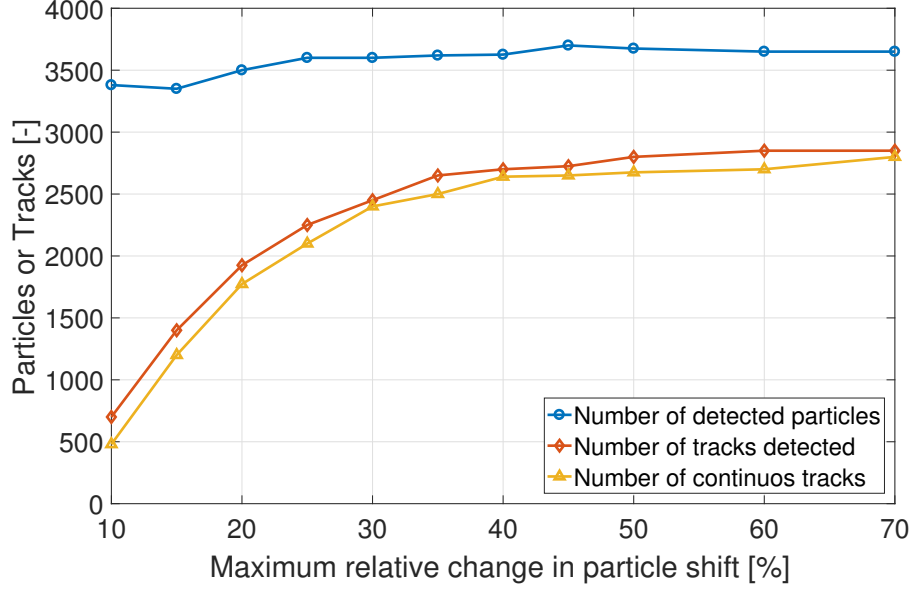
Figure 4.2: Number of detected tracks in function of acceleration limits.

present work, a long track length is preferred because the number of spurious trajectories is then reduced. According to Schanz et al. (2016), (ghost) particles, which do not hold up a coherent trajectories across time steps, are hardly reconstructed by the STB algorithm. In this way, the requirement for long tracks criterion acts as a first filter in eliminating outliers.

4.3   Post-Processing

As the calculated velocity fields are not free of errors, it is part of the data analysis process to filter out outliers. Two data filtering techniques are proposed in this section and an assessment on the filtered velocity fields is presented. The filter that presents better performance will be selected for post-processing the results.

4.3.1   Confidence level filter

The confidence level is one of the most straightforward tools to reject outliers in a batch of data samples. The filter considers a data point as an outlier when its value falls beyond certain confidence value defined by the user from the mean. The mean value of velocity is defined as:

$$\overline{U} = \frac{1}{N} \sum_{i=1}^{N} U_i \tag{4.1}$$

being U_i the streamwise velocity population within a bin. The same procedure can be performed to spanwise (V) and normal (W) component of the velocity. The standard deviation of the corresponding bin is defined as:

$$\sigma_x = \sqrt{\frac{1}{N-1} \sum_{i=1}^{N} (U_i - \overline{U})^2} \tag{4.2}$$

The confidence level is designated as n times of σ from the mean. Thus, a velocity vector is considered for the statistics if and only if its value is within the defined dispersion. Otherwise the velocity point is discarded from the population.

$$\forall |U_i - \overline{U}| > |n \cdot \sigma_x| \Rightarrow outlier \tag{4.3}$$

The filter can be applied to the data set multiple times, as a new value of mean and standard deviation are resulted after each passes. Nevertheless, an excessive number of passes could lead to smoothing of the velocity field.

4.3.2 Universal Outlier Detection

The Universal Outlier Detection is a median based filter proposed by Westerweel and Scarano (2005) for PIV data. This filter determines outliers by comparing a threshold value with the normalized residual of the velocity. With this approach, the filter works both in laminar and turbulent flow regimes with similar performance, which gives the universal character of the filter. To employ this filter, the residual of the velocity (equation 4.4) and its median value are calculated (equation 4.5). U_m in equation 4.4 denotes the median value of velocity.

$$r_i = |U_i - U_m| \tag{4.4}$$

$$r_m = median\{r_1, r_2, r_3...r_n\} \tag{4.5}$$

The residual value is normalized with the median:

$$r_i^* = \frac{r_i}{r_m + \epsilon} \tag{4.6}$$

ϵ in equation 4.6 defines the fluctuating level in the measurement data.

Note the presented normalized residual value is for one single component, the process is repeated for other components and the magnitude of the residual is calculated. A velocity vector is then considered outlier if the calculated residual magnitude is higher than the user defined threshold (r_{th}^*). The lower the normalized residual threshold, the stricter the outlier detection criterion is.

4.3.3   Filter comparison

Two data filtering strategies have been presented. The confidence level filter is tested with acceptance levels of 2σ and 3σ with two filter passes each. The confidence interval achieved with 2σ and 3σ are 95.4% and 99.6% respectively. The universal outlier detection is tested with threshold value of 2.5 and 3, and an acceptable fluctuation of 0.2. The filtered data is then averaged in cubic bin cells of $5 \times 5 \times 5\ mm^3$.

(a) Unfiltered.   **(b)** Mean filter 2σ.   **(c)** Mean filter 3σ.   **(d)** Median filter r_{th}^* = 2.5.   **(e)** Median filter r_{th}^* = 3.
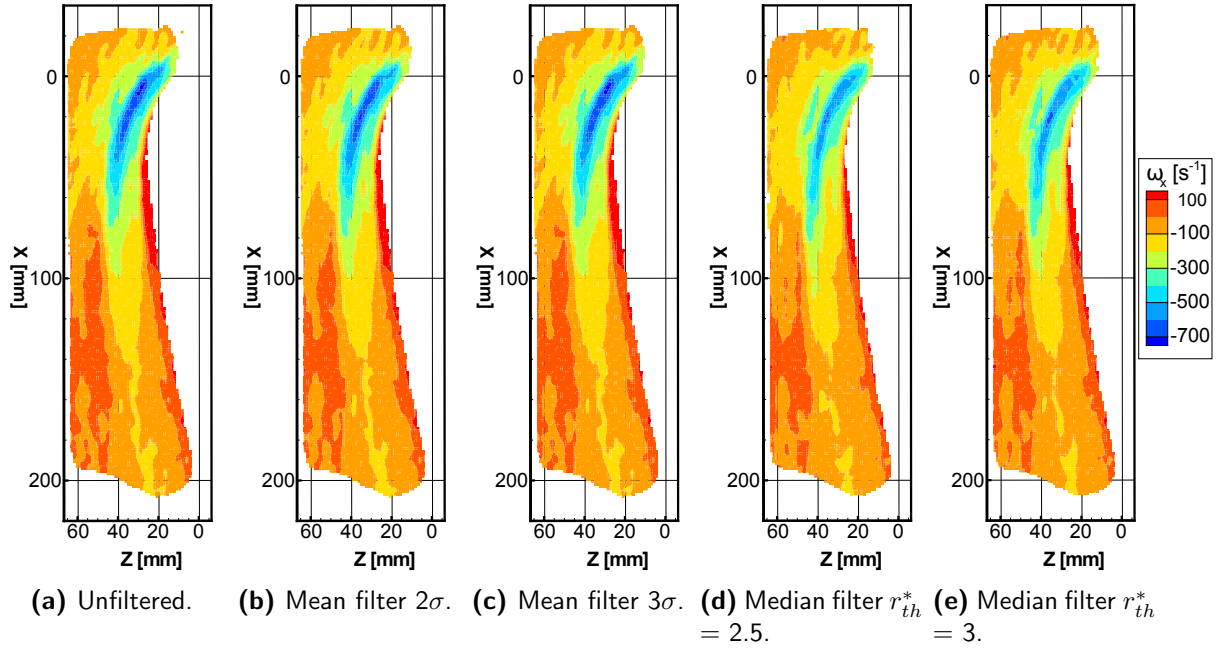
Figure 4.3: Comparison of different filter on the ensemble average of PTV data with 300 burst cycles. The shown plane is parallel to the junction wall at a height of y = 6 mm for the clean configure.

Different filtered ensemble averages of the streamwise vorticity are shown in figure 4.3. This quantity is shown because the velocity, regardless the component, has only small changes on the field which hinder the comparison. Compared to the unfiltered case, the median filters have concluded that the peak vorticity at the wing's nose is lower, while it is slightly weaker for the 2σ confidence filter and almost no variation for the 3σ one. Another noticeable change caused by the filters is the shrinkage of the vortex stream at about X = 140 mm. It is possible that the HSV breakdown occurs at this location as the wide of the vorticity contours reduces considerably and becomes less coherent. Again, the median filters indicate that the streamwise vorticity is less intense and only small changes is observed for the confidence filters.

Other quantities are also revised for determining the most suitable filter. For instance, the standard deviation and the remaining particles in the cells after filtering. For the median filters, both quantities are less than all other cases, while for the mean filters, these values are slightly lower in the 2σ case and almost no changes for the 3σ mean filter. These values

at some particular locations, indicated in figure 4.4 are shown in table 4.3. These results have a strong implication on the filter that will be used to post-process all the data. First of all, the lower value of standard deviation from the median filter could indicate the data set is over-smoothed. Although its effect is not reflected on the averaged velocity field, it reduces the calculated turbulence level. Secondly, if the remaining number of particles in the bin cells is reduced, the statistical convergence could be not reached. Viewed differently, the uncertainty of the bin is also higher due to less particle samples.

Table 4.3: Value of standard deviation and remaining particles of after applying different filters. The locations are indicated in figure 4.4

	Freestream (Point 4)				Core (Point 3)			
	σ_x [m/s]	σ_y [m/s]	σ_z [m/s]	Particles	σ_x [m/s]	σ_y [m/s]	σ_z [m/s]	Particles
Unfiltered	0.855	0.459	0.477	1292	1.179	1.253	1.323	941
2σ	0.611	0.418	0.461	1250	0.855	1.206	1.319	921
3σ	0.855	0.459	0.477	1292	1.178	1.252	1.323	933
$r_{th}^* = 2.5$	0.598	0.348	0.397	1098	0.811	0.815	0.889	672
$r_{th}^* = 3$	0.665	0.380	0.419	1168	0.896	0.990	1.019	765

For the given observations, the mean filter with 2σ is applied to the data as outlier detector. This filter is preferred over the median filter because it is less aggressive in discarding data samples. Additionally the value of standard deviation is not as heavily biased. The 3σ mean filter is not selected because the confidence level is extremely high. As a result, almost all the data samples are included for the ensemble average, resulting almost no filtering effect in the velocity field.

4.4   Grid transformation

The output from the STB algorithm are particles trajectories. This form of velocity data representation is more precise as each velocity vector represents a unique position in space. However, this property complicates the analysis process, specially when it involves the calculation of spatial gradients: as the data is scattered in space the gradient is not uniform between neighbours. For this reason, it is preferred to transform the trajectories into a structured grid before proceeding to the analysis. Since the spatial gradient is then uniform across grid cells. Nevertheless, grid transformation has the disadvantage of spatial averaging. Hence, the cells or bins must be sufficiently small to minimise the spatial modulation but at the same time big enough to include sufficient sample points and reduce the uncertainty.

In a first approximation, the grid cell length can be determined by the following equation proposed by Agüera et al. (2016):

$$l = \sqrt[3]{\frac{N_{min}}{N_{eff} \cdot C}} \tag{4.7}$$

N_{min} is the minimum number of samples required in a fluid cell, which is defined in the design of experiment in section 3.4.2, N_{eff} is the number of effective samples and C the seeding concentration in $bubbles/cm^3$. In the current study, the number of effective samples can be approximated as the number of burst cycles. However, in the case of time-resolved measurement, the effective number of samples differs from the number of recorded images because the flow structures are correlated in space and time. In such situation, the effective number of samples can be estimated as the ratio of acquisition period (T_{aq}) and the characteristic time scale of the flow (T).

$$N_{eff} = \frac{T_{aq}}{T} \tag{4.8}$$

In this work, a bin cell length of approximately 4 mm is resulted by considering N_{eff} the number of burst cycles.

The ensemble average of the velocity field on each cell is performed using Gaussian weighted average, centred on the cell. In other words, a velocity vector has more influence on the final mean value the closer to the cell centre it is.

4.5   Convergence analysis

After the ensemble average of the particle tracking data, the convergence analysis is performed. This analysis aims to find out the minimum number of samples required to have a consistent average value. It is important to ensure statistical convergence as otherwise bias is introduced into the mean value.

The speed of convergence highly depends on the nature of the flow. In laminar flow, the convergence is reached rapidly because of the low fluctuating level; while in turbulent flow the convergence is slower. However, it could also be the case that the convergence is hardly reached by an unsteady flow. For instance, the meandering effect of the HSV in junction flow keeps the flow oscillating between two extreme positions, resulting high standard deviation. Therefore, the convergence analysis is performed to various locations to evaluate the effect of different flow natures on the convergence, see figure 4.4. The locations where the convergence is analysed are: freestream flow far away from the junction (points 1 and 4), close to the HSV leg core and its outer region (points 2 and 3) and the junction close to the trailing edge (point 5).

Nevertheless, if the mean velocity converges with less than the total available samples and the uncertainty value is not a concern, the spatial resolution of the ensemble average can be increased by introducing a smaller bin size; the other way around, if it does not converge, one could trade-off the spatial resolution for a better statistically converged result. For this reason, apart from analysing the convergence with a bin size of 4 mm, it is also analysed for bin sizes of 3 and 5 mm.

The convergence plot of the normal velocity is displayed in figure 4.5. The quantity selected
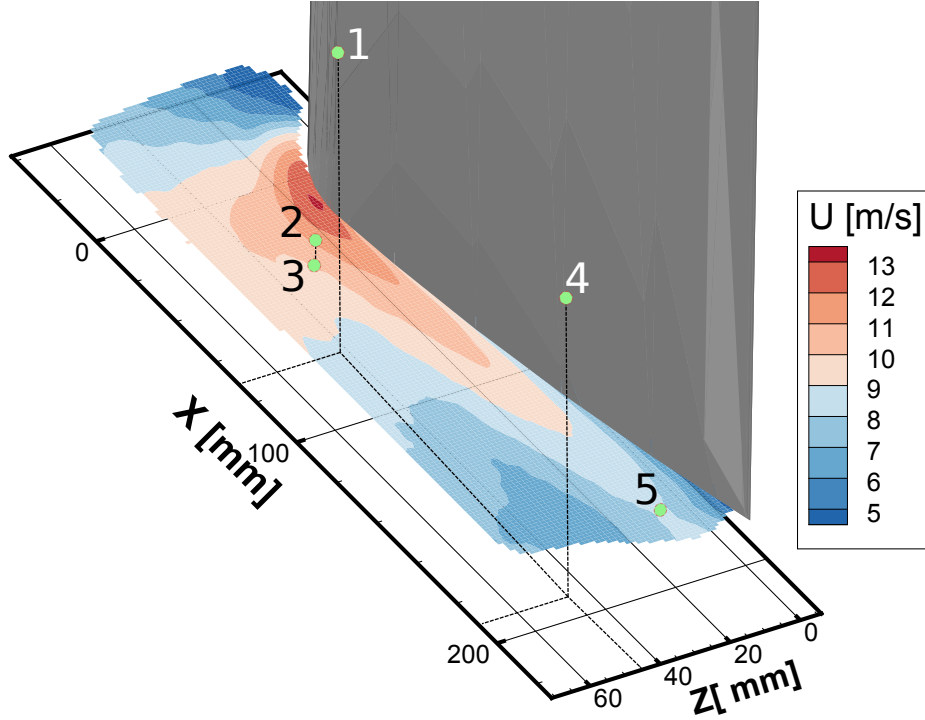
Figure 4.4: Locations in the flow field where the convergence analysis takes place.

as decisive, and thus shown, is the normal velocity (W) as its convergence rate is slower than the streamwise velocity. It can be observed from the plot that the normal velocity at the freestream converges almost immediately with a few hundreds of cycles regardless the cell size. The turbulent regions also converge relatively quickly after approximately 300 cycles for the 5 *mm* bin size, and about 400 for the 3 and 4 *mm* bins. More cycles could be included to calculate the fields and reducing the uncertainty.

During the experiment, the burst cycles of the VG in spacing configuration were not recorded correctly. However, the ensemble average could still be calculated with the time resolved measurement. Since each frame of the TR data is correlated between each other, the effective number of samples has to be calculated with equation 4.8 with the successive equation 4.9. The TR ensemble average is converged if the resulted number of samples is close to the convergence value. The characteristic time scale of the flow can be calculated by means of autocorrelation. Autocorrelation is a mathematical tool that measures the time for a pattern to repeat itself on a given time signal (Box and Jenkins, 1976). The autocorrelation coefficient is defined as:

$$R(\tau) = \frac{\sum\limits_{i=1}^{N-\tau} U'(t) \cdot U'(t+\tau)}{\sum\limits_{i=1}^{N} U'(t)^2} \tag{4.9}$$

τ and $U'(t)$ are the time delay and the fluctuating part of the velocity signal respectively. The autocorrelation coefficient is calculated for all three velocity components and the component that presents the longest characteristic time is adopted for the characteristic time scale. The
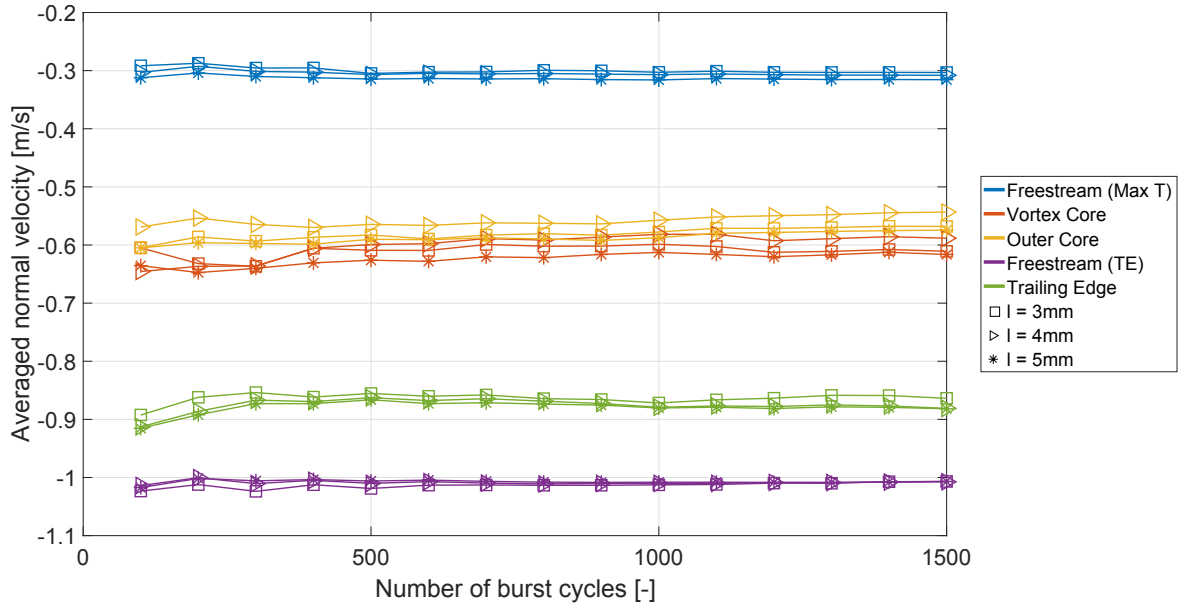
Figure 4.5: Convergence plot for the different location and different bin cell length.

velocity-time series is acquired by Gaussian averaging velocities vectors that are within a large cubic interrogation volume for each time step. The need for a large volume is to compensate the low particle concentration of the flow, as a large volume has high probability to acquire particles in all time steps. Figure 4.6 shows the fraction of the time series in which the interrogation volume has not captured any particle. A volume of $10 \times 10 \times 10 \ mm^3$ is selected to extract the velocity signal as it yields a relatively low empty space fraction. The times instances which do not have any velocity vectors are interpolated. The location of the volume is set to be around the vortex core position at 65% of the chord length. At this point, the meandering effect of the HSV is dominant and its frequency is expected to be captured by the autocorrelation analysis.

The autocorrelation coefficient is evaluated and presented in figure 4.7. The series is considered to be uncorrelated in time when the autocorrelation coefficient drops below R = 0.15. The corresponding integral time scale for this threshold value is $1.8 \ ms$. Note the streamwise velocity is considered as it returns the longest time scale. The time-resolved measurement has a total number of ten thousands images acquired at $5 \ kHz$ of acquisition frequency, thus, the acquisition period is $2 \ s$. The effective number of samples is then calculated using equation 4.8, resulting 1,111 uncorrelated samples. Given the fact that the number of uncorrelated samples is higher than the required for statistical convergence, it can be concluded that the time-resolved data is suitable for the flow analysis.
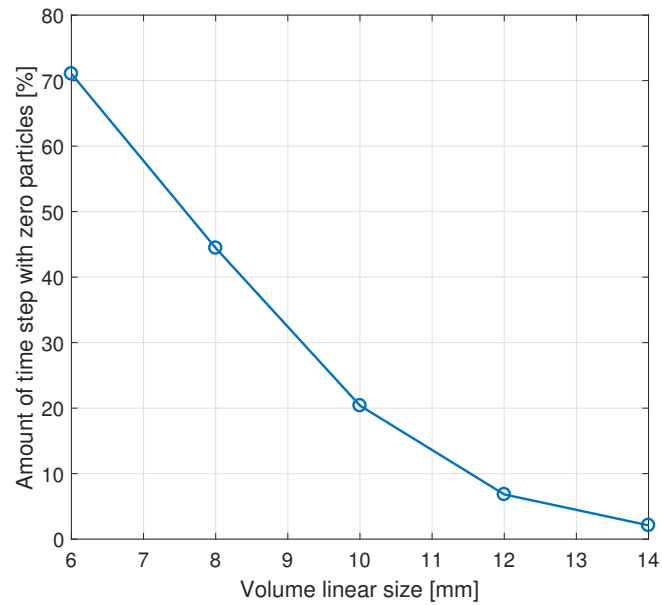
Figure 4.6: Percentage of zero particles in the velocity time series in function of interrogation volume size.
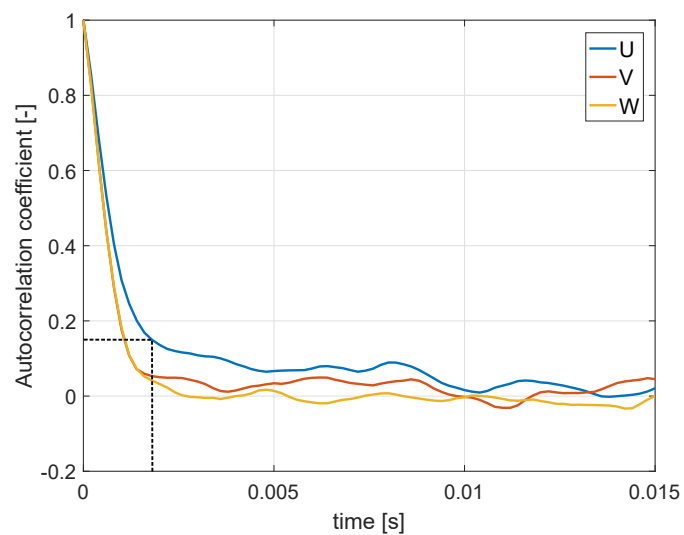
Figure 4.7: Autocorrelation coefficient of the time series acquired at 65% of the chord around the vortex core in the VG in spacing configuration.

4.6   Uncertainty analysis

The uncertainty of the measurement can be quantified using equation 4.10. The uncertainty depends on the standard deviation of the samples, the coverage factor k, which both together define the confidence interval, and the square root of the number of uncorrelated samples.

$$\epsilon = \frac{k\sigma}{\sqrt{N_{un}}} \tag{4.10}$$

In the case of the sPIV measurement, the number of uncorrelated samples is equal to the number of velocity fields obtained, which is 1000. The uncertainty of the wake field is measured in three locations: freestream, close to the vortex core wake and in the boundary far away from the vortex wake. These locations are shown in figure 4.8. The results of the uncertainty assessment are shown in table 4.4.
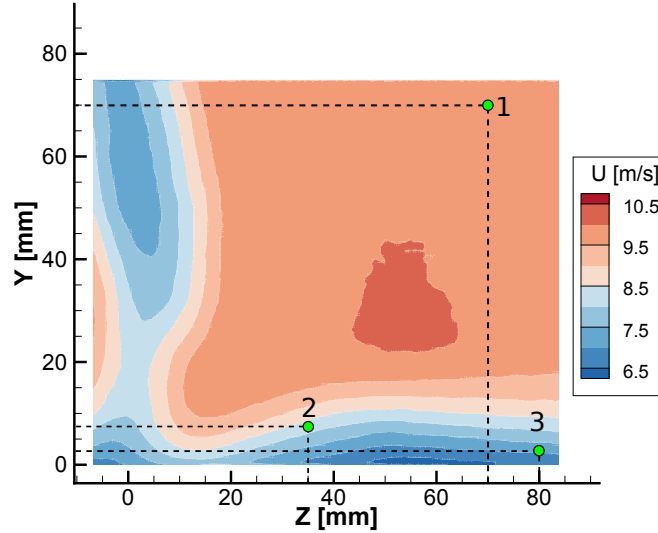
Figure 4.8: Locations in the wake where the uncertainty is measured.

Table 4.4: Velocity uncertainty calculated in the wake measurement.

	Freestream (Point 1)			Core (Point 2)			Boundary (Point 3)		
	ϵ_x	ϵ_y	ϵ_z	ϵ_x	ϵ_y	ϵ_z	ϵ_x	ϵ_y	ϵ_z
				‰ of the freestream					
Clean	0.8	0.7	2.2	3.7	3.3	5.0	3.5	2.8	5.2
Fairing	0.8	0.6	2.1	3.5	3.1	5.1	3.4	2.7	5.0
VG (Series)	0.8	0.6	2.0	4.1	3.6	5.4	3.5	2.8	5.2
VG (Spacing 1.5T)	0.7	0.6	2.0	3.6	3.3	4.9	3.4	2.7	4.9
VG (Spacing 1T)	1.1	0.8	2.8	3.9	3.4	4.8	3.2	2.7	5.2
Antifairing	1.1	0.8	2.8	3.0	3.0	4.5	3.5	3.0	5.6

For the tomographic measurements, the number of burst cycles can be considered as the number of uncorrelated samples. This reasoning is sound because each burst cycle is separated from the subsequent ones by a large time separation, hence the cycles are uncorrelated in time.

In the case of the time-resolve data, the number of effective samples, measured with equation 4.8, is not strictly equal to the number of uncorrelated sample as it depends also on the concentration. Given a single TR effective sample and transformed into a structured grid, not all bin cells would have captured at least one particle due to the low seeding concentration of large-scale PTV. As a result, the velocity field with such sample would have cells that do not have any velocity information. In such matter, a TR effective sample should not be considered as an uncorrelated sample as its field is incomplete. A correction factor is defined to work around this problem. It is shown as the multiplier of equation 4.11. This factor takes the minimum between particles that are in a bin cell, which depends on the seeding concentration and the considered cell size, and unity. In this way, if the number of particles in a bin cell is less than one, more TR effective samples are needed to compose an uncorrelated sample, otherwise they are equivalent.

$$N_{un} = N_{eff} \cdot min\{C \cdot l^3, 1\} \tag{4.11}$$

Applying equation 4.11 on the calculated number of TR effective samples, 390 uncorrelated samples are obtained. Although the number of valid uncorrelated samples is slightly less than the convergence value, it is considered to be acceptable for the current study.

The uncertainty is calculate for the ensemble averaged velocity field, for each velocity component and each configuration. The ensemble average of the VG configuration is build upon TR data, thus, higher uncertainty is expected. Various locations(vortex core, freestream and trailing edge as indicated in figure 4.5) are selected for the uncertainty calculation, whose values are summarized in table 4.5. Higher numbers are found to be located at the core and close to the trailing edge regions in all configurations, which could be linked to the turbulence and unsteadiness of the HSV.

Table 4.5: Velocity uncertainty calculated in the ensemble average of all configurations.

	Freestream (Point 4)			Core (Point 3)			Trailing Edge (Point 5)		
	ϵ_x	ϵ_y	ϵ_z	ϵ_x	ϵ_y	ϵ_z	ϵ_x	ϵ_y	ϵ_z
	‰of the freestream								
Clean	0.6	1.1	1.4	3.9	4.4	4.2	3.6	2.2	2.8
Fairing	0.6	1.0	1.3	3.2	2.8	3.2	4.7	2.6	3.4
VG Spacing	1.4	2.6	3.6	9.8	12.4	12.1	10.2	5.5	7.4
Antifairing	0.6	1.0	1.2	4.0	4.9	4.4	2.5	1.8	2.2

During the process of grid size assessment, it is observed that the peak streamwise vorticity of the HSV decreases with the grid size. The diminution is attributed the high velocity gradient close to the vortex core, which cannot be resolved with the selected bin size and thus, the vorticity value suffers from the spatial modulation effect. Consequently, a bias on this quantity is present and is a source of error which should be taken into account. To narrow down the uncertainty, an estimation on the true peak vorticity is performed and the difference with the binned data would infer the systematic error in the results.

Assuming the peak vorticity increases with the cell size and decreases with smaller ones up to a certain limit (the true peak vorticity), a series of data points can be obtained by constructing the ensemble average with different size.

To estimate whether the true peak vorticity is achieved, multiple ensemble average with different cell size are reconstructed around the vortex. The peak vorticity value is then recorded for each grid size. Smaller grid is preferred as its vorticity value is closer to the true one, but it should be bared in mind that the noise level also increases due to less particles are in the bin. Once the data points are obtained, it can be fitted with a polynomial and extrapolated to smaller grid size. The result of the estimation is shown in figure 4.9. It can
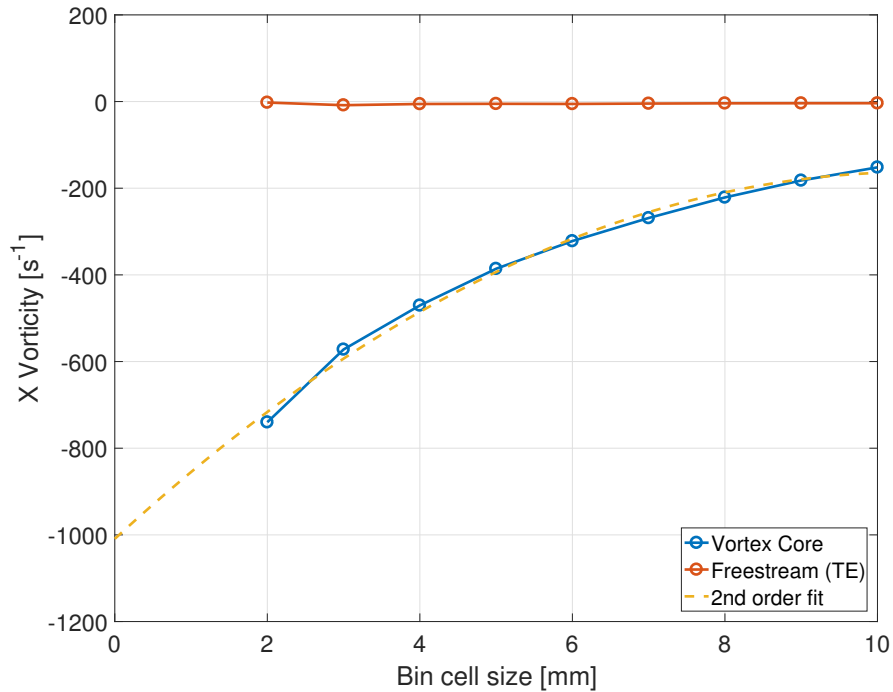
Figure 4.9: Peak vorticity value in function of cell size.

be concluded that the peak vorticity has not been reached yet, as the measured peak vorticity in function of the grid size is continually decreasing with the smaller cell size. No further data points are obtained as the noise level surpasses recognisable level. In the worst case scenario, the true peak vorticity takes the value of -1000 s^{-1} at zero grid size. The difference with the peak vorticity measured in the same location but with a grid of 4 mm is -530 s^{-1}. Although the peak vorticity difference is relatively high, it reduces only the local accuracy of the vorticity field, which is a relatively small area of about 1.5 × 1.5 mm^2 (the vortex core size). Nevertheless, the limit in calculating the peak vorticity does not suppose a major shortcoming when comparing different configuration, as it is more relevant the difference in vorticity across configuration than measuring the absolute value.

4.7 Flow Analysis

The processing techniques discussed so far are adopted in order to obtain the time-averaged velocity fields of the junction flow as precise as possible. Then, the flow is analysed to reveal the vortical structures. In the subsequent sections, the analysis techniques such as wake characterization, vortex identification method, and turbulent level determination are briefly explained.

4.7.1 Momentum Deficit

This flow analysis only applies to results from the sPIV measurement, as the momentum deficit survey is more accurate at the wake region where influences of the model is minimum.

The momentum deficit analysis estimates the force which contributes the most to the drag. The results from the different configuration will be used to compare the performance. The idea of this analysis is that an undisturbed flow loses its kinetic energy after passing through an obstacle. The energy lost is attributed to the friction with the model and the effect of the reduced velocity (wake) is captured downstream. By applying the momentum balance between the freestream and the wake, the difference yields the drag.

$$MD = \rho \int_S U \cdot (U_\infty - U)dS \tag{4.12}$$

This quantity is defined as the surface integral of the product of streamwise velocity at the wake and its difference with the freestream velocity (equation 4.12). The application of the equation is valid if certain assumptions are considered. For instance the flow is incompressible and the plane of measurement is perpendicular to the streamwise velocity Anderson (2010). Only velocity in the streamwise direction is considered because this is the component relevant to the drag. Following this basis, the lift force or side force could also be determined if the normal and spanwise velocity are considered respectively.

4.7.2 Vorticity

Vorticity is defined as as the curl of the velocity field. This quantity describes the rate of change in the flow direction (circulation) and velocity gradient (shear). Nonetheless, for a given vorticity value, it cannot distinguish the source of either as the two effects are coupled.

$$\vec{\omega} = \nabla \times \vec{u} = \begin{bmatrix} \frac{dW}{dy} - \frac{dV}{dz} \\ \frac{dW}{dx} - \frac{dU}{dz} \\ \frac{dV}{dx} - \frac{dU}{dy} \end{bmatrix} \tag{4.13}$$

4.7.3   Q-criterion

Facing the shortcoming of vorticity on identifying vortices or shear layers, Hunt et al. (1988) proposed a method which decouples the two effects called Q-criterion. This method begins with the calculation of the velocity gradient tensor, which is then decomposed into a symmetric tensor S and antisymmetric tensor Ω. Each elements of the two tensors are defined as:

$$S_{ij} = \frac{1}{2}\left(\frac{\partial u_i}{\partial x_j} + \frac{\partial u_j}{\partial x_i}\right) \tag{4.14a}$$

$$\Omega_{ij} = \frac{1}{2}\left(\frac{\partial u_i}{\partial x_j} - \frac{\partial u_j}{\partial x_i}\right) \tag{4.14b}$$

The Q-criterion, symbolized as Q, is expressed as the difference in magnitude of S and Ω.

$$Q = \frac{1}{2}(|\Omega|^2 - |S|^2) \tag{4.15}$$

The modulus of Ω and S defines the local vorticity magnitude and the shear rate. Hence, a positive value of Q implies the presence of a vortex and negative for a shear layer.

4.7.4   Circulation

It has been shown that a vortex can be recognized using the Q-criterion. Nevertheless, the value of Q does not report the vortex strength. In account for this limitation, the circulation (Γ) can be employed to estimate the vortex strength.

$$\Gamma = \oint_C \vec{u} \cdot dl = \int_S \vec{\omega} \cdot dS \tag{4.16}$$

The circulation is defined as the line integral of the scalar product of velocity and the tangent of the closed curved. By applying the Stokes theorem, the same expression can be written in function of the vorticity and the area enclosed by the curve.

As the circulation highly depends on the selected area for its determination, it is recommended to calculate it in an area enclosed by a contour line of a certain vorticity value. In such a way a larger vortex would have higher contribution due to the increased area. Nevertheless, a rectangular shaped integral surface, centred to the vortex core, could be adopted for a simpler calculation. As then it mainly accounts for the the peak vorticity. This window must have the same surface area if a comparison between configurations is performed.

4.7.5   Turbulence level

The intensity of the velocity fluctuation around the junction is studied by means of the normal components of the Reynolds stress (R_{xx}, R_{yy} and R_{zz} for each component). The reason for studying the three components separately is due to the anisotropy of the flow. This analysis

has a special interest in the practical application such as a junction flow introduced in a wind tunnel, which is the motivation of this thesis. In such configuration, the disturbances could be increased in certain direction, hence the uncertainty. Consequently, the results obtained from an experiment performed in this wind tunnel would be biased, specially if it is more sensitive toward the disturbed direction.

Chapter 5

Results and discussion

This chapter describes the results on the performed junction flow experiments. First of all, the flow conditions are introduced and the flow at the wake region, measured with sPIV, is characterized. This initial analysis allows the recognition of the outperforming configurations among all. These configurations are the ones further studied by measuring their junction flow with large-scale tomographic PTV technique. To conclude this chapter, the working mechanism of the control devices on the HSV is proposed based on the obtained results. The results presented in this chapter are normalised with the Rood wing maximum thickness and/or freestream velocity.

5.1   Flow Condition

As mentioned in the experimental setup in chapter 3, all tests are conducted with a flow velocity of 10 m/s. The flat surface is tripped at the beginning of the transparent test section. The boundary layer profile is assessed with planar PIV at the presumed wing's leading edge position without the model.

The BL profile is shown in figure 5.1. The BL thickness (δ) is about 0.6T, the calculated displacement thickness (δ^*), momentum thickness (θ) and the Reynolds based on these number are summarized in table 5.1. The boundary layer is turbulent as according to Schlichting et al. (1955), the shape factor is around 1.4.

Table 5.1: Boundary layer properties.

δ	0.6T | 28.5 [mm]	H	1.48
δ^*	0.096T | 4.6 [mm]	$Re_{\delta*}$	3194
θ	0.065T | 3.1 [mm]	Re_θ	2153

The turbulence level increases the closer to the wall is up to a peak value, then it drops to zero on the wall as no velocity exist. The measured maximum value is about 10%, however, it might not represents the peak turbulence level due to the limited spacial resolution of PIV. The freestream turbulence level is about 1%.
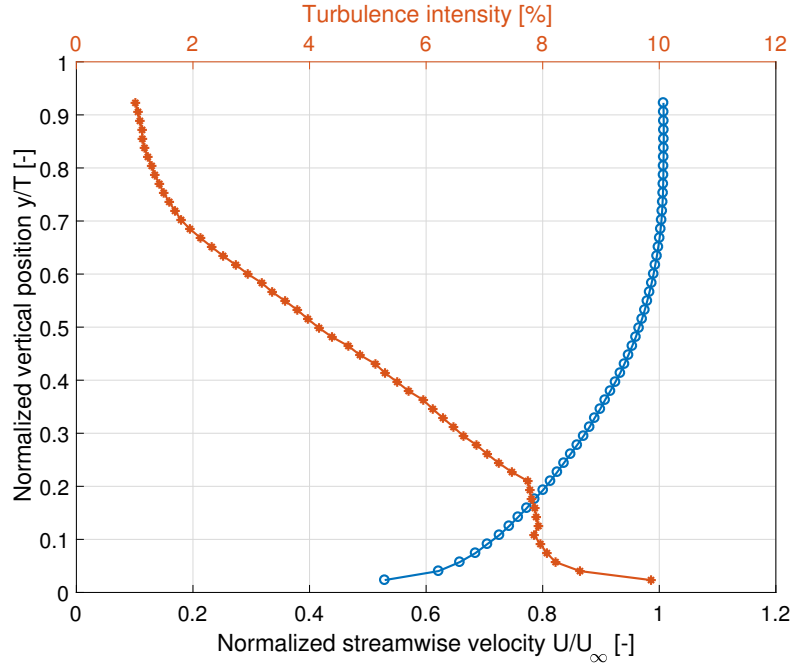
Figure 5.1: Boundary layer profile at the wing's leading edge position.

5.2 Wake Survey

Results of the wake measurements are displayed in this section. The discussion is focused on the time averaged velocity, vorticity and the associated momentum deficit and turbulence level at the wake at $x/T = 7.67$ downstream from the wing leading edge. These measurements are taken in a plane normal to the freestream velocity. The results of the clean configuration are discussed first in order to define the reference flow features of the junction flow.

5.2.1 Clean Configuration

Velocity and vorticity field

The streamwise velocity of the clean configuration, displayed in figure 5.2, shows a reduction of freestream velocity at two locations: the wake of the wing ($z/T = 0$) and the flat plate boundary layer ($y/T \lesssim 0.5$). Note the velocity field is not exactly symmetric with respect to the symmetric plane ($z/T = 0$), given that the wing model has one side rougher than the other due to manufacturing issue. As a result, the flow transitions at a different point on each side and a small cross flow is induced downstream of the trailing edge. To force the flow transition to occur at a similar point, zigzag tape has been used. Although the cross flow intensity is reduced, a small effect is still present. Given such situation, less attention is given to the wing's wake as this effect is repeated in all configurations and does not change significantly.

A swirl flow is observed at the juncture area and the streamwise velocity is higher than the surrounding. This flow is transporting high momentum flow to the BL junction. As a result, the momentum deficit is reduced locally. This observation is the result of the HSV wake, whose presence is barely visible. In addition, the vortex also introduces a cross flow at the boundary, creating hence a three dimensional boundary layer.

At about z/T = 0.75, the height of low streamwise velocity region is faintly greater than the outer region and the flow deflection occurs around this point. This infers the location of the time averaged HSV. The vorticity field can also be plotted to support this basis, where a region of high intensity is expected.

The streamwise vorticity contour is provided in figure 5.3. The intensity is indeed higher in absolute value at the aforesaid position than in other regions. The vorticity associated with the HSV has a negative sign and counter-clockwise rotation in the represented results, on the measured side of the wing. Nevertheless, the vortex is not located in a single point but in a area. This could due to the fact that the HSV does not hold a coherent structure at the wake but has already broken down into smaller structures. More details are discussed in section 5.3.2. As the product of the vortex breaks down, the flow becomes more turbulent. Besides, due to the high turbulence level, the vorticity field is not completely converged, which introduces additional difficulties in the interpretation of this quantity.
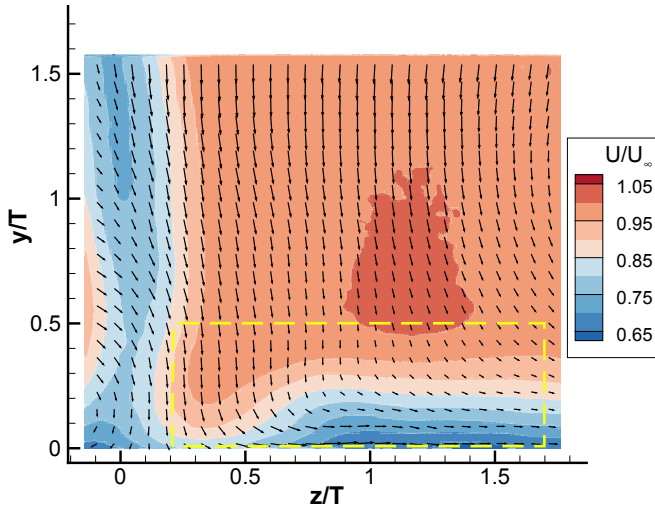
Figure 5.2: Contour of the streamwise velocity at the wake. Yellow box defines the area where the momentum deficit is calculated
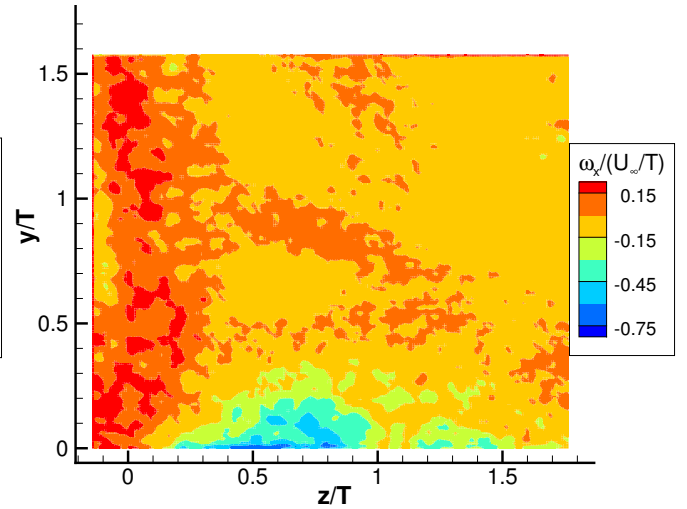
Figure 5.3: Contour of the streamwise vorticity at the wake.

5.2.2 Comparison with other Configurations

Velocity and vorticity field

The wake measurements of the junction with passive flow control devices are presented in figure 5.4.

(a) Fairing.

(b) VG in series.

(c) VG in 1T spacing.

(d) VG in 1.5T spacing.

(e) Antifairing.
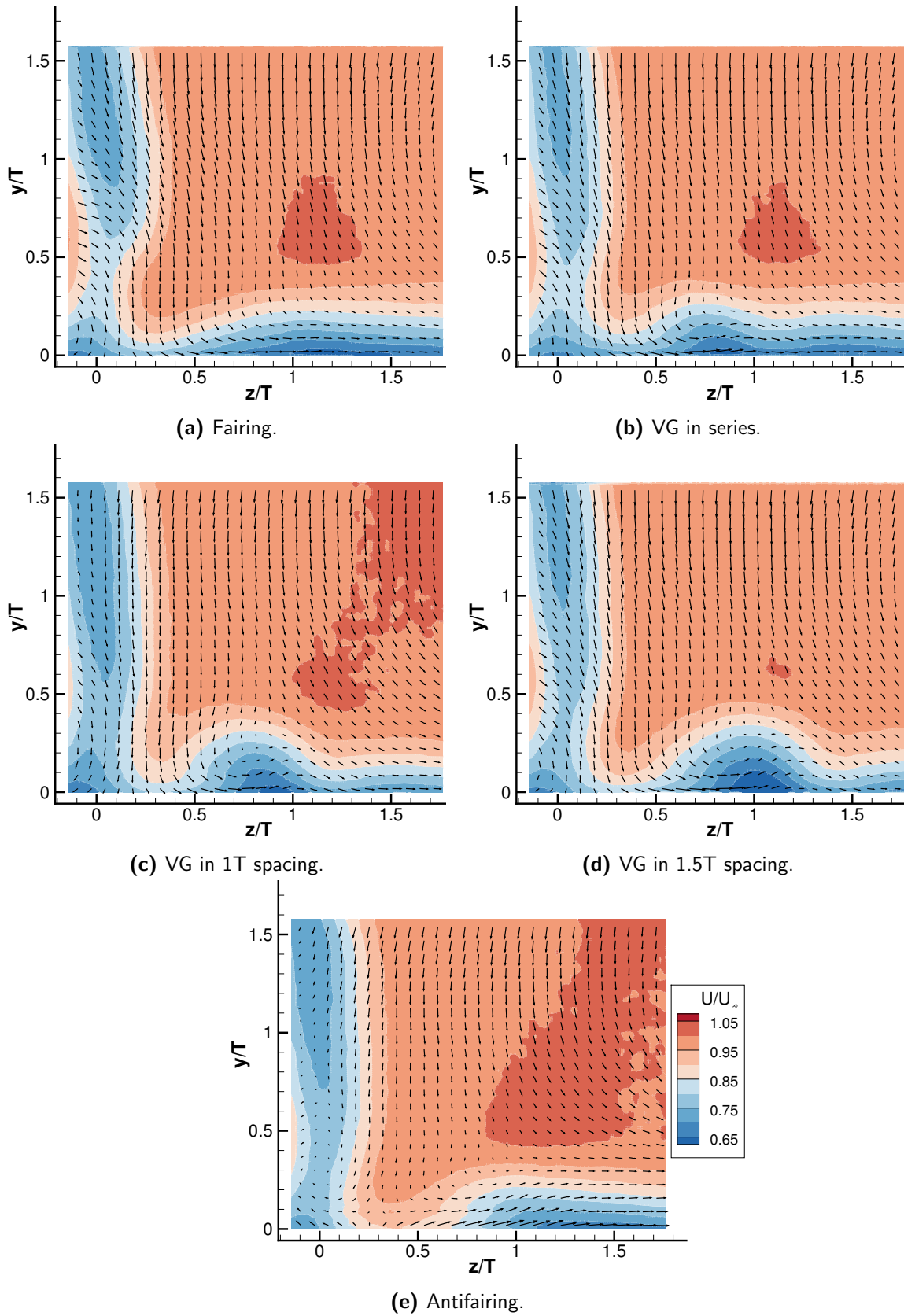
Figure 5.4: Streamwise velocity of the wake with different control devices

The streamwise velocity of the fairing configuration is relatively similar to the clean config-
uration. The only appreciable difference is that the freestream velocity close to the juncture
region (z/T = 0.4) is not intruded to the boundary as strongly as in the clean configuration.
Nevertheless, the cross flow intensity appears to be similar. These observations suggest that
the vortex associated with the fairing configuration could be located closer to the flat surface.

In regards to the vortex generators configurations, all three have a more pronounced silhouette
of a vortex. The vector fields indicate the vortices have higher influence on the boundary layer
than the clean configuration, as a small amount of flow immediate to the plate is slightly lifted
up. Due to the presence of vortices, the thickness of the boundary layer appears to have a
wavy shape. In addition, a region of low streamwise velocity surrounds the assumed vortex
position, causing the BL to be thicker. However, the BL is thinner than the reference further
away from the vortex. This action is the consequence of the vortex generated by the control
device. As the vortex has an opposite rotation than the HSV, see figure 5.5, it pulls the
freestream flow towards the boundary at the outer region.

For the antifairing, the velocity loss in the junction wake is less pronounced. Furthermore, the
magnitude of the downwash and deflecting flow adjacent to the trailing edge is diminished
compared to the reference. In addition, an upwash larger than in most configurations is
observed next to the wall in the range z/T = [0.5, 1.2]. Both, the higher streamwise velocity
and the upwash flow, are the outcome of the antifairing design, as the dented surface has a
positive slope in the x direction downstream of the wing model.

The streamwise vorticity fields are shown in figure 5.5. Starting with the fairing configuration,
the region with negative vorticity is similar to the one obtained in the clean configuration.
However, the peak vorticity value is found closer to the TE immediate to the flat plate. This
finding explains the crossflow observed on the flat plate.

In the cases of the VG generators, a positive vorticity, or clockwise rotating vortex, associated
with the control device is observed almost coinciding with the HSV core, segregating the
negative vorticity region in two parts. A strong negative vorticity is observed at the inner
part of the junction for the series configuration, but the trace of a positive vortex is relatively
low. This observation is due to the artificially created vortex has not merged with the HSV
core but has only approached to the HSV leg, increasing hence its strength.

The VG in spacing configurations appear to be more effective than the series configuration.
First of all, the intensity of the HSV has not increased; secondly, the positive vorticity is
also introducing high momentum flow from the freestream to the BL. It can be observed as
well as the spacing distance plays an important role in the removal of the HSV: with one
thickness spacing, the positive vortex is closer to the HSV core and both are interacting with
each other, resulting in a smaller and weaker vortex. However, the HSV appears to be larger
when the VG are placed too far away. It can also be noted that the strength of the positive
vortex is higher for the larger spacing, as it has less interaction with the main vortex.

The antifairing configuration has similar characteristics to the fairing case, the only difference
is that the assumed vorticity peak is positioned further away from the wing. This finding ex-
plains why more high momentum fluid is transferred closer to the chord line in the antifairing

(a) Fairing.

(b) VG in series.

(c) VG in 1T spacing.

(d) VG in 1.5T spacing.

(e) Antifairing.
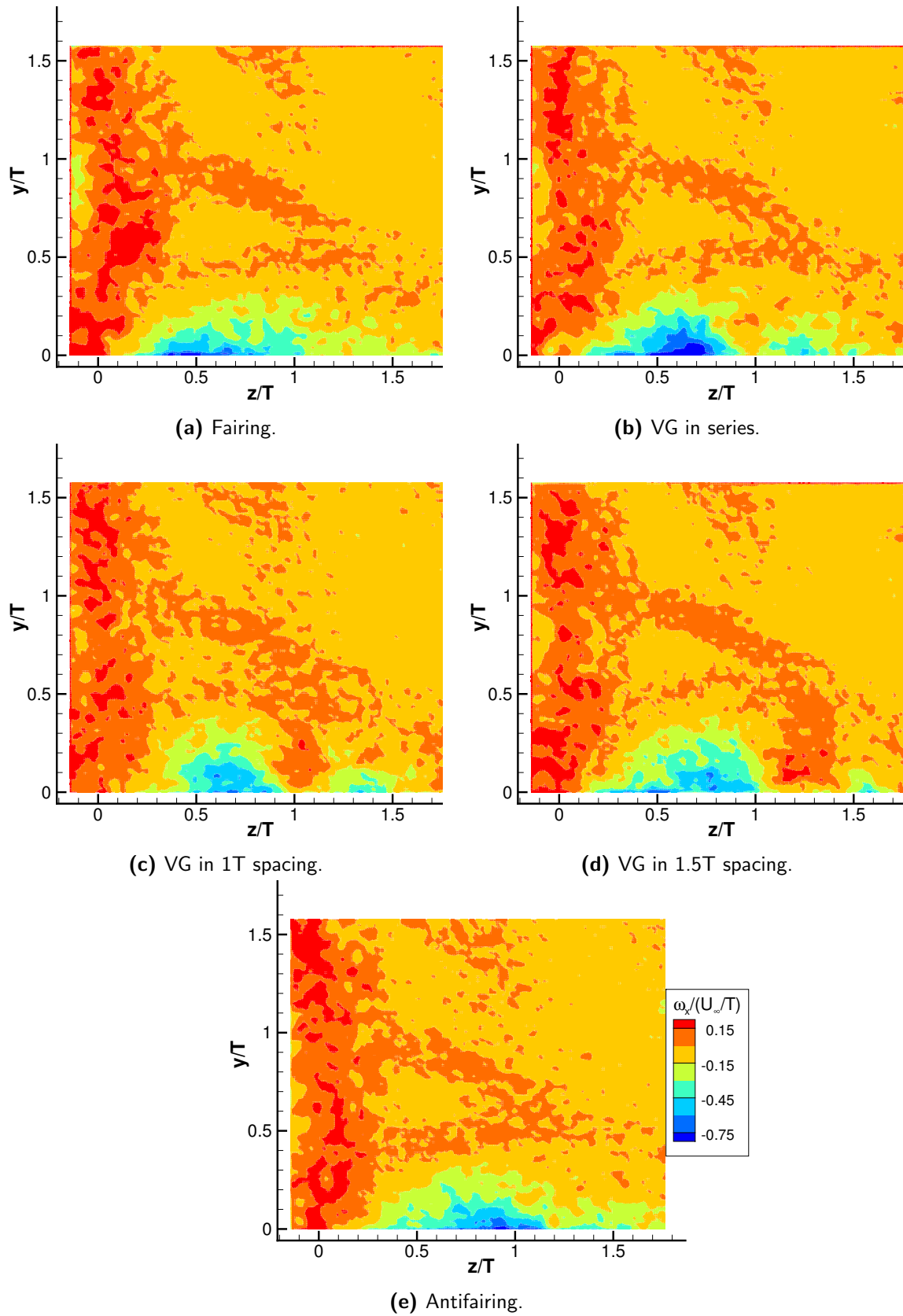
Figure 5.5: Streamwise vorticity of the wake with different control devices

configuration.

Momentum Deficit

The momentum deficit measured in the wake is a good indicator of the drag, even though only a small part of the wake is accounted for in the current study, it allows for comparison of the control devices performance. In order to calculate this quantity, an area enclosing the HSV is adopted (yellow dashed line in figure 5.2). Additionally, the omission of the far field in the calculation reduces the possible error linked to the small differences in freestream velocity or the asymmetric flow.
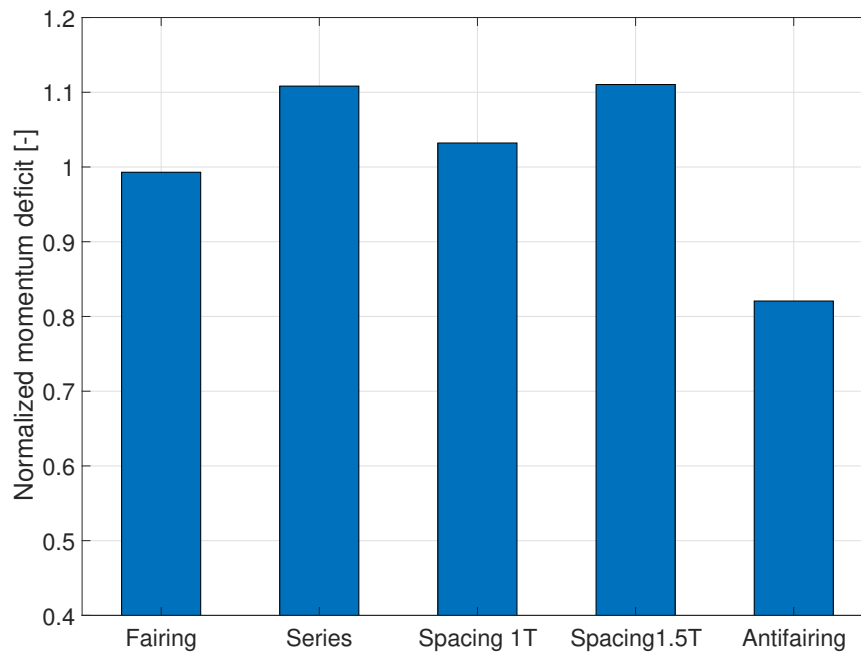
Figure 5.6: Momentum deficit normalized with clean configuration.

In figure 5.6, the measured momentum deficit of the control devices is shown as a fraction of the clean configuration's momentum deficit. The fairing shows a small reduction of about 2%. All VG cases are performing worse than the clean configuration, with the small spacing configuration the one with the least increment. The largest reduction is recorded for the antifairing with up to 17% less momentum deficit in the studied area.

In view of these results, both the VG in series and large spacing configurations are discarded for the tomographic measurement of the junction flow around the model.

5.2.3 Turbulence Intensity

The implementation of a control device depends on its purpose. For instance, reducing the drag or the turbulence downstream of a junction flow. Hence, the performance study based on the turbulence level downstream of the junction flow is assessed in this section.

The principal components of Reynolds stress of the remaining four configurations are shown in figures 5.7-5.9. Regardless the direction, the results indicate the boundary layer has higher values than the freestream region, especially at the vortex location where the highest turbulence level is located.

(a) Clean.

(b) Fairing.

(c) VG in 1T spacing.

(d) Antifairing.
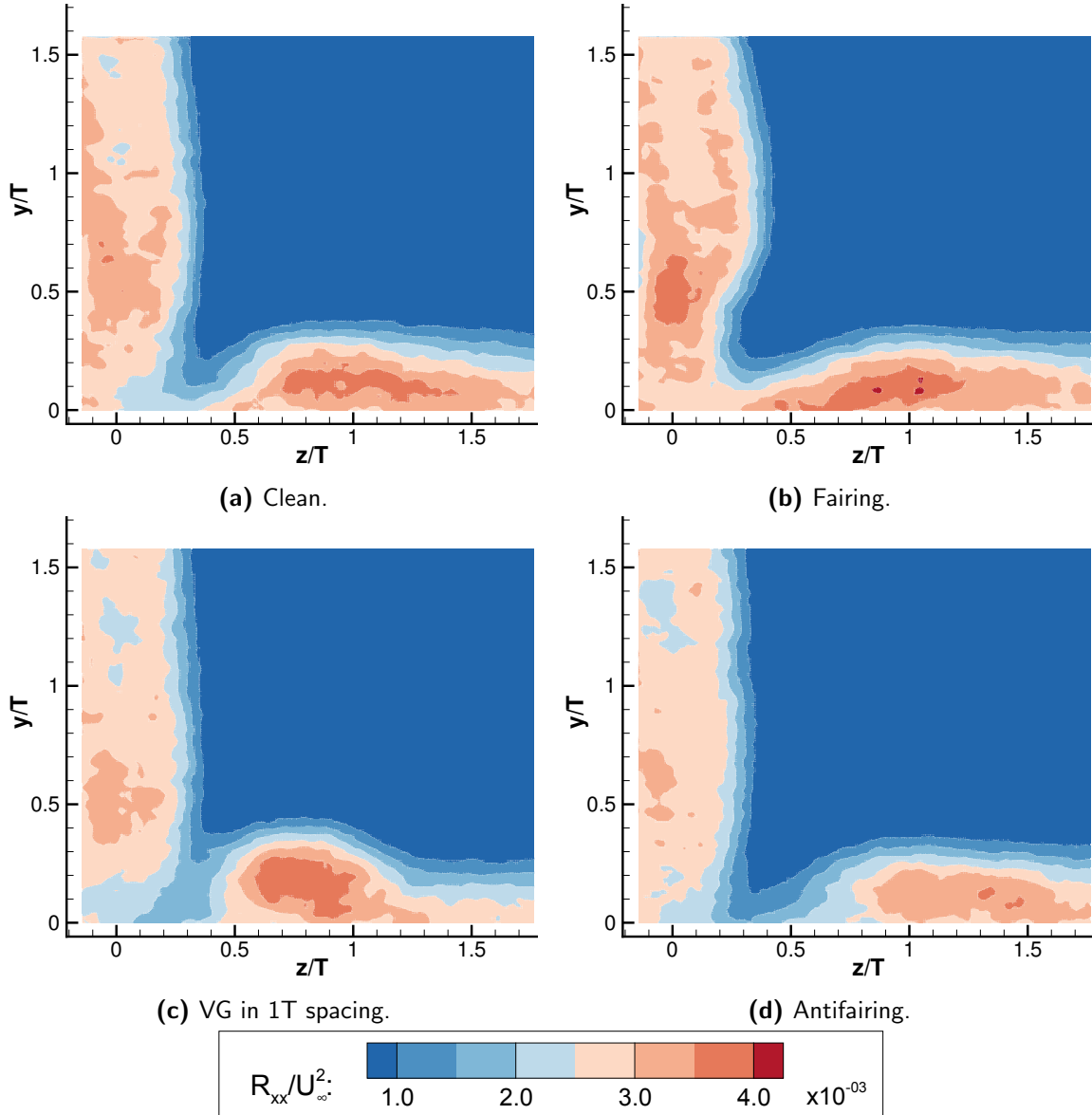
Figure 5.7: Streamwise Reynolds stress of the wake with different control devices

In terms of the streamwise Reynolds stress (R_{xx}), the fairing configuration has a comparable fluctuating level to the clean reference case. The VG case has a localized high turbulence region but reduces quickly in the normal to wing direction. The antifairing has the least streamwise turbulence. It appears that all configurations, excluding the VG one, have a more distributed turbulence along the boundary.

For the spanwise direction (R_{yy}), all configurations have a similar Reynolds stress values in

the boundary with the exception of the VG, which is the worse performer.

(a) Clean.

(b) Fairing.

(c) VG in 1T spacing.

(d) Antifairing.
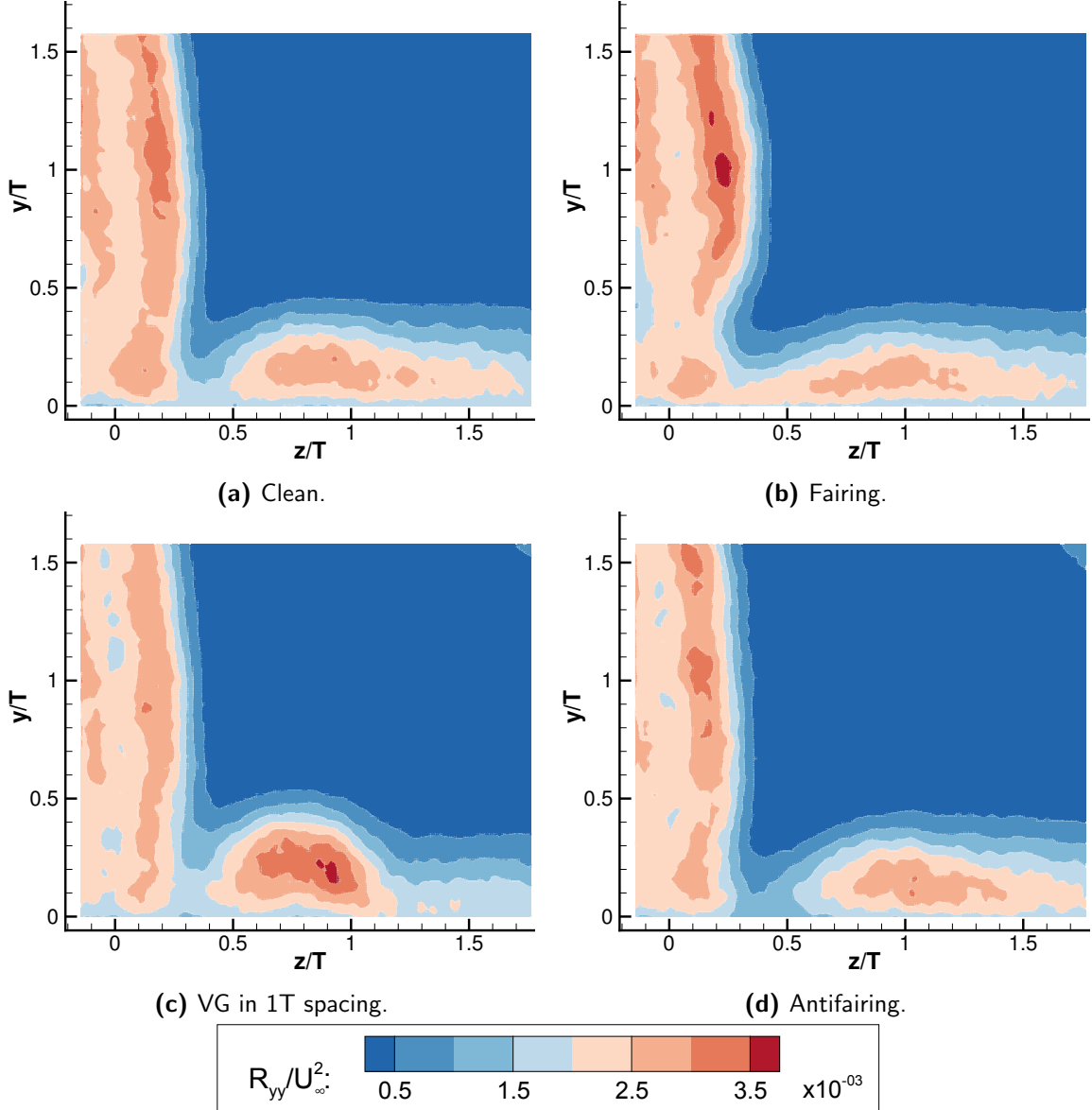
Figure 5.8: Spanwise Reynolds stress of the wake with different control devices

Lastly, the Reynolds stress in the normal direction (R_{zz}) is discussed. The clean and the fairing configurations are outperforming the other two in this direction. Again, the VG has high turbulence confined in a small region while the antifairing has it distributed along the plate. Besides, the turbulence level in the normal direction is almost double than the streamwise and spanwise direction for all configurations. This effect could be linked to the meandering effect, which is still recognized in the wake.

The peak Reynolds stress is summarized in table 5.2. In view of the results, it can be concluded that the VG configuration generates the most turbulence intensity levels downstream in all directions. The fairing is better than the antifairing in suppressing the fluctuations in the

(a) Clean.

(b) Fairing.

(c) VG in 1T spacing.
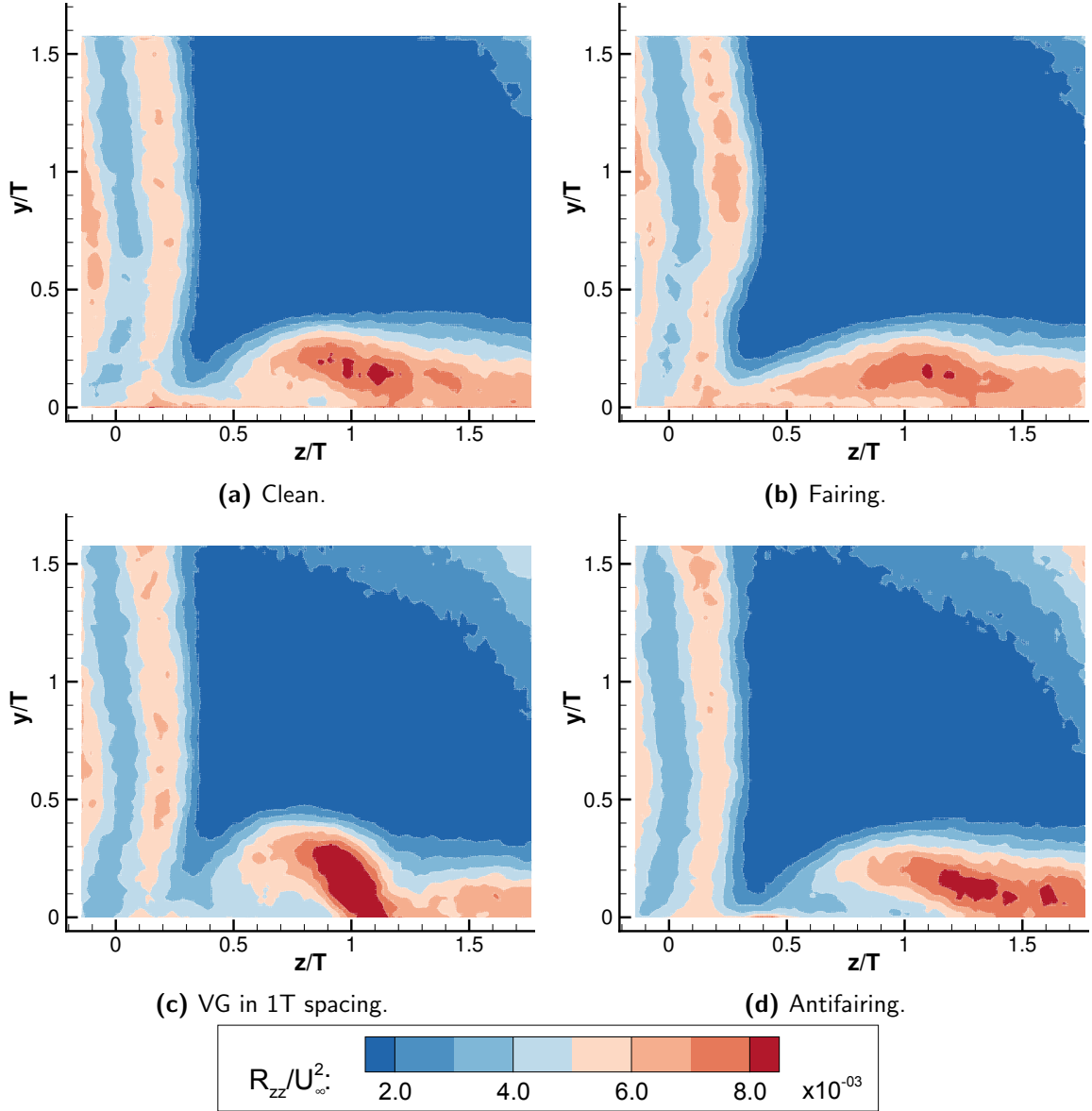
(d) Antifairing.

Figure 5.9: Normal Reynolds stress of the wake with different control devices

direction perpendicular to the freestream; while the antifairing works better in the streamwise direction.

Table 5.2: Peak Reynolds stress in the junction wake.

	R_{xx}/U_∞^2	R_{yy}/U_∞^2	R_{zz}/U_∞^2	
Clean	3.94	3.03	8.78	
Fairing	4.08	2.83	8.36	$\times 10^{-3}$
VG	3.97	3.63	10.26	
Antifairing	3.63	3.02	8.62	

5.3   Flow around wing-flat plate junction

Results of the tomographic measurement are presented in this section. Only those configurations which present less momentum deficit, the reference clean configuration, fairing, VG in 1T spacing and antifairing, presented in section A, are experimented. To begin with, results on the time averaged velocity of the flow are given, followed by the presentation of the HSV vortex structure. The closing of this section focuses on the circulation of the vortex and the turbulence level at different locations.

5.3.1   Time-averaged velocity field

To simplify the representation of the volumetric velocity field, multiple contour planes will be displayed.

Clean Configuration

Results of the clean configuration are displayed first to set the reference flow structures. The displayed planes are perpendicular to the freestream (x-planes) located at x/T = 0, 0.75, 1.5, 3 and 4 as shown in figure 5.10, which corresponds to the location of the leading edge, maximum thickness and others.
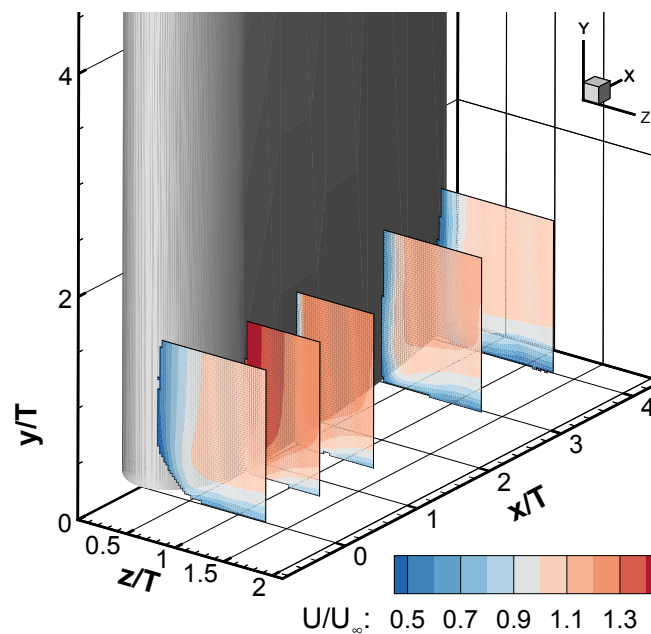
Figure 5.10: Illustration of the multiple planes.

At the plane of the leading edge, see figure 5.11a, the incoming freestream velocity has reduced its strength on the flat plate and also at the wing's leading edge, where the stagnation region is located. The velocity at the position of maximum thickness is shown in figure 5.11b. The

(a) x/T = 0.

(b) x/T = 0.75.

(c) x/T = 1.5.

(d) x/T = 3.

(e) x/T = 4.
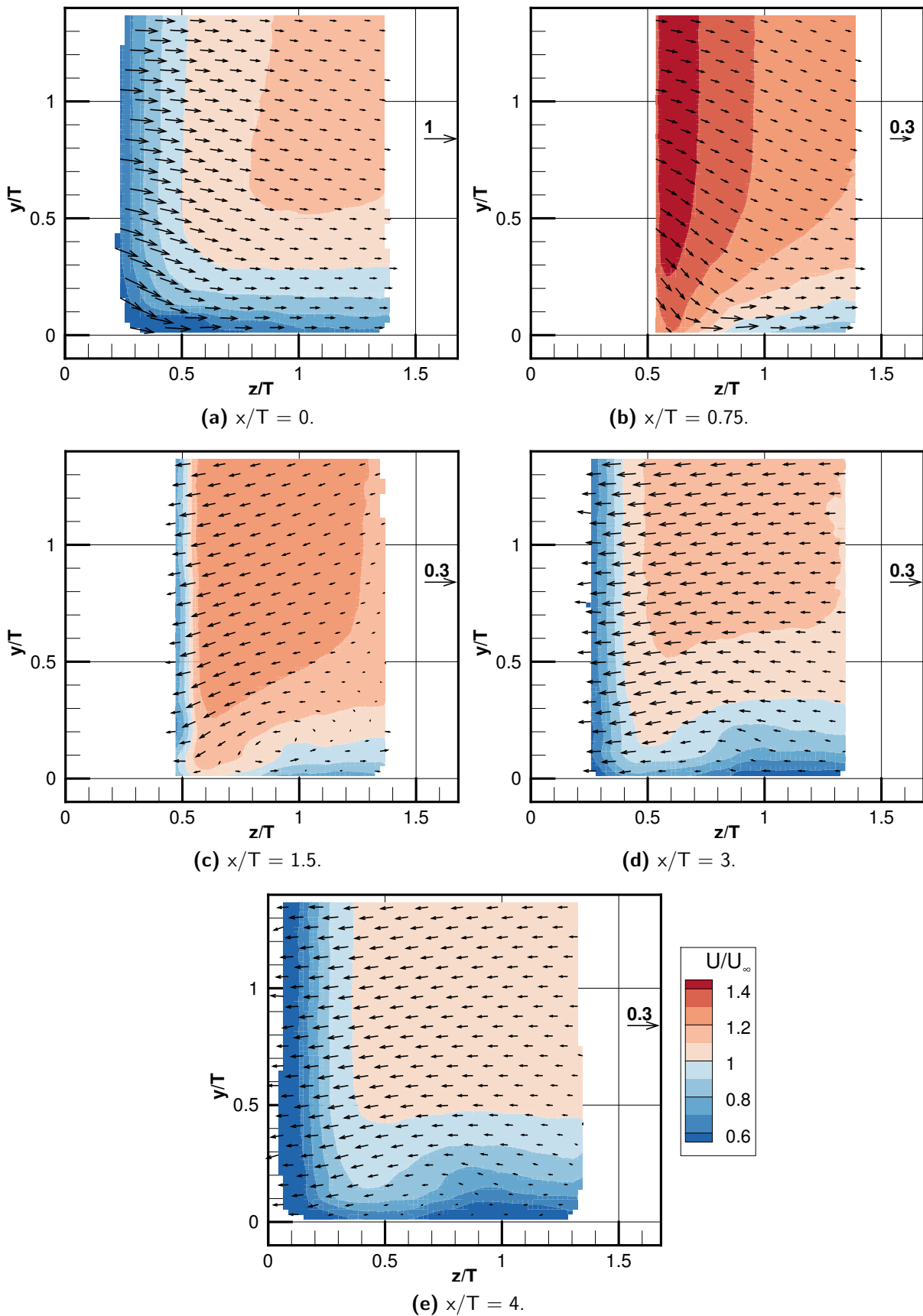
Figure 5.11: Averaged velocity field across multiple planes.

flow surrounding the wing accelerates and so does the flow at the wing-flat plate juncture.

On the plate boundary further away from the wing, the velocity is maintained relatively low as the effect of the wing's curvature is reduced with distance. After the maximum thickness point, at x/T = 1.5, the flow decelerates again as the thickness of the airfoil is reduced. The tapering also causes the velocity component normal to the wing to have a negative sign. A vortex is visible at this plane location. The vortex is drawing high momentum flow towards the juncture, and the same time pushing the boundary flow outward. Because of the rotation, some of the boundary flow close to the vortex is also lifted up. Moving towards the trailing edge, the contours of the streamwise velocity are similar to the one observed at the previous location such as x/T = 1.5. Nevertheless, the velocity magnitude is continually decreasing the closer it is to the trailing edge. Additionally, the prints of the vortex also become less noticeable downstream.
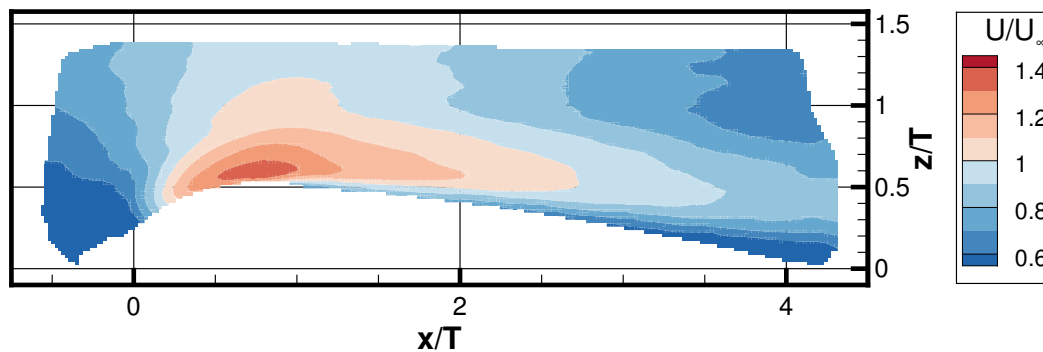
(a) Contour of streamwise velocity at y/T = 0.1
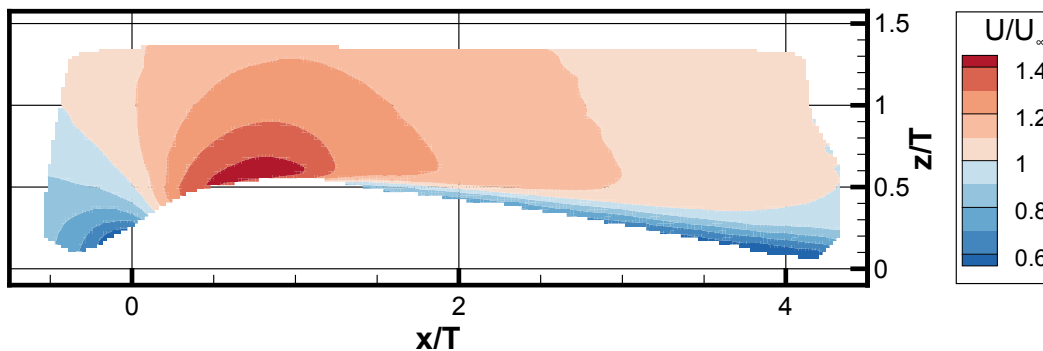
(b) Contour of streamwise velocity at y/T = 0.5

Figure 5.12: Streamwise velocity of the clean configuration at different spanwise planes.

Viewed from the top of the junction, see figure 5.12, at a height of y/T = 0.1, a stream of stronger streamwise velocity can be appreciated close to the wing. Such stream is the result of the vortex which brings the high momentum from the freestream to the inner region. More details is explained in section 5.3.2. At the outer region, the lower momentum can be associated with the combined effect of the plate boundary layer and the transported flow by the HSV. This features cease to exist for a height above y/T = 0.5, where the streamwise velocity field assimilates to a 2D isolated airfoil.

Comparison with other configurations

The velocity fields of other configurations are shown in this section. Results on the velocity field are focused at planes x/T = 0, 1.5 and 4.

(a) Fairing.

(b) VG.

(c) Antifairing.
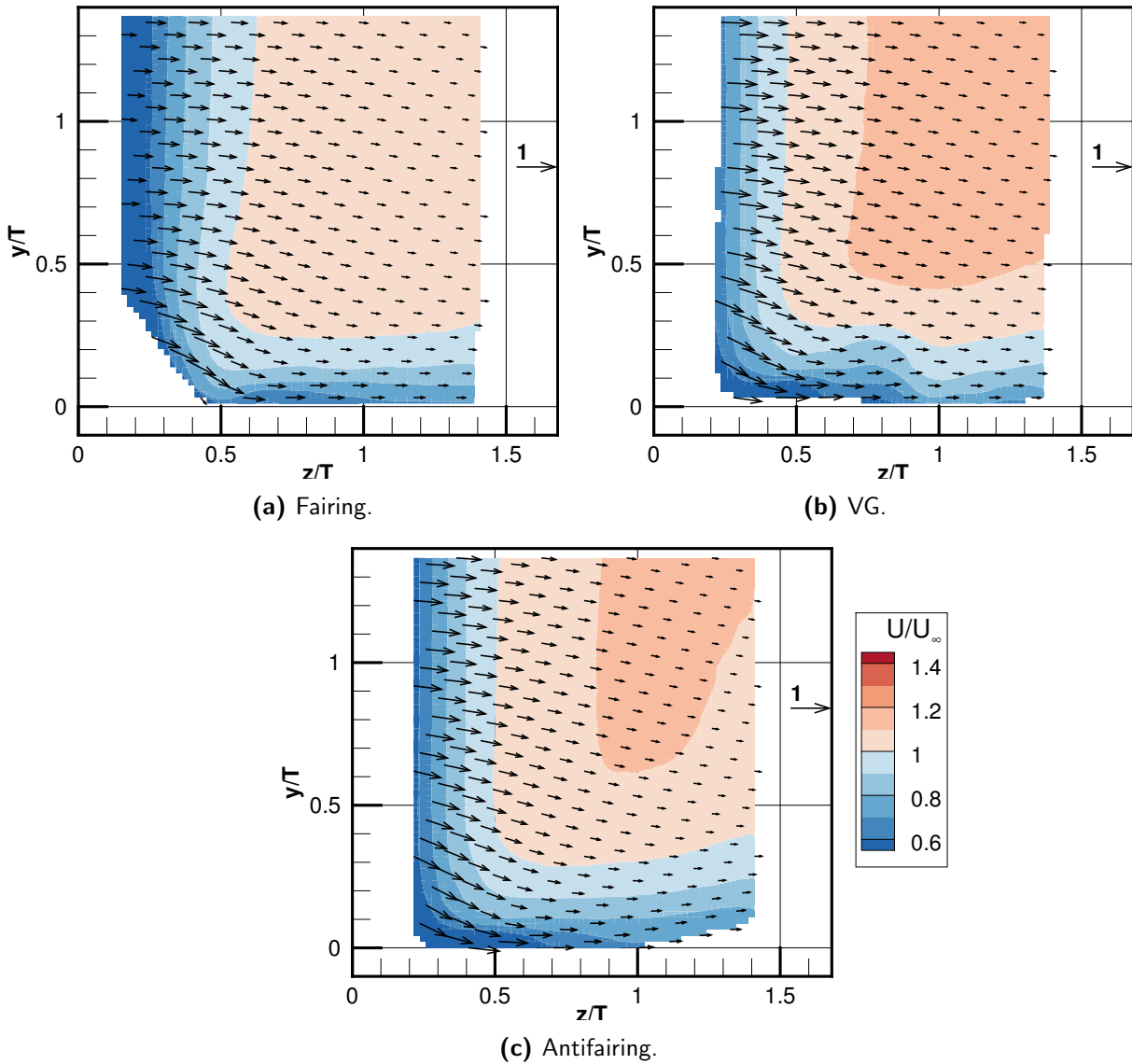
Figure 5.13: Streamwise velocity of different configuration at x/T = 0.

At the leading edge plane, the streamwise velocity measured at the outer region (away from the flat plate) is lower for the fairing configuration than all the others, see figure 5.13. The velocity in the normal direction is also slightly lower at the leading edge, possibly due to the gradual deflection of the leading edge fairing. Apart from these observations, the fairing has a similar contour to the clean configuration. The antifairing also has a similar streamwise velocity contour, but due to dented surface, the flow close to the plate surface is flowing upward lightly. Most changes are observed for the VG configuration. Although the vector

field does not give an indication of a clear vortex, a contour area of low velocity is found at the boundary, which looks alike to the field found at the wake.

(a) Fairing.

(b) VG.

(c) Antifairing.
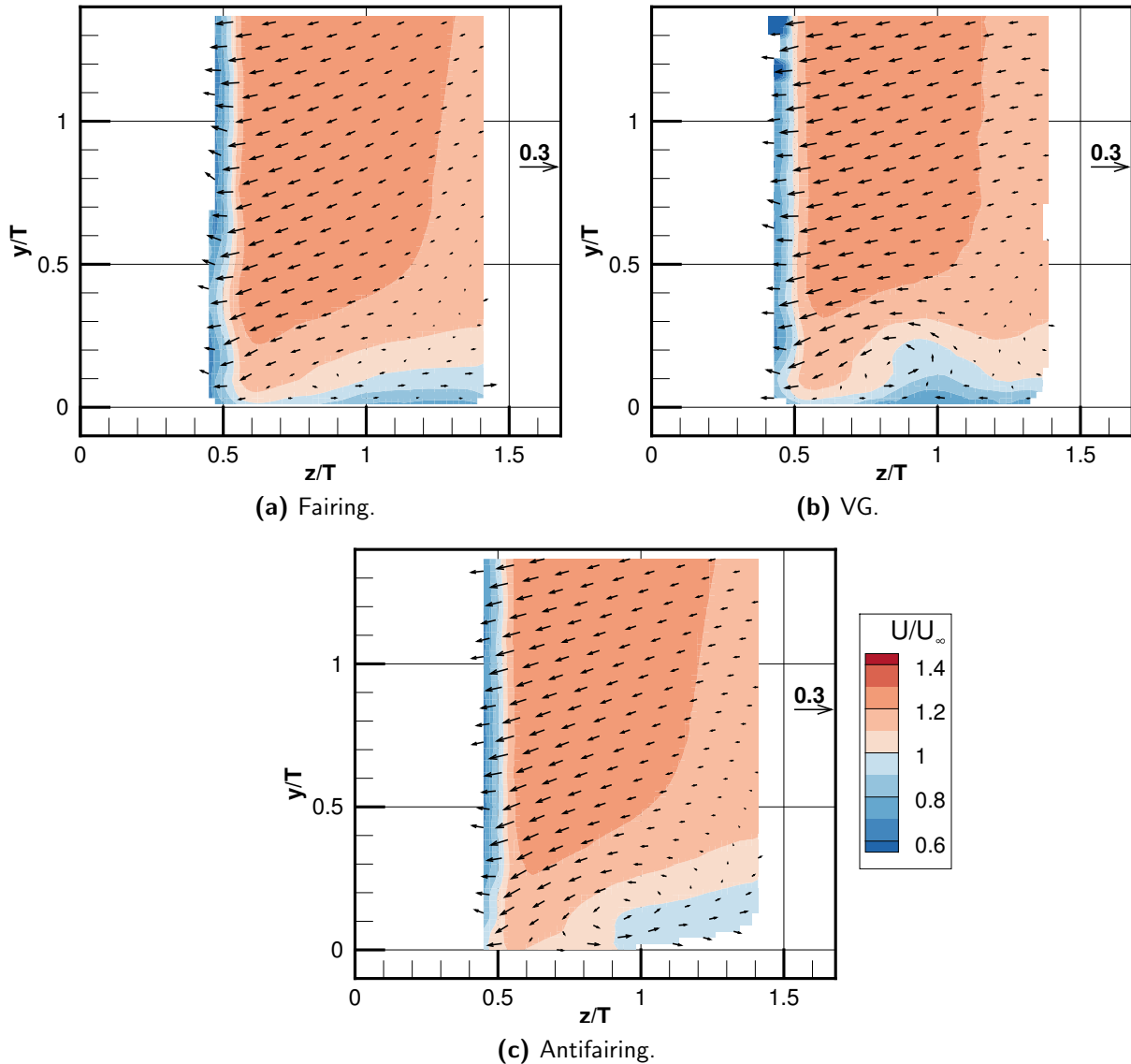
Figure 5.14: Streamwise velocity of different configuration at x/T = 1.5.

The next location to be discussed is at x/T = 1.5. The vector fields in this plane show a well defined vortex across all the configurations. It can be deduced that the vortex from the fairing configuration has a weak rotational intensity, while both VG and the antifairing have a stronger one. As the fairing has a weak vortex, the induced downwash is more gradual along the normal to wing direction compared with the latter configurations. At z/T = 1.2 of the VG case, the in-plane velocities, shown as vector field, indicate the flow is going inward on the boundary, which is the opposite direction than in other configurations. This aspect is the result of the vortex from the control device, which has reversed rotating direction compared with the main HSV.

At the trailing edge region, see figure 5.15, the contour plots have a comparable appearance to the previous plane with a reduced intensity. Once again, the boundary layer of the fairing configuration stands out from the others, as its characteristics look like a recovered boundary layer with a faintly wake from the vortex. The in-plane velocities do not indicate a clear presence of the HSV.

(a) Fairing.

(b) VG.

(c) Antifairing.
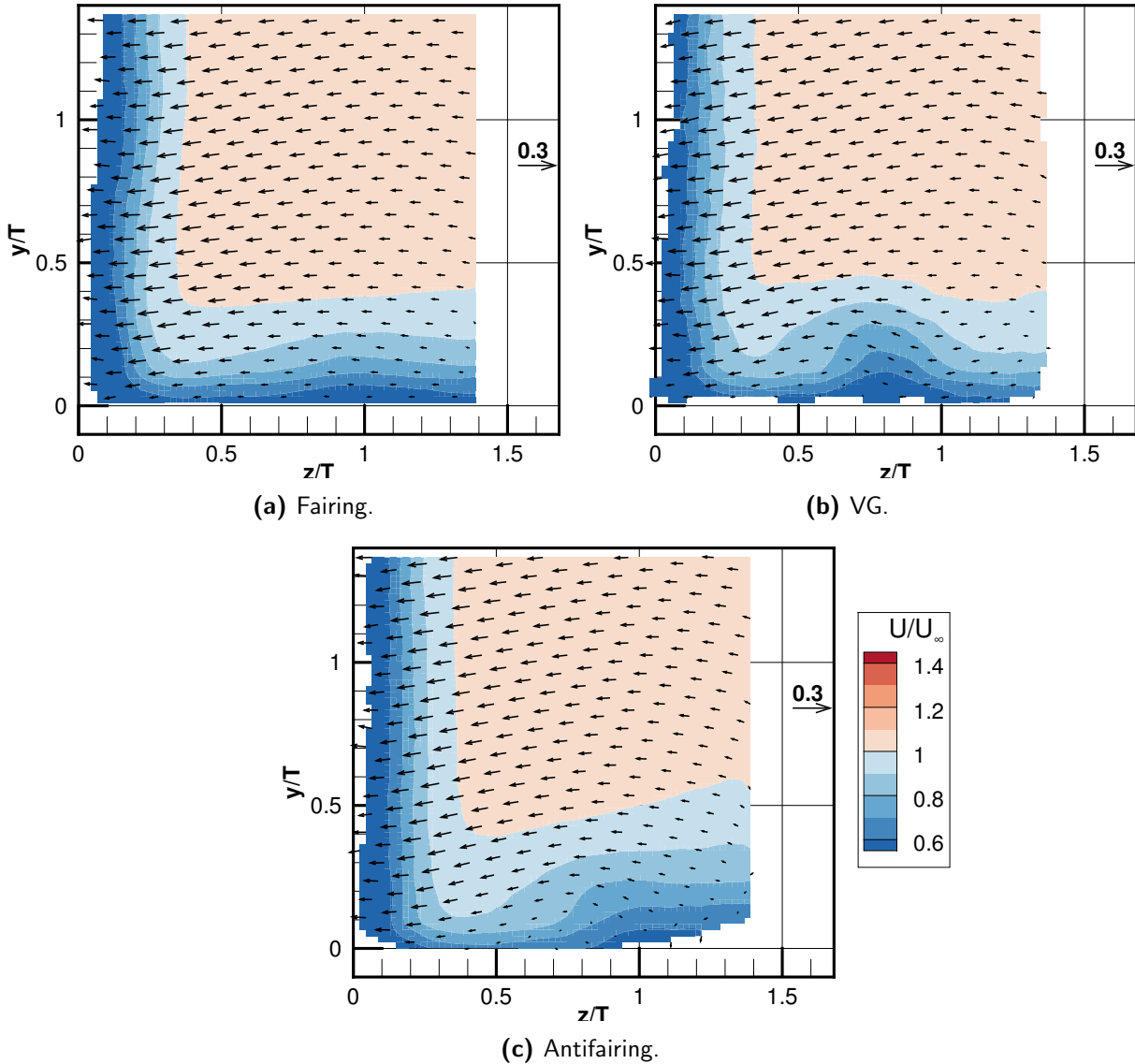
Figure 5.15: Streamwise velocity of different configuration at $x/T = 4$.

Viewed from the top at $y/T = 0.1$, see figure 5.16, the fairing configuration presents a slower velocityof about $0.1U/U_\infty$ times less than the other configurations at the point of maximum thickness. The antifairing does not have major differences compared to the clean configuration. In regards to the VG configuration, the velocity field appears to be divided into two sections normal to the wing. As the division is located around $z/T = 1$, the two regions are mainly separated by the pair of vortices from the VG and HSV. This flow pattern is resulted

from the pair of common-up-flow vortices that draw high velocity fluid from the freestream towards the boundary, leaving a region of low velocity in between them. This explanation is represented in figure 5.24.

(a) Fairing.

(b) VG.

(c) Antifairing.
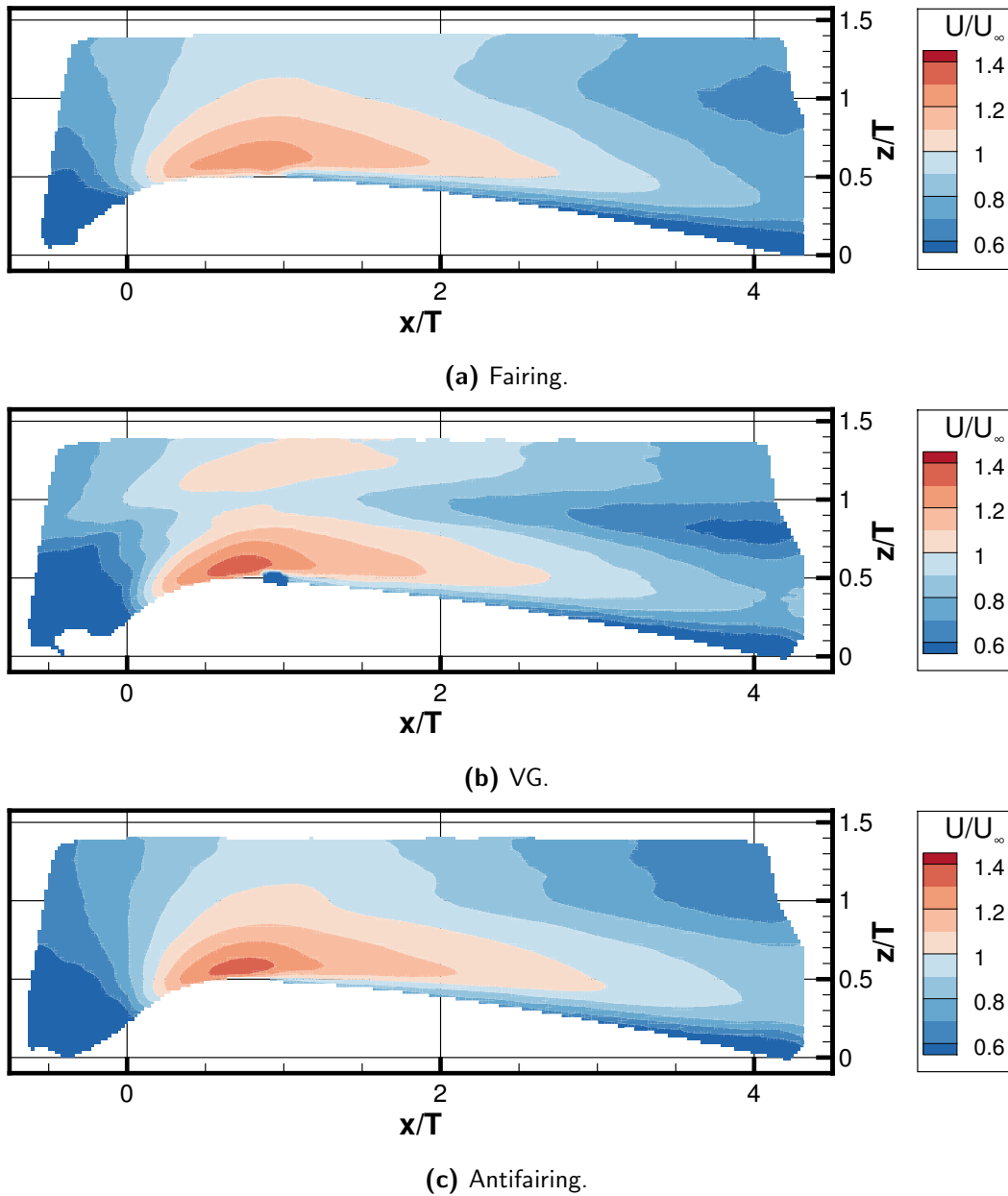
Figure 5.16: Streamwise velocity of different configuration at $y/T = 0.1$.

5.3.2   Topology of vortical structure

Clean Configuration

The velocity field of the junction flow and some features of the generated HSV have been introduced in section 5.3.1. However, the location of this vortex is still unclear. In order to find out its location, contour of the streamwise vorticity is plotted. To complement the identification of the vortex location, the Q-criterion is applied and an isosurface with a proper value is displayed.

Contours of the streamwise vorticity at selected planes normal to the streamwise flow are shown in figure 5.18. Note the colorbar level changes depending on the location in order to appreciate the decreasing value. At the leading edge plane, a clear area with negative vorticity is found at the junction, which corresponds to the main HSV. A positive vorticity region is created by the HSV at the boundary, which can be appreciated at planes x/T = 0.75 and 1.5. The positive vorticity indicates the presence of a shear layer, caused by the induced velocity from the HSV. Besides, the peak vorticity value of the main HSV vortex decreases downstream. Close to the trailing edge, the vortex does not have a coherent structure anymore, which suggests the vortex has broken down into smaller structures.
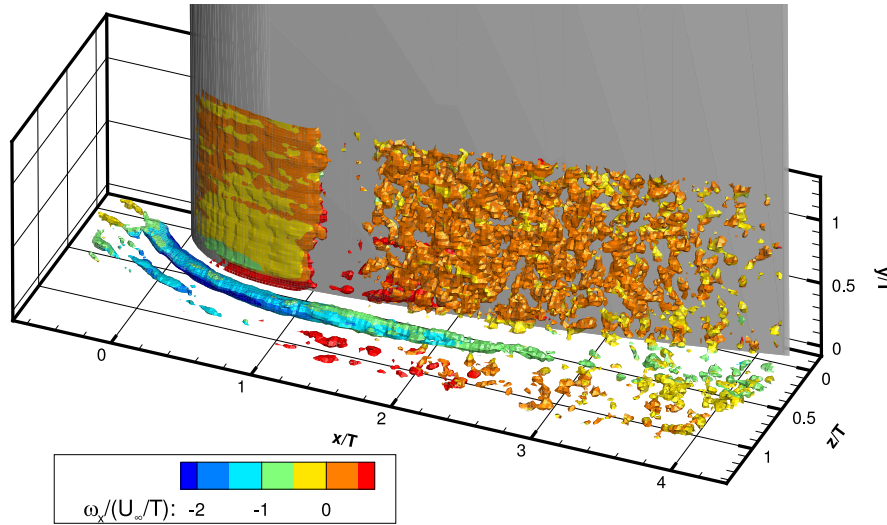
Figure 5.17: Isosurface of Q = 0.2 flooded with streamwise vorticity.

The isosurface of $\frac{Q}{(U_\infty/T)^2} = 0.2$, flooded with streamwise vorticity is displayed in figure 5.17. Note that an isosurface is also present on the surface of the wing. Nevertheless, such surface does not indicate the presence of vortices but is originated due to curvature effect, hence, the isosurface of Q on the wing is discarded from the discussion. The HSV can be seen wrapped around the wing surface. Close to the leading edge region, a small structure parallel to the main vortex is present. This structure is a secondary HSV vortex, discussed in the literature review (section 1.1.1), which is isolated from the main vortex by the line of low shear. From x/T = 2, the size of the vortex tube becomes thinner and it ceases to exist after x/T = 3. Nevertheless, a population of small structures with the same Q value is clustered downstream. Such observation confirms the breakdown of the main HSV.

(a) x/T = 0.

(b) x/T = 0.75.

(c) x/T = 1.5.

(d) x/T = 3.

(e) x/T = 4.
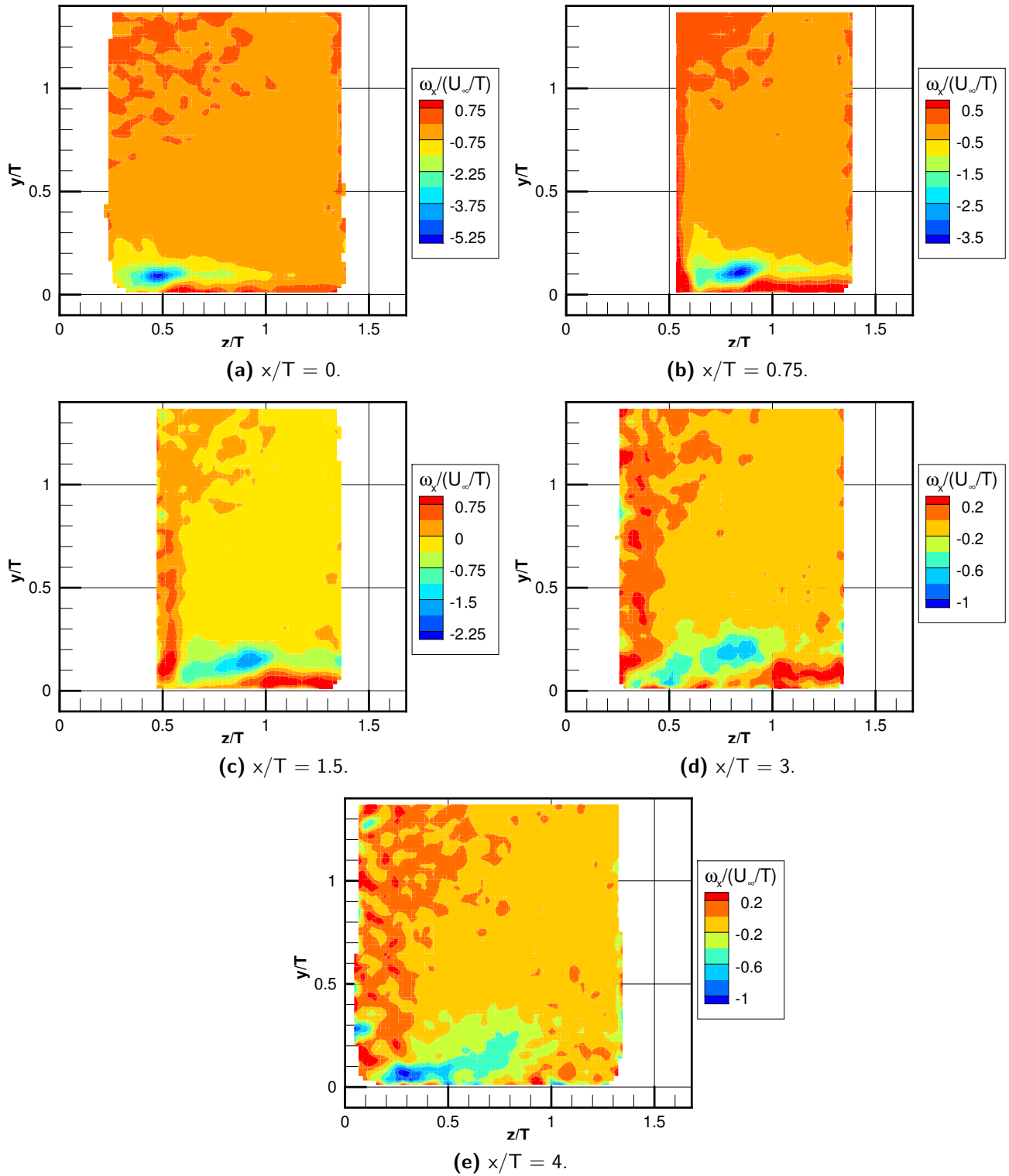
Figure 5.18: Vorticity field across multiple planes.

Comparison with other configurations

The results of the vorticity field are shown in figures 5.19-5.21. The displayed planes are the same as the ones presented in the averaged velocity, x/T = 0, 1.5 and 4.

(a) Fairing.

(b) VG.

(c) Antifairing.
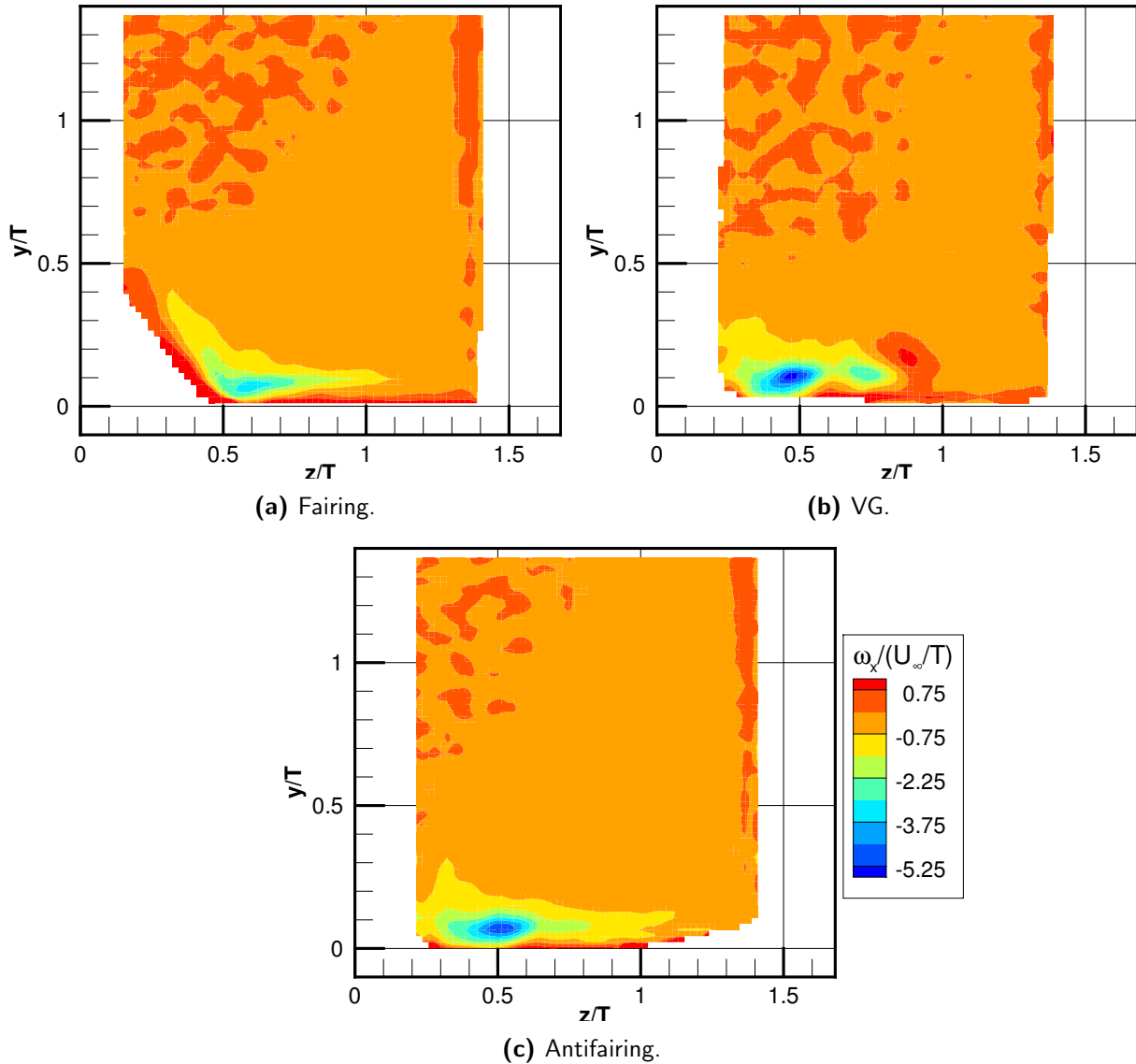
Figure 5.19: Streamwise vorticity of different configuration at x/T = 0.

Starting the discussion on the results from the leading edge plane, the fairing configuration presents the least vorticity intensity. Besides, the countour of the vorticity is stretched along the fairing and the flat plate. The vorticity contour and intensity of the antifairing configuration assemble to the reference case. The vorticity field from the VG configuration displays three locations where vortices could take place: two corotating negative vortices close to the wing's leading edge and a positive one at z/T = 0.9. The less intense negative vortex could be a secondary HSV whose strength is intensified by the action of the third positive vortex from the VG.

(a) Fairing.

(b) VG.

(c) Antifairing.
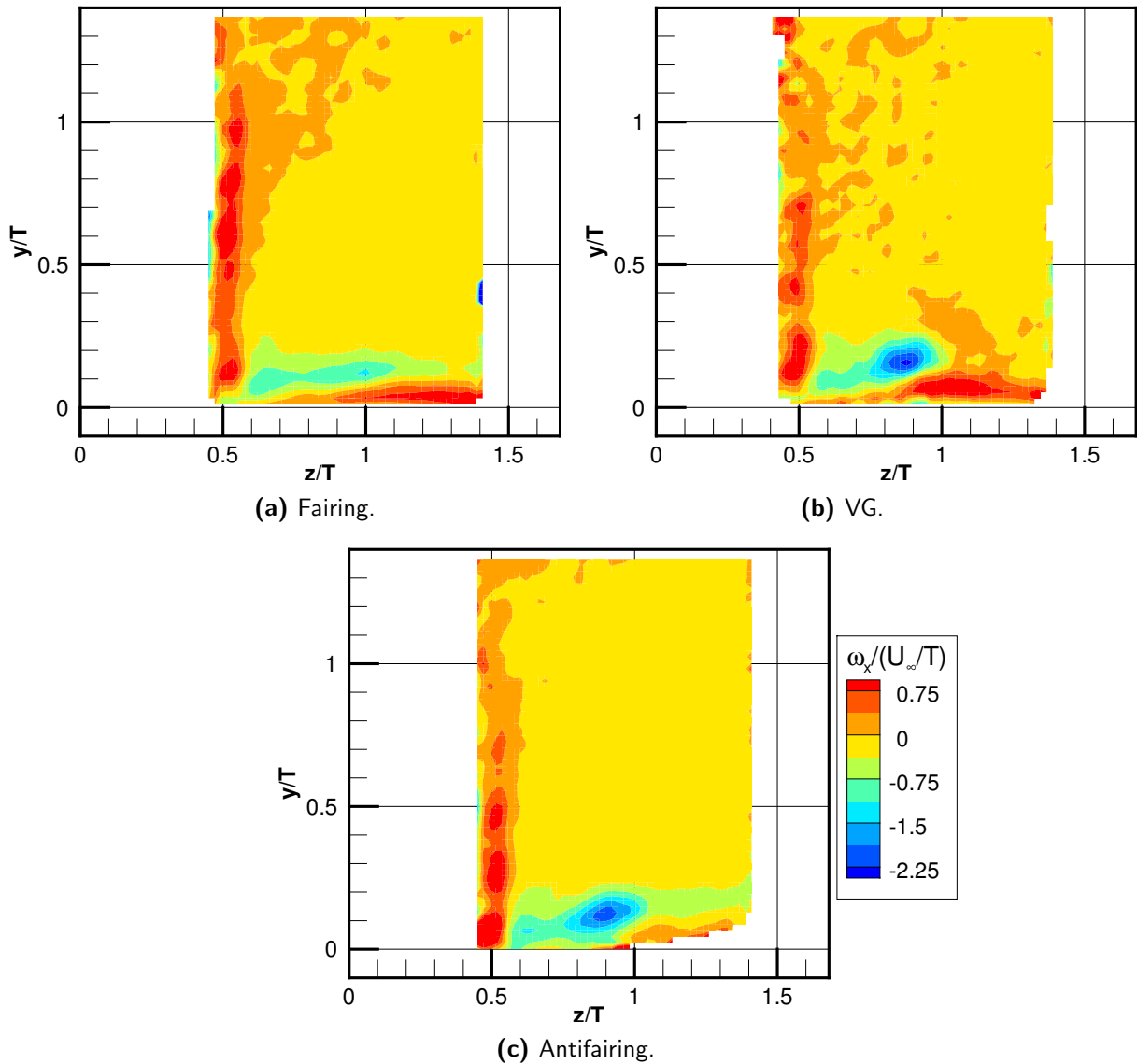
Figure 5.20: Streamwise vorticity of different configuration at $x/T = 1.5$.

Following by the plane at $x/T = 1.5$, note that the vorticity level scale is adjusted to better represent the fields, as the minimum value now is halved compared to the one at the leading edge. The fairing configuration is still the one which has the smallest value in vorticity magnitude, but also more spread along the z direction. Both the antifairing and VG configurations have a more localized high vorticity region. A common feature, with the exception of the antifairing, is that a positive vorticity, which has been discussed to be a shear layer, is created in the normal direction from the main HSV, at about $z/T = 1.2$. The reason for the antifairing to have a less intense shear layer could due to the slower velocity at that region as the flow is expanded inside the dent. As a result, the flow is steadier. However, it could also be the case that the flow in the sloped region is not well captured due to limited optical access.

(a) Fairing.

(b) VG.

(c) Antifairing.
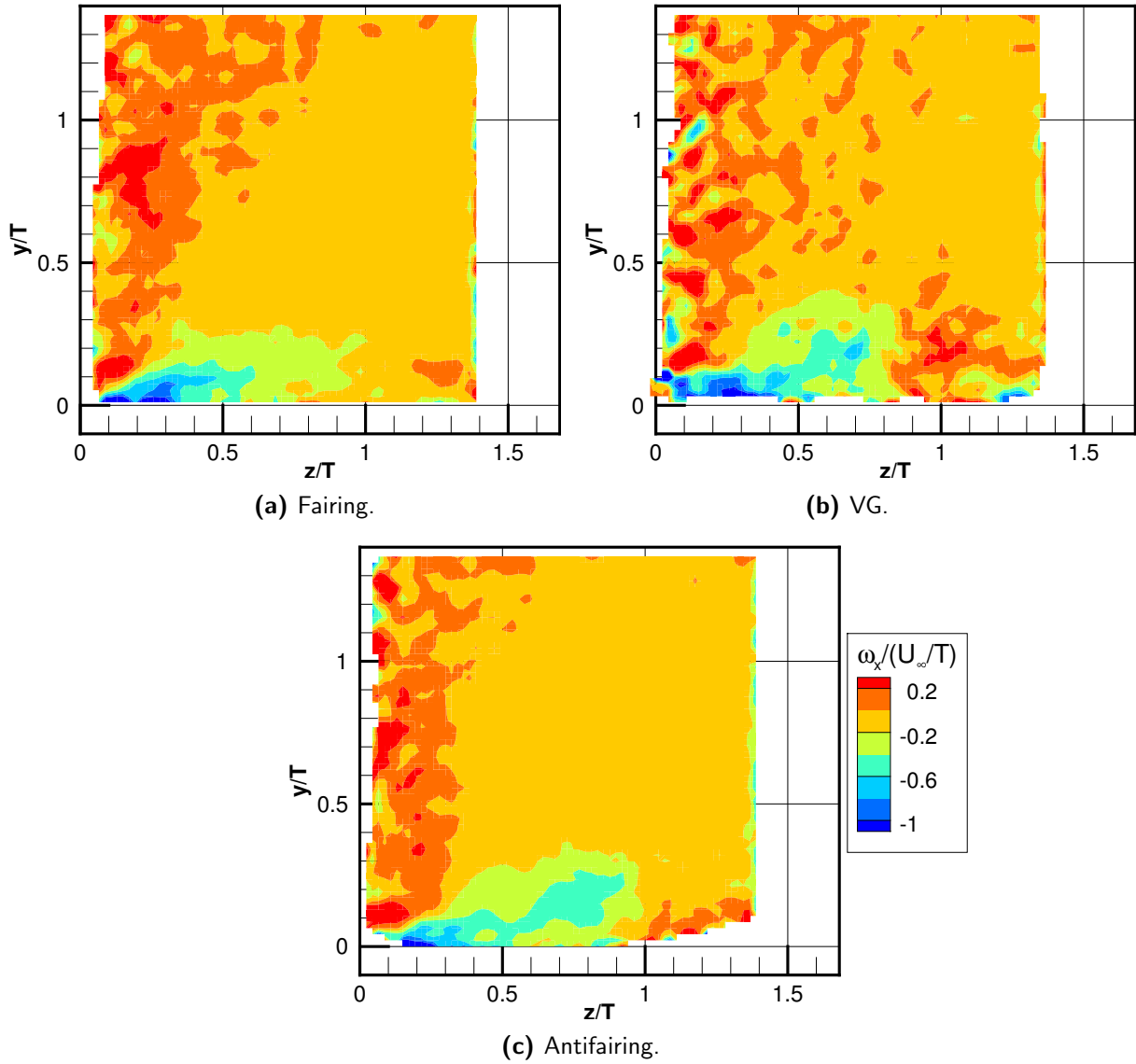
Figure 5.21: Streamwise vorticity of different configuration at x/T = 4.

The vorticity intensity at the trailing edge, shown in figure 5.21a, is reduced considerable across all configurations. Once again, the contour level is adjusted to appreciate the small differences. The fields appear to be noisier especially for the VG case. This effect is due to the scale of the color level used, and the higher fluctuation associated with the vortex breakdown. For the VG case, fewer effective samples are used to compute it, thus, the vorticity field could be not converged in this high fluctuating region. Regardless the noise, it can be noted that a negative vorticity is concentrated close to the trailing edge juncture in all configurations, fact that gives the downwash flow pattern observed in the wake.

Isosurfaces of Q criterion with value $\frac{Q}{(U_\infty/T)^2} = 0.2$, flooded with vorticity, are shown in
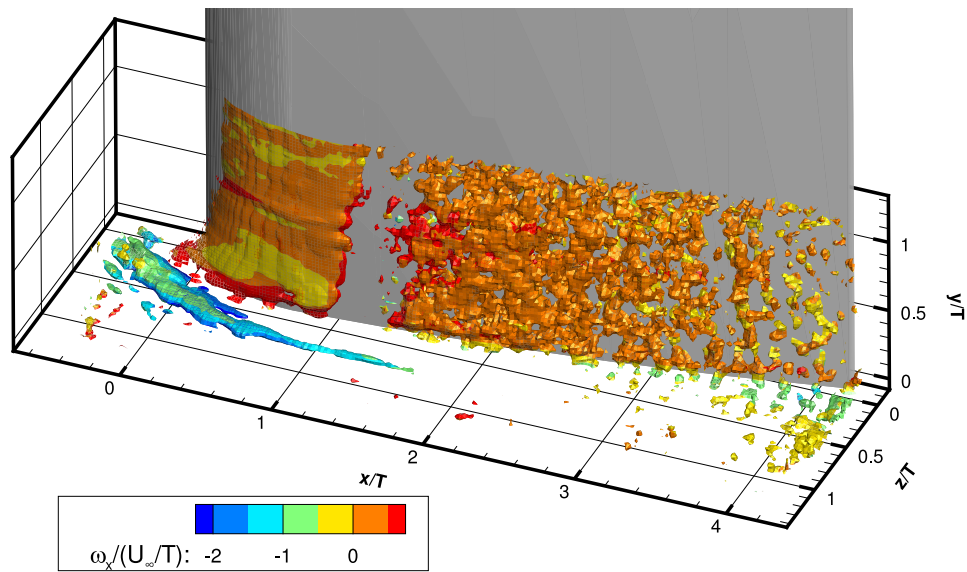
(a) Fairing.
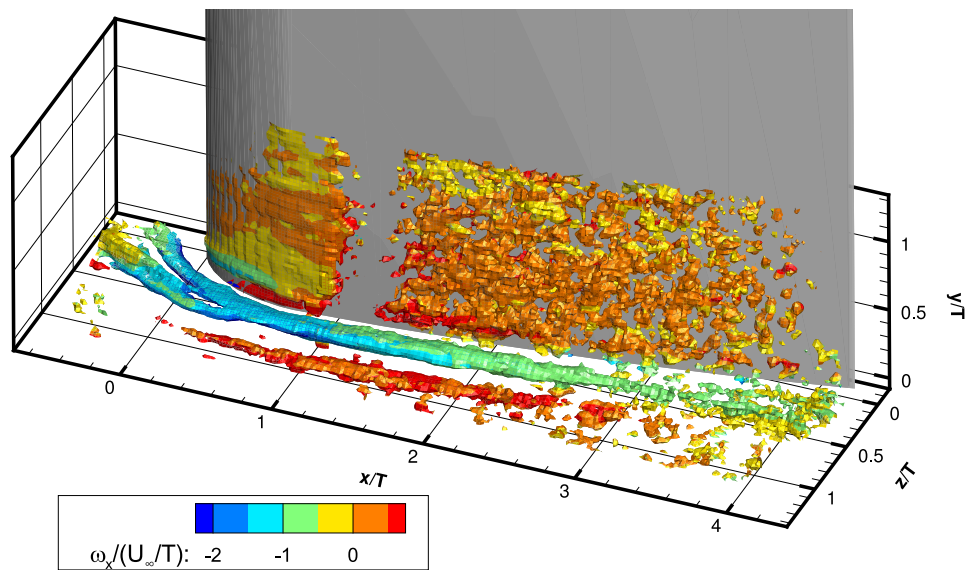
(b) VG.

Figure 5.22: Isosurface of normalised Q = 0.2 flooded with streamwise vorticity for different configurations.

figure 5.22. The HSV in the fairing configuration breaks downs in a shorter distance, before reaching x/T = 2, than other configurations. For this reason, the vorticity field intensity reduces quickly downstream. For the VG case, the presence of the secondary vortex is more pronounced than in the clean configuration, mainly due to the interference from the positive vortex of the VG device. The secondary vortex merges with the main HSV around the maximum thickness region. The combined HSV is slightly larger in size than the reference and holds the coherent structure longer before breaking down. However, the structures created after the break down appear to be relatively large as well. Parallel to the main HSV, the
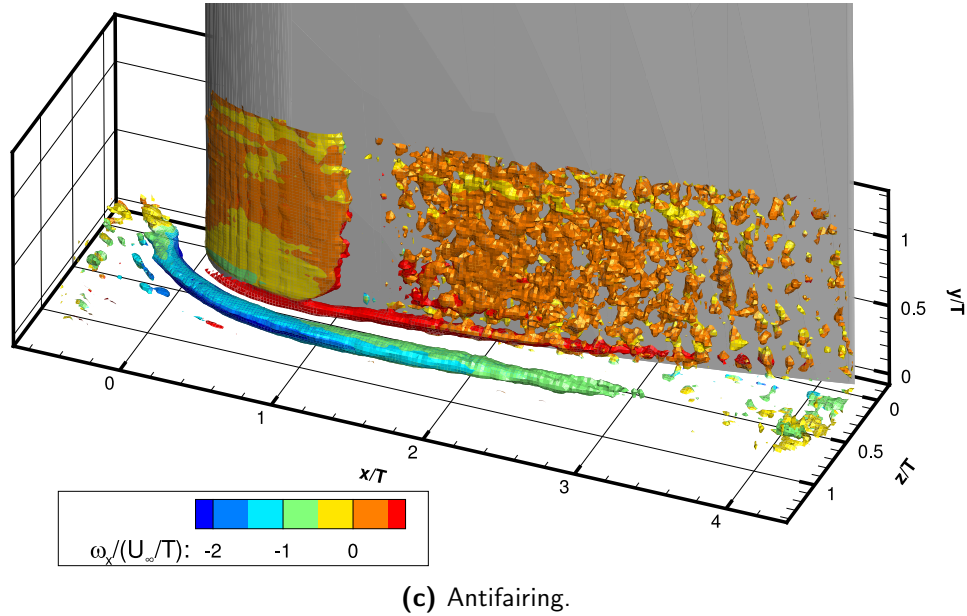
(c) Antifairing.

Figure 5.22: Isosurface of normalised Q = 0.2 flooded with streamwise vorticity for different configurations. (cont.)

vortex generated by the control device with positive rotation can also be observed. The structure of the positive vortex is less coherent and is also diffused at a similar point to the main HSV. Finally, the antifairing has a HSV which holds its circular shape similar to the clean configuration one. In terms of size, it is thicker in the spanwise direction, but this does not delay the point of HSV breakdown.
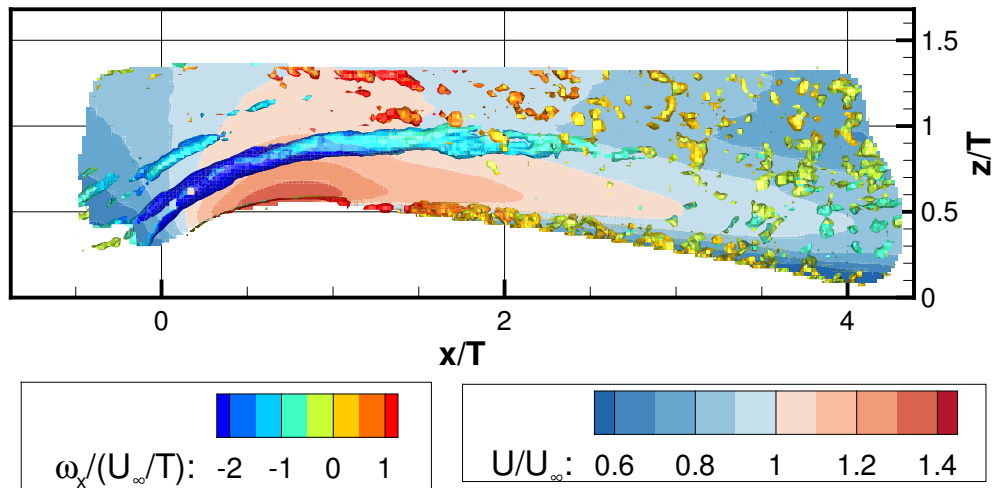
Figure 5.23: Superposition of streamwise velocity contour at y/T = 0.15 and isosurface of $\frac{Q}{(U_\infty/T)^2}$ = 0.2 flooded with streamwise vorticity of the clean configuration.

It has been shown in section 5.3.1 that the contour of the streamwise velocity has a high velocity stream feature when viewed from above. Such stream is the result of momentum transfer from the freestream to the boundary by the action of the HSV. It is shown clearly

in figure 5.23 that the vortex tube separates the high and low velocity regions, while the streamwise velocity is lower in the same position of the vortex.

A similar image is displayed for the VG configurations to complement the explanation. In this case, it can be noted that the outer high momentum region is accompanied by the positive vorticity. This evidence confirms the pair of vortices are transferring momentum from the freestream to the boundary. Besides, it is observed also that the secondary vortex leaves a trace of lower streamwise velocity at its location close to the leading edge.
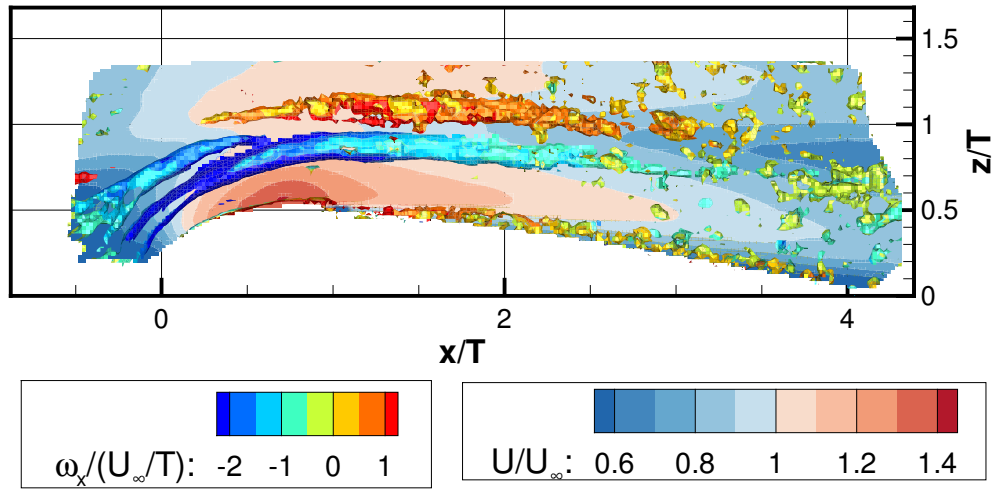
Figure 5.24: Superposition of streamwise velocity contour at $y/T = 0.15$ and isosurface of $\frac{Q}{(U_\infty/T)^2} = 0.2$ flooded with streamwise vorticity of the VG configuration.

5.3.3 Circulation

The flow kinematics and the vortical structures have been shown in sections 5.3.1 and 5.3.2. In order to quantify the HSV strength, circulation is used in addition to the vorticity, as it takes into account the size of the vortex as well.

The approach of the circulation calculation is explained in section 4.7.4. First, the location of the vortex core has to be determined. In order to obtain such information, the vortex core is considered to be at the peak vorticity value within the vortex tube. The circulation value is calculated on all the planes normal to the streamwise direction, as the HSV is composed mainly by streamwise vorticity.

The location of the HSV is plotted in figure 5.25. Note the curves start to oscillate for $x/T > 1.5$, as the vortex begins the transition to the breakdown process. This effect can also be observed in the Q-criterion figures. Additionally, the measured peak vorticity is shown in figure 5.26. As it has been discussed in the previous sections, the fairing is the configuration with least vorticity. The HSV from the antifairing configuration begins with a value similar to the one in the clean configuration, but is maintained higher in absolute value through the streamwise direction. The VG also has a comparable vorticity magnitude close to the leading
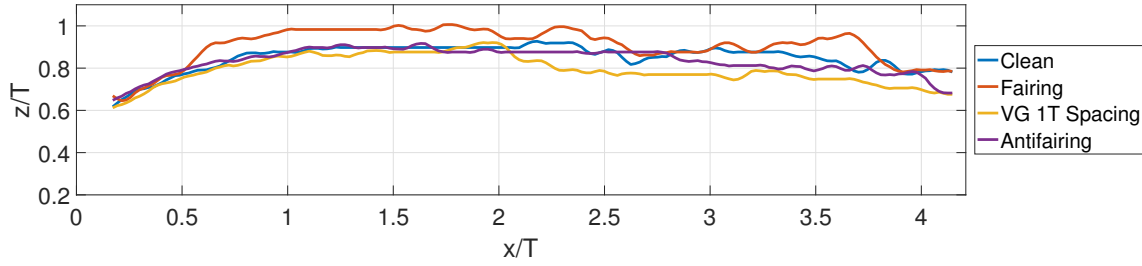
Figure 5.25: Position of the peak x-vorticity.

edge region. However, it has larger value downstream. At the trailing edge, the vorticity values of the latter three configurations converge again.
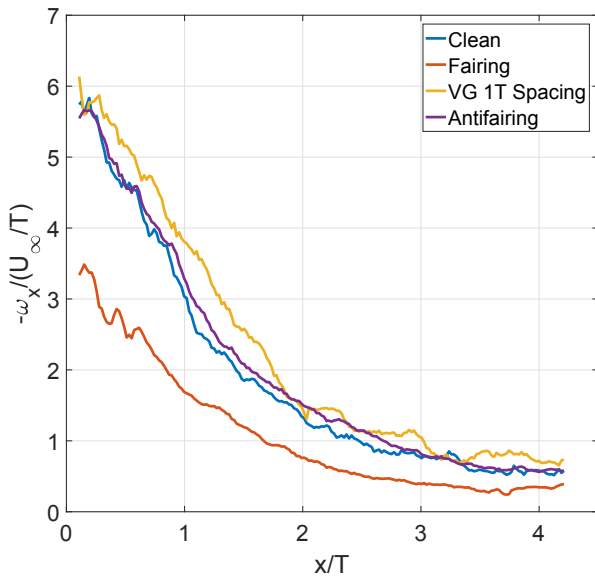
Figure 5.26: Peak streamwise vorticity value measured across the x-direction.
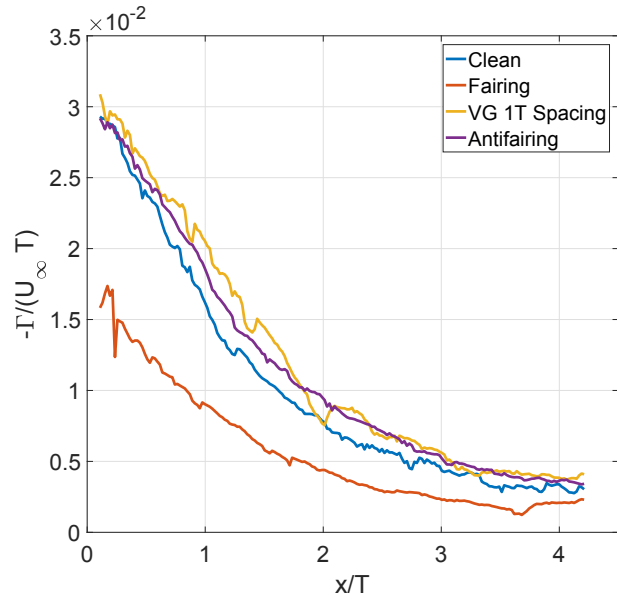
Figure 5.27: Circulation value calculated on a radius of 3mm around the peak vorticity location.

The results of the circulation are shown in figure 5.27. The fairing configuration exhibit the least intensity. The VG and the antifairing configurations are the ones to have higher circulation. Since the HSV associated to the antifairing is larger in size, its circulation is close to the VG case regardless the lower vorticity value.

From these observations, it can be concluded that the VG and the antifairing configurations produce a vortex stronger than the clean wing-flat plate junction. A maximum difference of about 42% and 13% in the peak vorticity is observed at x/T =1.1. The fairing configuration is the most efficient in damping the HSV with up to 40% less peak vorticity at the vortex head. In terms of circulation, the fairing still holds the configuration with least value across the x direction with an average of 45% less than the reference. For the VG and the antifairing, an average of higher circulation value, 21% and 17% respectively, are calculated.

5.3.4 Turbulence level

The last quantity to discuss is the turbulence level. The results from the reference configuration are displayed in this section together with other configurations in order to facilitate the comparison. The normal components of the Reynolds stress are examined on two planes, x/T = 1.5 and x/T = 4.
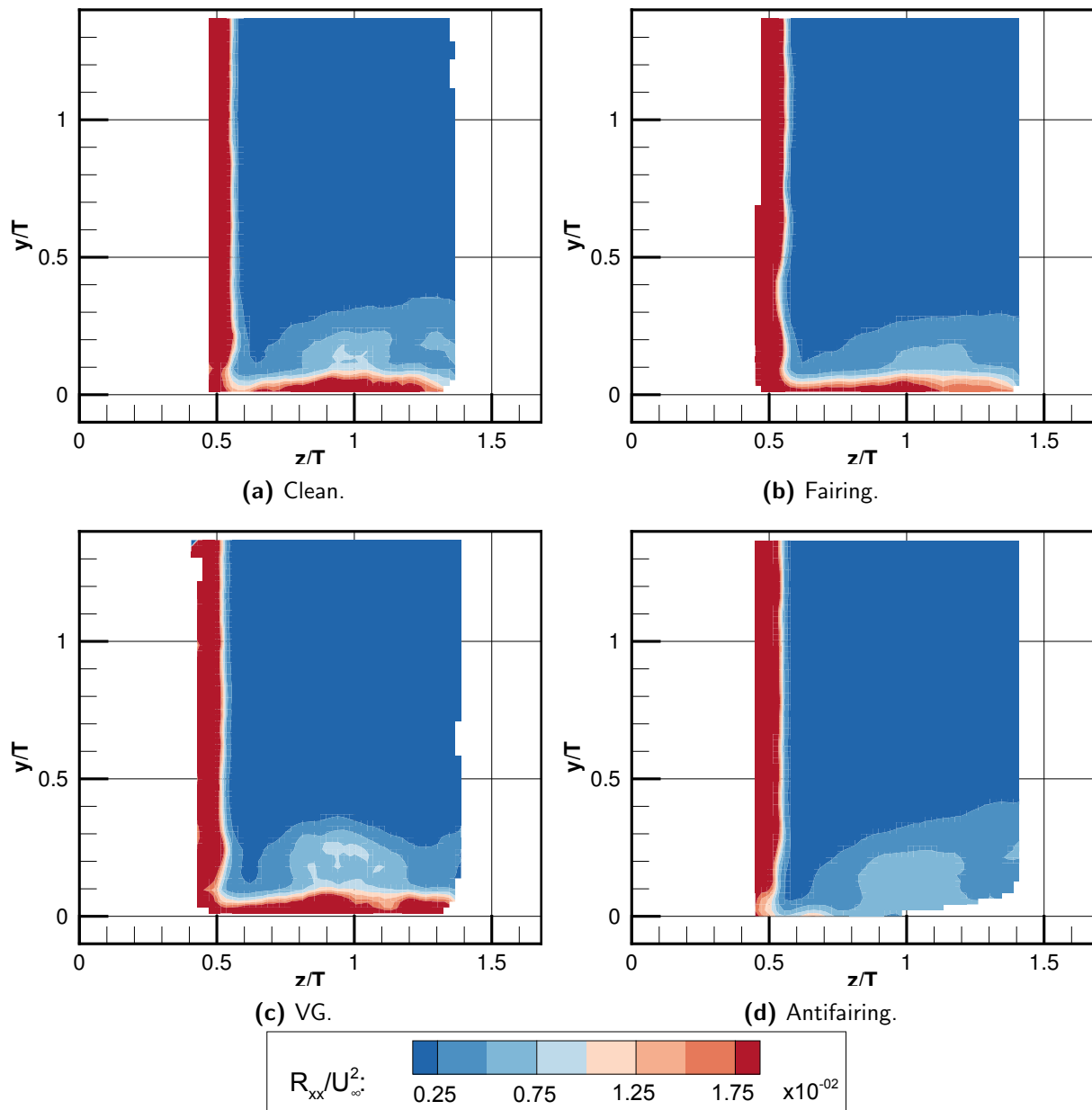
Figure 5.28: Streamwise Reynolds stress at x/T = 1.5.

The streamwise component of the Reynolds stress is shown in figures 5.28 and 5.29 for each configuration. At x/T = 1.5, the Reynold stress at the flat plate boundary and at the wing

surface is relatively high compared to the freestream or even at the vortex location, with the exception of the antifairing, which is capable of maintaining it relatively low. Additionally, the silhouette of the vortex is reflected in this quantity. For the clean, VG, and antifairing configurations, a fairly distinguishable shape of the HSV legs is appreciated, while for the fairing it takes a more flatten shape. This last observation is preserved along all the planes to the trailing edge. The fluctuating intensity at the vortex core location does not vary considerably but it does reduce on the boundary. It can be said that the antifairing configuration has the least streamwise Reynolds stress on the plate, followed by the fairing, clean and VG configurations.

(a) Clean.

(b) Fairing.

(c) VG.

(d) Antifairing.
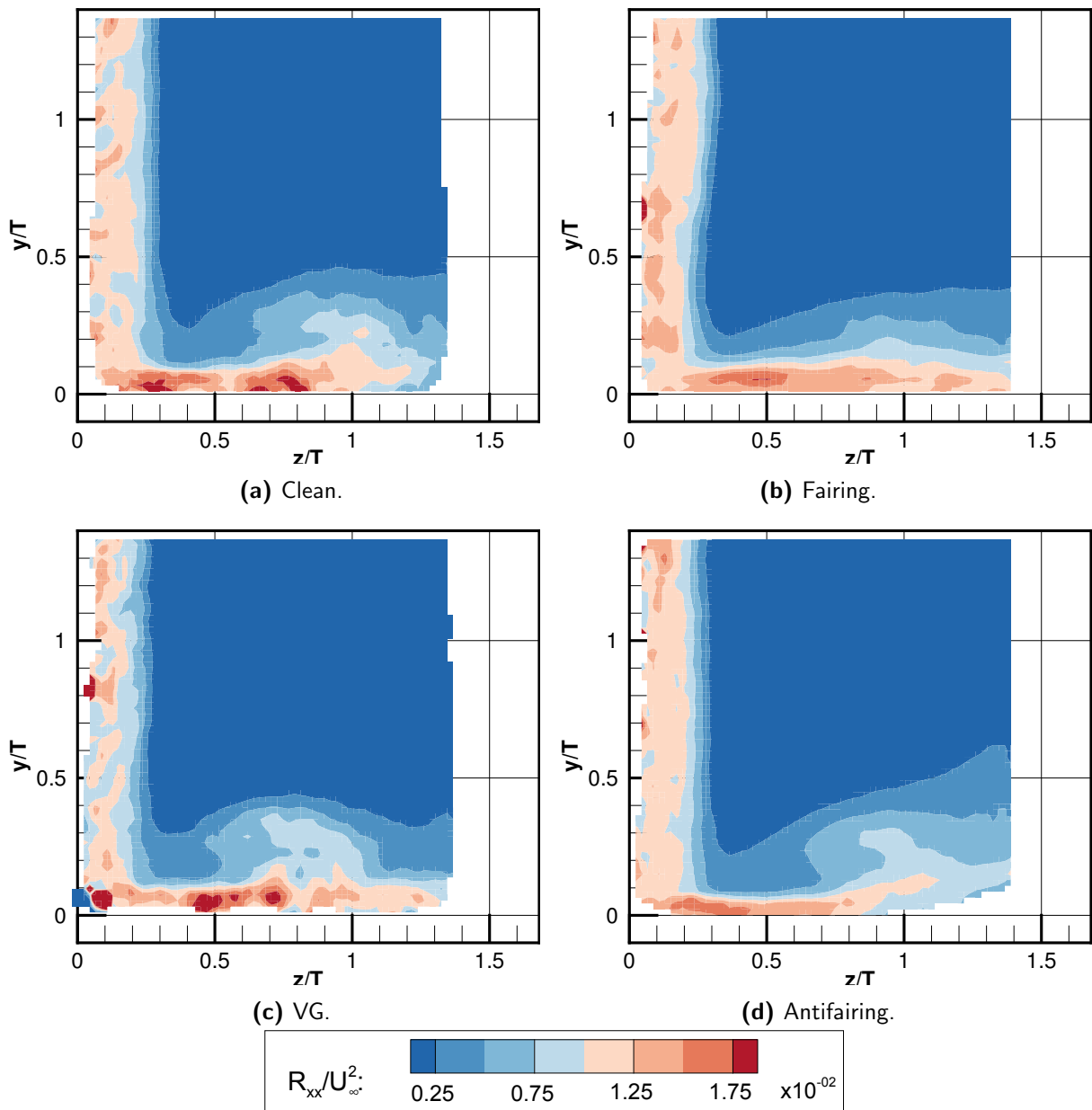
Figure 5.29: Streamwise Reynolds stress at $x/T = 4$.

The Reynolds stress in the spanwise direction behaves equally as the R_{xx}: a silhouette of the vortex confines a region of high fluctuation. At x/T = 1.5, the R_{yy} values around the vortex of the VG configuration resemble to the one from the antifairing, which is higher than in the reference clean configuration. The fairing presents a much lower R_{yy} value. Further downstream at x/T = 4, the contour level is adjusted in order to visualize the small changes. The clean, antifairing and VG configurations have a similar performance, restraining the fluctuations around the HSV core. On the other hand, in the fairing configuration the fluctuations resultant from the HSV are spread out over the plate surface.

(a) Clean.

(b) Fairing.

(c) VG.

(d) Antifairing.

R_{yy}/U_∞^2:   0.25   0.50   0.75   1.00   x10^{-02}
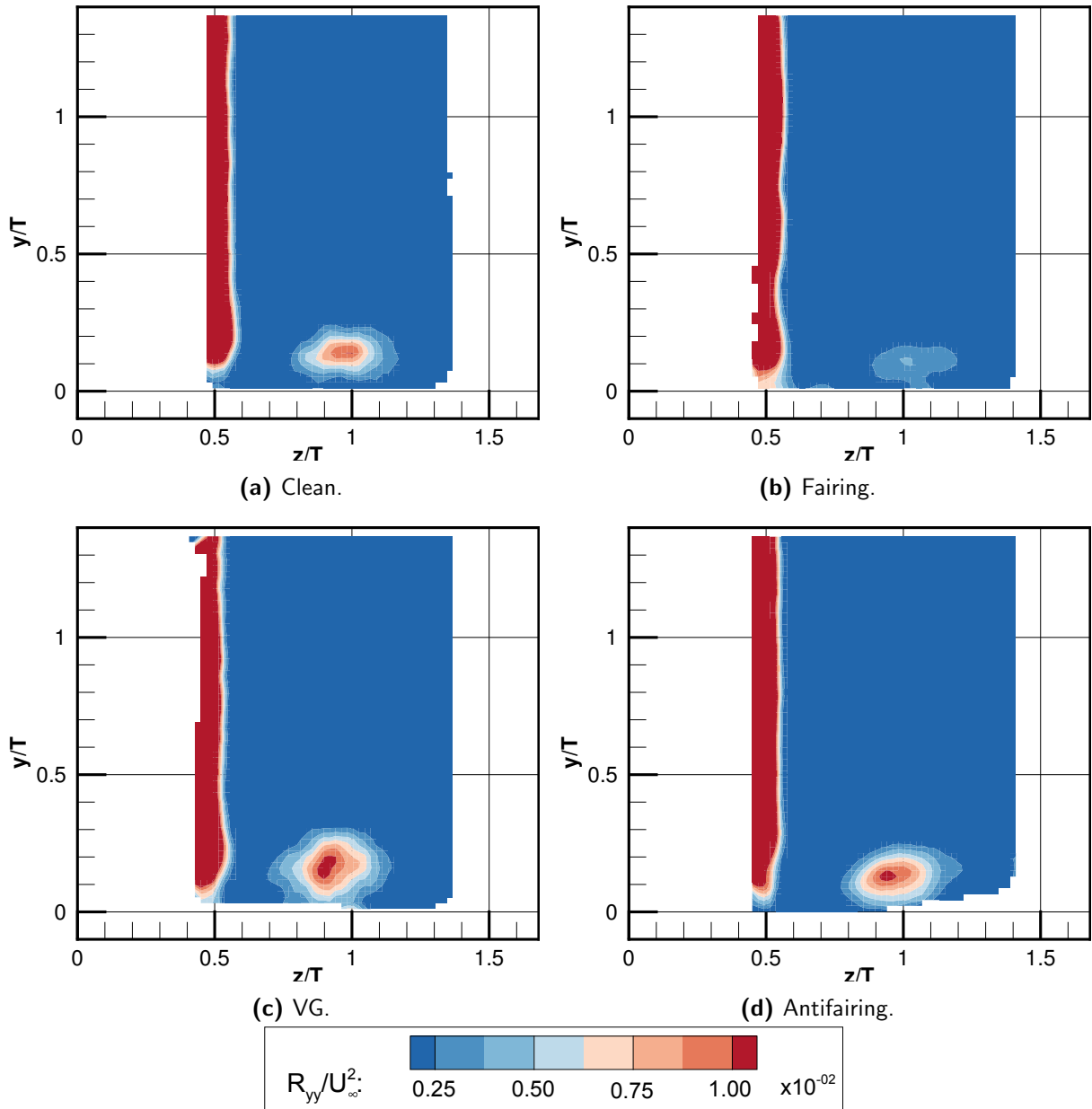
Figure 5.30: Spanwise Reynolds stress at x/T = 1.5.

The evolution of the Reynolds stress in the normal direction along the streamwise direction

(a) Clean.

(b) Fairing.

(c) VG.

(d) Antifairing.

R_{yy}/U_∞^2: 2.0   2.8   3.6   4.4   x10^{-03}
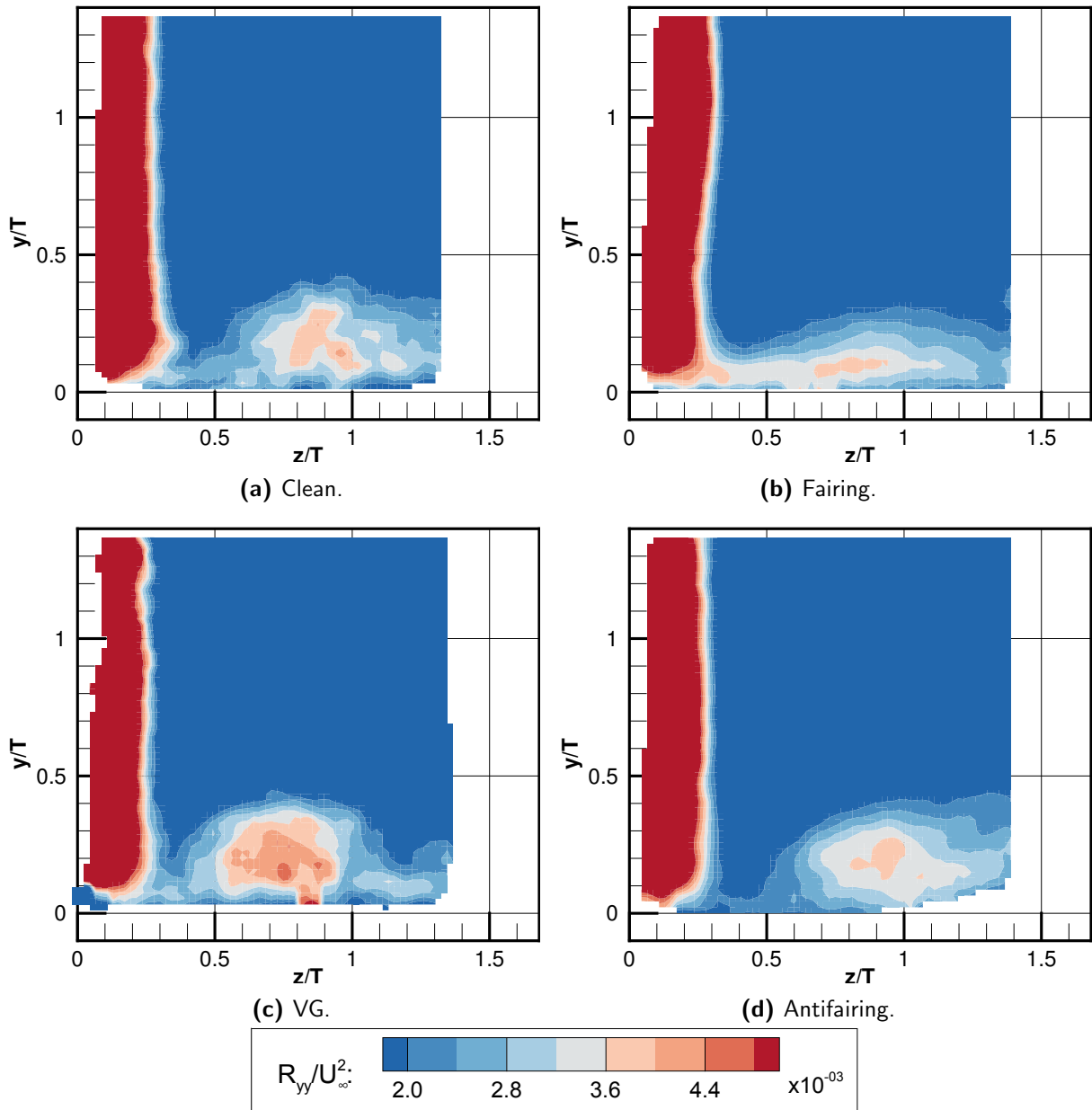
Figure 5.31: Spanwise Reynolds stress at $x/T = 4$.

follows a similar trend as in other directions. The VG configuration is the one with the strongest fluctuation and the antifairing the one with least fluctuation. This classification follows until the end of the junction. The high fluctuation in the normal direction suggest that the vortex has some sort of oscillating action like the meandering effect defined in the literature. However, this effect cannot be proven with the time-averaged data presented in this work.

Overall, it can be said that when the HSV wraps around the wing model, the generated fluctuations has higher intensity in the spanwise and normal to wing direction than the

streamwise direction. This effect is observed in all configurations and the fairing is the one which can overcome the high fluctuations most efficiently in the first half of the wing-flat plate juncture, but performs moderately downstream. Despite the vortex induced fluctuations are lower in the streamwise direction, it is masked by the streamwise turbulence in the boundary layer which is higher. In this aspect, the antifairing is capable of eliminating the boundary turbulence. However, it could also be the case that the boundary layer is not well captured. Moreover, the Reynolds stress intensity in the wing's normal direction is almost double the strength of the spanwise direction. From this results, it can be deduced that the meandering effect occurs mainly such direction. For an overview on the turbulence level, the peak Reynolds stress around the vortex core is recorded in table 5.3.

Table 5.3: Peak Reynolds stress around the vortex core location at x/T = 1.5 and 4.

x/T=	1.5			4			
	R_{xx}/U_∞^2	R_{yy}/U_∞^2	R_{zz}/U_∞^2	R_{xx}/U_∞^2	R_{yy}/U_∞^2	R_{zz}/U_∞^2	
Clean	2.26	1.00	1.47	1.97	0.42	0.80	
Fairing	1.93	0.51	1.31	1.49	0.39	0.75	$\times 10^{-2}$
VG	2.54	1.05	1.91	2.12	0.46	0.85	
Antifairing	0.73	1.03	1.29	1.08	0.39	0.80	

(a) Clean.

(b) Fairing.

(c) VG.

(d) Antifairing.

R_{zz}/U_∞^2: 0.25 0.75 1.25 1.75 x10^{-02}
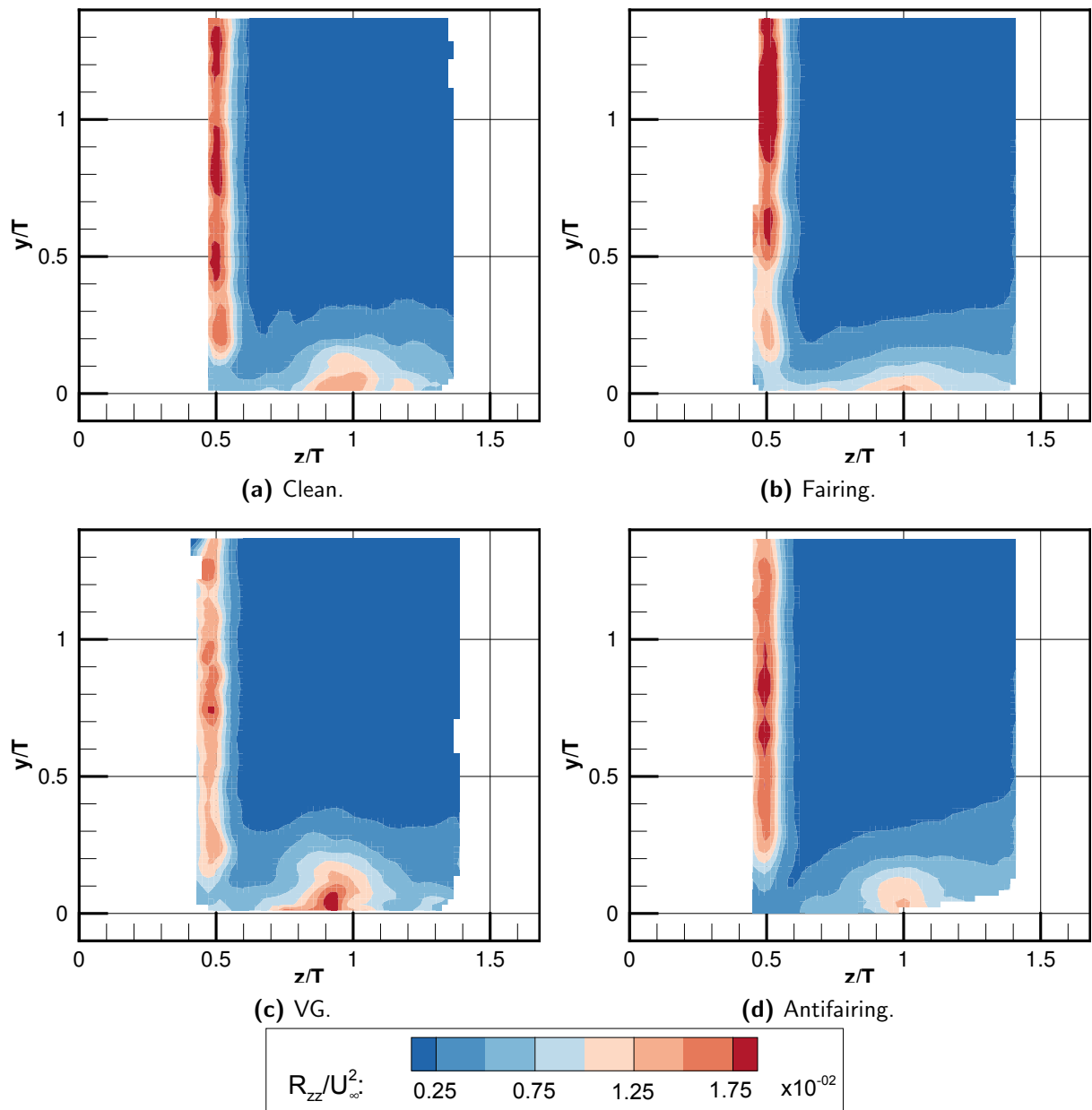
Figure 5.32: Normal Reynolds stress at $x/T = 1.5$.

(a) Clean.

(b) Fairing.

(c) VG.

(d) Antifairing.
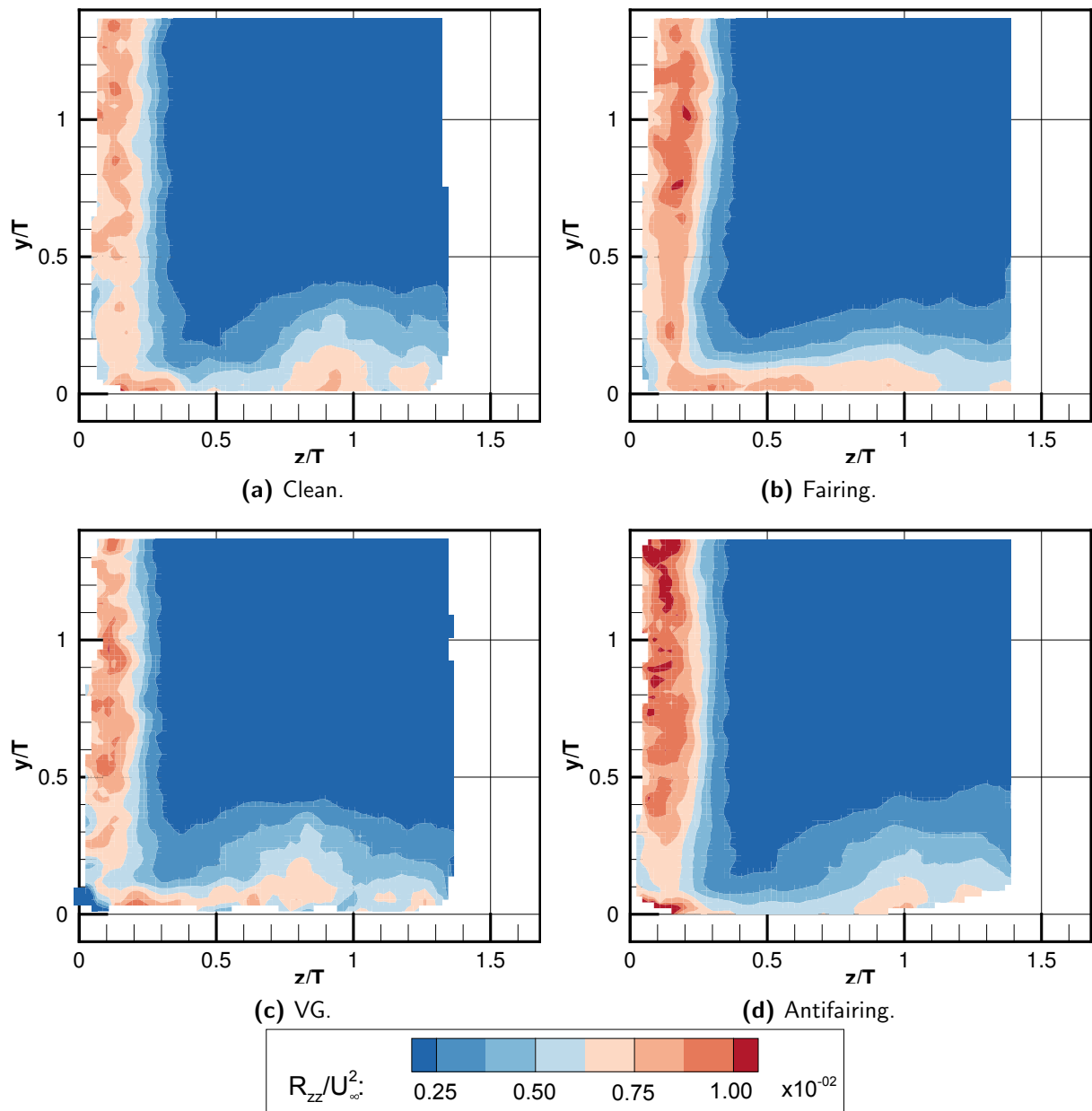
Figure 5.33: Normal Reynolds stress at $x/T = 4$.

5.4   Comparison with literatures

Numerous researches on the topic of junction flow have focused in the inception of the HSV system, while have left unstudied the vortex legs regions. For this reason, only a few literatures are comparable to this study.

5.4.1   Clean configuration

The clean configuration is compared to the research done by Fleming et al. (1993), in which the flow around a Rood wing-flat plate junction was studied with hot-wire technique at multiple planes (see figure 5.34). The experiment was conducted at $Re_\theta = 6300$, and although the Reynolds number based on the momentum thickness is almost three times higher than the one in the current research, the momentum thickness is still comparable ($\theta/T = 0.0548$).

The results of the current research are shown in figure 5.35, the different planes are adjusted to the same locations as in the literature for a fair comparison, with the exception of the subfigure f, which is measured at the wake x/T = 7.4.

In figure 5.35 it is observed that the tomographic measurement technique can measure the velocity close to the wing surface. Apart from the additional information given by the new measurement technique, the obtained results are relatively similar. To begin with, the height of the contour line $U/U_\infty = 1$ grows with the streamwise direction in a similar matter. In addition, the low velocity contour lines ($U/U_\infty < 1$) are twisted around z/T = 0.9 in the planes b-e, observation which suggests the transfer of momentum by the HSV's action. The efficiency of the transfer action appears to be more intense in the literature.

The reason for the differences observed between the two works is due to the flow conditions. In the work performed by Fleming et al. (1993), both the wing model and the freestream velocity are larger than in the current study. Hence the Reynolds number and the MDF (7.24 $\times 10^8$) are almost an order of magnitude higher than the present performed experiments. Such conditions derive to the generation of a stronger vortex which persists downstream. Despite the distinctions, the velocity around the wing junction is well captured with fair similarity. In addition, the extra flow characteristics obtained from the tomographic measurement can effectively define the vortical structures in three-dimensions.

5.4.2   Fairing

Koers (2017) performed both sPIV measurements and CFD analysis in the wake of a NACA0015-flat plate junction. Besides the basic airfoil formed junction, the author tested as well the implementation of leading edge fairing and antifairing. Results obtained from the experiments are chosen to be compared with.
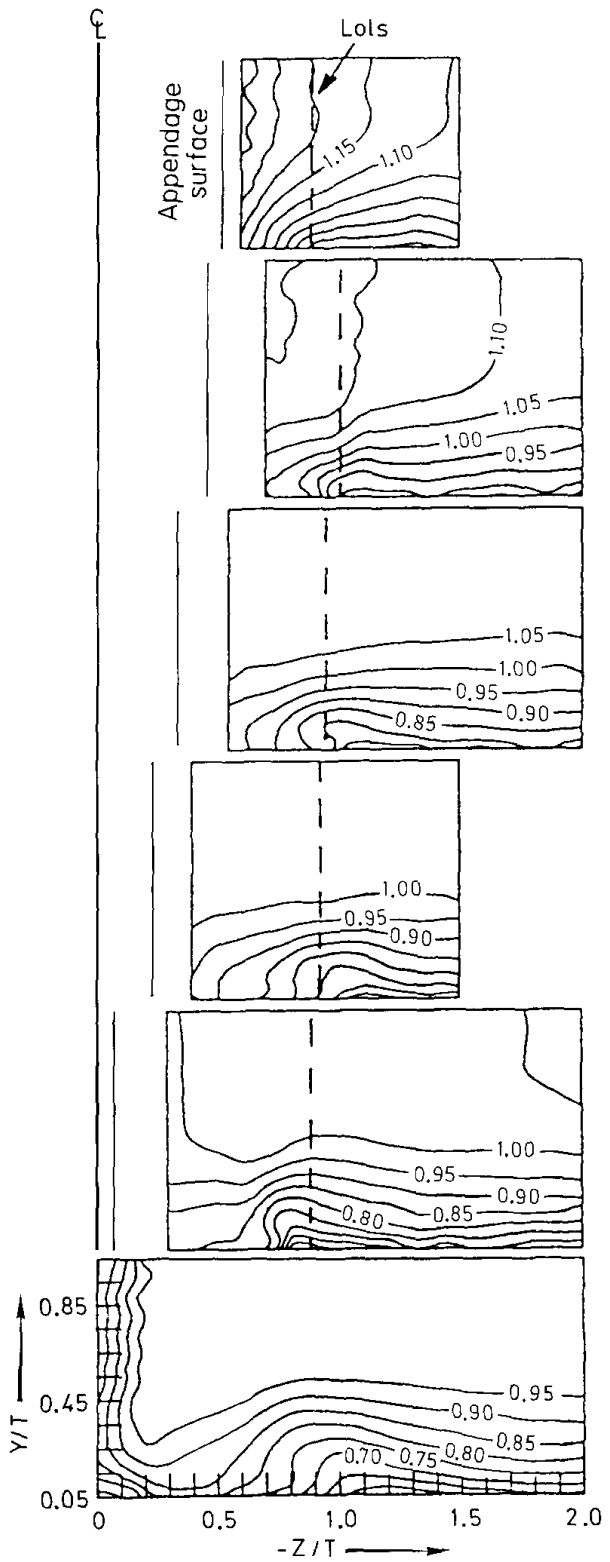
Figure 5.34: Contour of streamwise velocity around a clean junction at different planes. The locations of the planes (a-g) are x/T = 0.75, 1.8, 2.7, 3.2, 3.9, 6.3 respectively. Image adapted from Fleming et al. (1993).
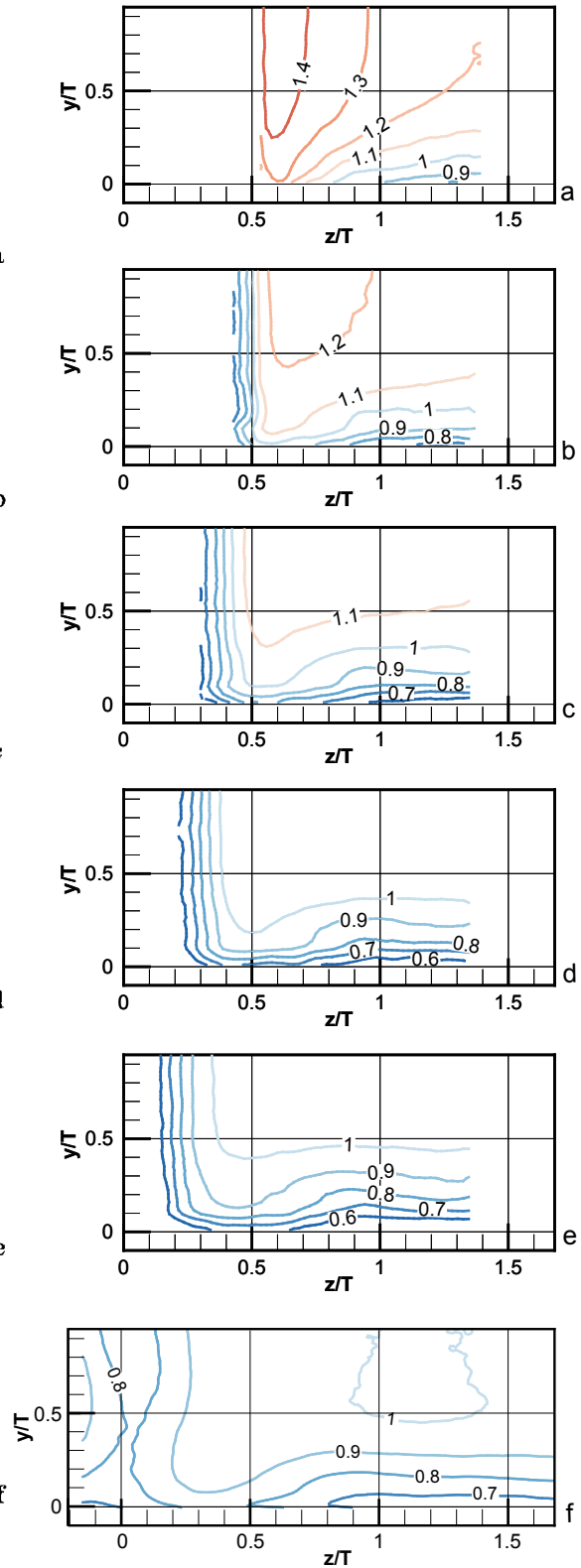
Figure 5.35: Contour of the streamwise velocity at the same locations as in figure 5.34 a-e. Subfigure f is the velocity contour of the sPIV wake measurement at x/T = 7.4.

In the experiments, the junction was tested at various freestream velocity. Among all, the slowest speed ($U_\infty = 10 m/s$) is selected for the comparison. At this velocity, the $Re_T = 7.2 \times 10^4$, with $Re_\theta = 927$, resulting a MDF of 6.67×10^7. It closely matches with the value obtained in the experiments performed in this project. The results of the fairing configuration are displayed in figure 5.36.
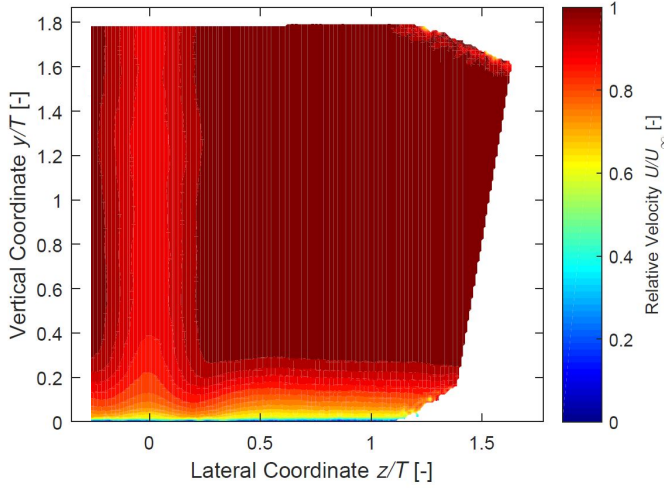
Figure 5.36: Streamwise velocity contour of the fairing configuration. Image adapted from Koers (2017).
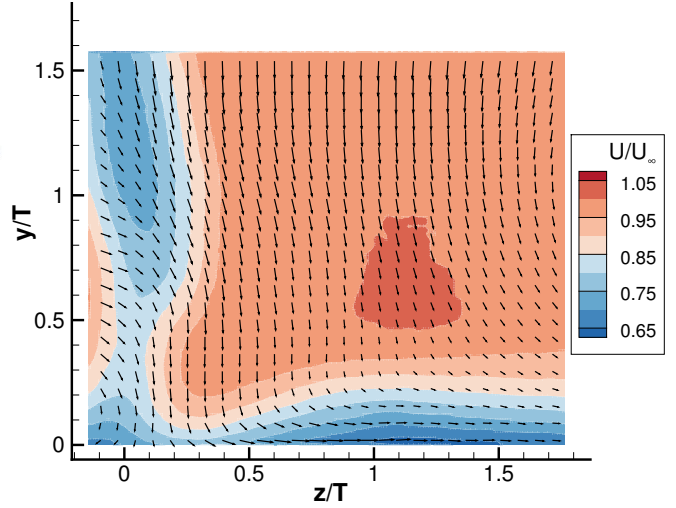
Figure 5.37: Reproduction of figure 5.4a.

The wake of the fairing, which is shown previously in figure 5.4a, is shown again in figure 5.37 for an easier side-by-side comparison. In the proximity of the chord line, at z/T = 0.25, the inrush of high momentum fluid can be found in both cases. In the same region, the lowest point that can be reached with a streamwise velocity of $U/U_\infty = 1$ is y/T = 0.2. In the direction normal to the wing, it is observed that the boundary layer recovers to its original thickness in a gradual manner. Nevertheless, this recovery is quicker in Koers (2017) work than the current one.

The fact that the MDF in the two cases is similar but the velocity fields are slightly different imply the strength of the created HSV are different. Since the NACA0015 airfoil model has a bluntness factor of 0.045, the produced HSV is by default weaker than the one produced by a Rood wing, which has BF = 0.32. In combination with the leading edge fairing, the effect is further minimized. For these reasons, the observed wakes are comparable in terms of the flow contours but a lesser effect of the vortex is observed in the literature results.

5.4.3   Vortex Generators

A wake assessment with vortex generators in spacing configuration was performed by Andoh et al. (2009) using X type hot wire probes. Two spacing configurations ,0.75T and 1.8T, were tested in the experiment. The VG were positioned 2.75T upstream of the junction leading edge. The experiment was conducted at $Re_T = 6.5 \times 10^4$ and $Re_\theta = 1670$, with a MDF of 1.1×10^8.

In the experiment, the X-probe was rotated for each acquisition point in space so it could measure the three components of velocity. The velocity data obtained at the wake, x/T = 6.3, was averaged and displayed in figure 5.38.

The streamwise vortex generated by the control device has a larger area of influence than the current results, as the vortex generators in Andoh et al. (2009) experiments are taller (0.15T compared to 0.1T). The same results show that the small spacing VG configurations yields a strong streamwise deceleration at the chord line. According to the author, it is caused by the interaction of both HSV and the streamwise vortex wake. On the other hand, the large VG spacing configuration presents a strong interaction of the HSV with the low momentum boundary layer flow.

(a) VG separated 0.75T apart.   **(b)** VG separated 1.8T apart.
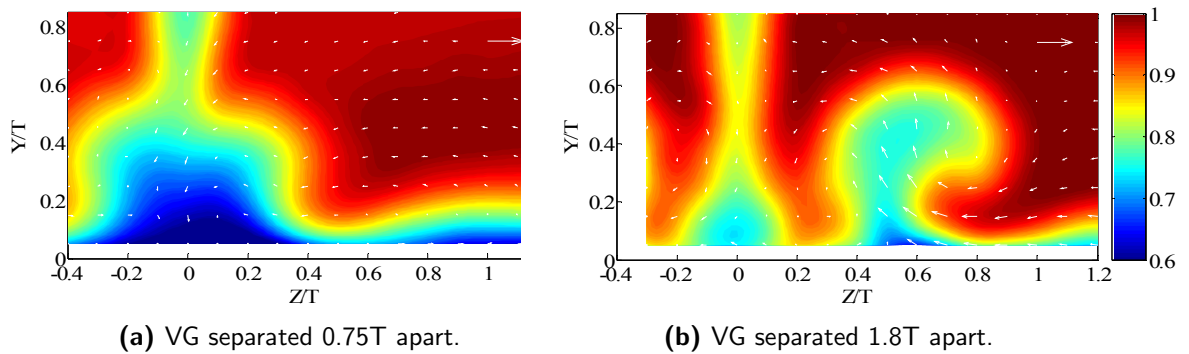
Figure 5.38: Velocity contours of a junction flow wake subjected to the effects of VG in different spacing. Source: Andoh et al. (2009)

(a) Reproduction of figure 5.4c.   **(b)** Reproduction of figure 5.4d.
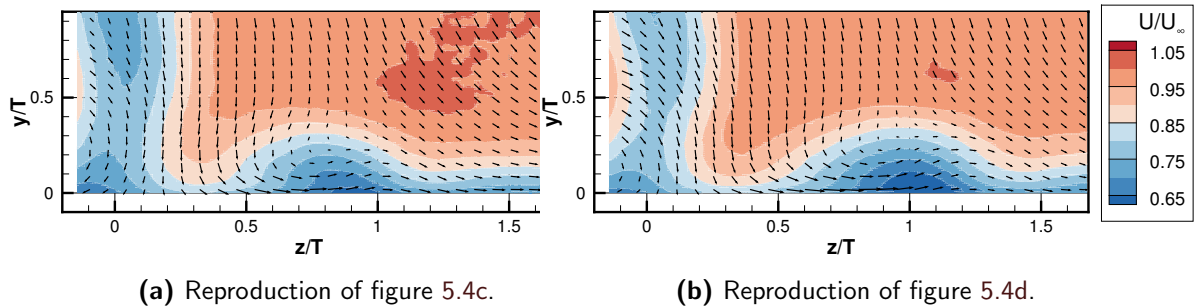
Figure 5.39: Reproduction of the wake velocity contours of the VG in spacing configurations.

The differences observed between the two configurations in the present study are less pronounced. In addition, they are strongly different from the literature. Nonetheless, it can be conjectured that finding the optimal spacing for the VG is not trivial. As it is shown in figures 5.38 and 5.39, various VG spacing are tested and none have eliminated the presence of the low momentum region. Nevertheless, it can also be the case that VG cannot eliminate completely the HSV. Focusing in between the literature and the current study, it can be concluded that the small vortex generator from this study is less efficient in contributing to the elimination of the HSV and the momentum transfer. As it is shown in figure 5.38b and 5.39b, less interaction between the boundary layer and freestream is observed for the shorter VG.

5.4.4 Antifairing

The only open literature on the antifairing is from Koers (2017). In this configuration, the flow condition is slightly different from the fairing condition discussed previously due to the installation of the antifairing plate on the existing wind tunnel walls. As a result, the boundary layer thickens, resulting a $Re_\theta = 1785$ and a MDF of 1.3×10^8.

The velocities of the wake measurement with sPIV, both from the literature and the present work, are presented in figures 5.40 and 5.41.
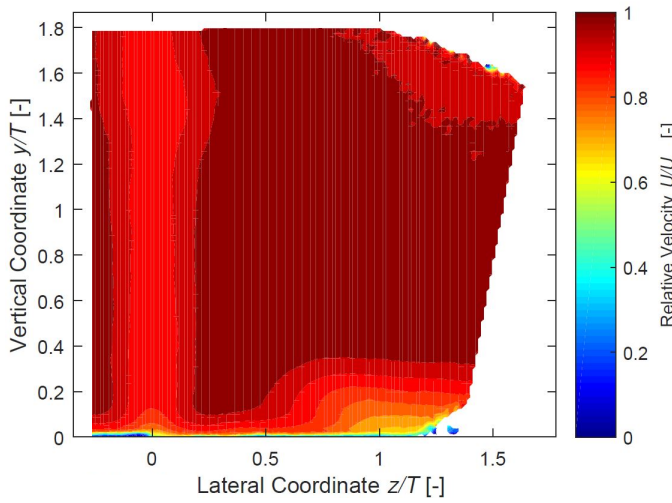
Figure 5.40: Streamwise velocity contour of the antifairing configuration. Image adapted from Koers (2017).
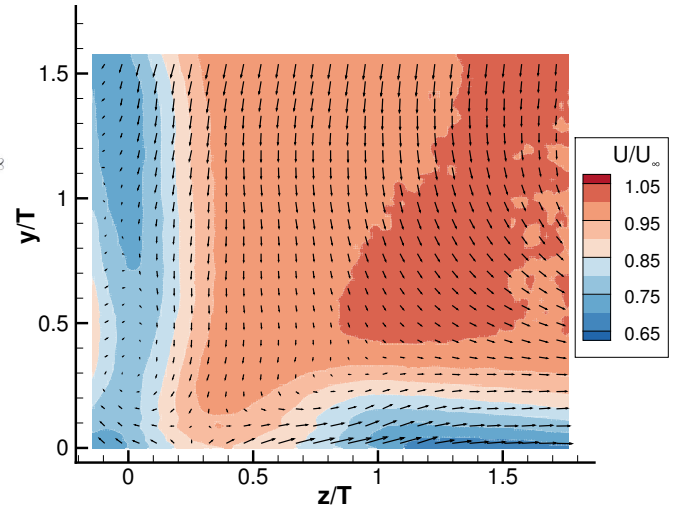
Figure 5.41: Reproduction of figure 5.4e.

As a general review on the comparison, the results from both sources closely match. A high momentum region is observed close to the junction region, from z/T 0.1 to 0.5. Besides, the presumed vortex is also found to be moved away from the chord line in the literature, where the streamwise velocity decreases in approaching the point of z/T = 1.1 on the flat surface. The boundary layer thickness between the two studies is also similar and decreases the further to the chord line is.

5.5 Working Mechanisms of the Control Devices

Following the analysis of the measured velocity field of the different configurations, a series of hypothesis are proposed to explain the working mechanisms of the control devices.

5.5.1 Fairing

It has been shown that the fairing is the configuration which reduces the most the strength of the HSV. It also reduces the Reynolds stresses in the first half of the wing-flat plate juncture, before the HSV breakdown occurs. However, the stresses are not as low as expected downstream.

(a) Close-up view of streamwise velocity at the fairing's leading edge.

(b) Close-up view of spanwise velocity at the fairing's leading edge.
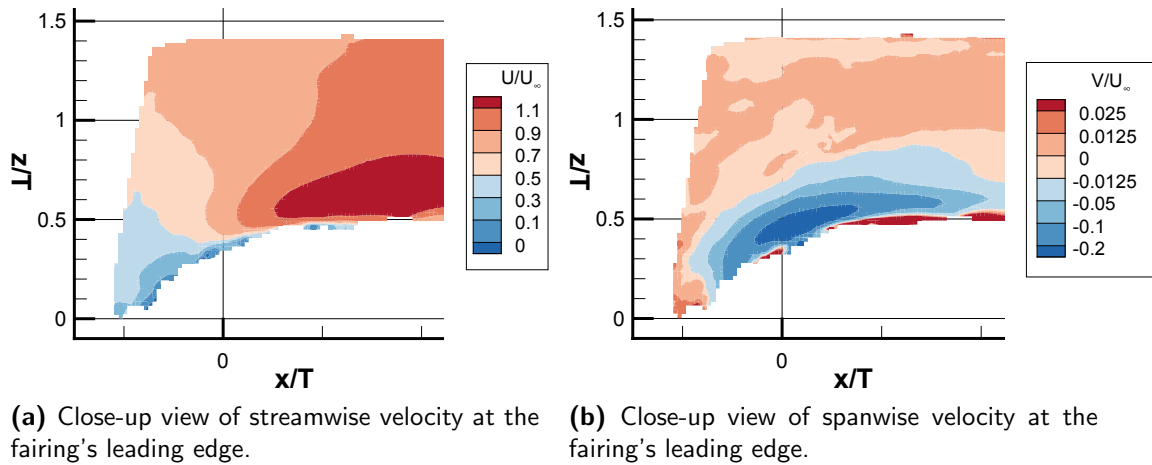
Figure 5.42: Velocity contours of the fairing's leading edge at $y/T = 0.07$.

The weak HSV formed at the leading edge is associated with the less intense leading edge separation. Oil-flow visualisation was performed in Koers (2017) thesis and it shows that the flow on the flat plate reaches the fairing leading edge and separates afterwards. The separation point can be deduced from figure 5.42, at the leading edge $z/T = 0.1$ where the streamwise and spanwise velocity have close to zero value. The reasons for the HSV to be weaker in the fairing than in the clean configuration are, first of all, the downwash velocity is partially counteracted by the upward flow from the fairing. Secondly, as the fairing surface is curved, the recirculation region of the HSV head is reduced, hence the circular shape of a normal HSV cannot be formed but limited to a more flatten one. Furthermore, the vortex peak vorticity is reduced as the non-circular shape vortex does not hold efficiently the swirl motion.

Starting with a weaker and more flatten vortex, it breaks down soon after passing through the maximum thickness region. It has been seen in the Reynolds stresses that high fluctuating regions on the plate are spread along the wing's normal direction downstream. This effect is due to the flow, which now contains small vortical structures resulted from the HSV break down, reattaches on the wing as the thickness is tapering downstream. In this matter, it implies that a strong HSV prevents the reattachment of the flow on the wing downtream, as the vortex pushes the boundary flow away from it. Recalling the oil-film measurement from Koers (2017), it can confirm this statement: the flow on the flat plate reattaches on the wing towards the tail. As a result, the unsteadiness derived from the vortex breakdown is spread and contaminates a larger area.

5.5.2 VG

The VG in spacing configuration has shown minimum improvement in terms of drag reduction or turbulence level. The idea of combining the counter rotating vortices is effective if and only if the VG spacing is set concentric to the vortex leg, and taking into consideration the curvature effect close to the leading edge.

From results on the vorticity contours and Reynolds stresses, the diameter of the vortex is slightly larger in size and intensity. Nevertheless, although the positive vortex is located in the vorticity contour, it is not reflected in the contours of the Reynolds stresses. In fact, its effect is merged with the main HSV, despite its influence is minimum. Comparing the Reynolds stresses of the VG configuration with the clean configuration, the contour level is reduced at about z/T = 1.25, see figure 5.32. Nevertheless, since the vortex originated from the VG is located parallel to the HSV, the swirling motion of the HSV increases, and so does the turbulence level at the main vortex core.

5.5.3 Antifairing

The dented surface design does not prevent at all the inception of the HSV. Nevertheless, this is the configuration which returns the least streamwise Reynolds stress among all. Additionally, it has been shown in the wake survey that the wake of the vortex is pushed away from the wing-plate juncture. At the same time, the juncture is compensated by high streamwise momentum flow. The combination of all these effects indicates this is the design with the most drag reduction.

The boundary layer profile at (X,Z) = (0, 1.2T) is shown in figure 5.43. The normalised streamwise velocity is higher than unity away from the wall due to the proximity to the wing model, which causes the flow to accelerate. From the figure it can be estimated that all configurations with exception of the antifairing have a boundary layer thickness in the order of 0.6T, which is the same as measured in the boundary assessment with PIV. On the other hand, the antifairing presents a velocity profile with a positive slope beyond the height of 0.6T. Such observation suggests the boundary layer is thickened by the antifairing plate, primarily in the beginning of the dent where the flow experiences an adverse pressure gradient. The same observation can be found in other locations upstream of the model. Although the boundary layer immediate to the wall is not resolved, as the boundary layer is thickened, it is expected that the value of velocity gradient (du/dy) at the wall is lower. Consequently, the wall shear stress is also lower for the antifairing than the clean configuration in the fore part of the junction.

According to the literature (Fleming 1991), the strength of the HSV scales with the incoming boundary layer momentum thickness. Hence, momentum thickness is calculated for the measured velocity profiles and the results are shown in table 5.4. The momentum thickness of the antifairing configuration is thicker than the other configurations, in combination with the stronger HSV observed in the results, it is in agreement with the literature. For the
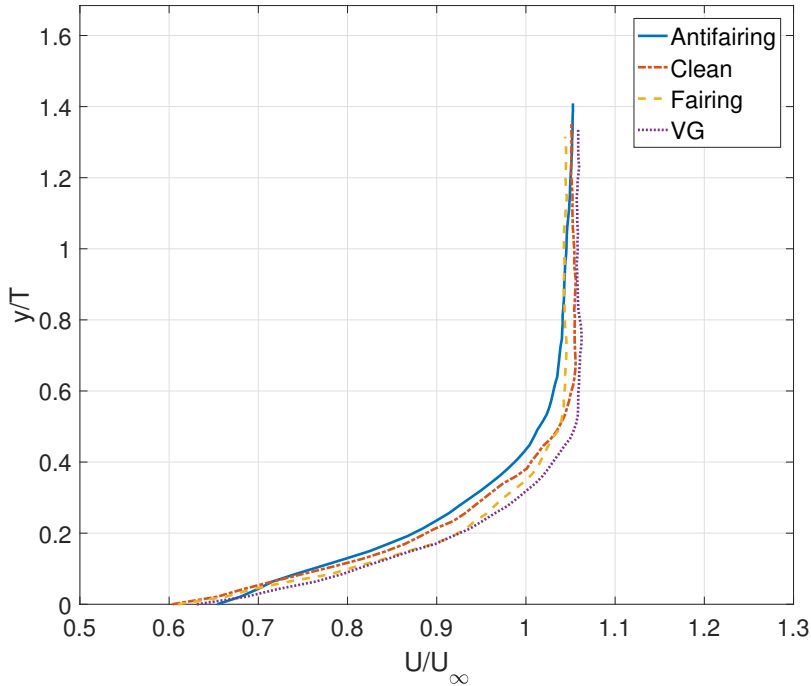
Figure 5.43: Boundary layer profile at $(X,Z) = (0, 1.2T)$

Table 5.4: Boundary layer properties measured in figure 5.43

	Displacement thickness	Momentum thickness
Clean	0.068T | 3.21 mm	0.053T | 2.51 mm
Fairing	0.064T | 3.06 mm	0.049T | 2.32 mm
VG	0.059T | 2.79 mm	0.046T | 2.19 mm
Antifairing	0.075T | 3.56 mm	0.060T | 2.83 mm

reason that the HSV is stronger, it can maintain its structure slightly longer than the clean configuration.

As the HSV is located in the dent, the induced velocity experiences a small acceleration when it recovers from the dent to the flat plate level in the normal direction of the wing. Due to this acceleration, the wake of the HSV follow the same trend after the trailing edge. Thus, the low momentum region appears to be shifted away from the chord line in the wake. Besides, at the most downstream region of the dent, the surface also recovers to the flat level in the streamwise direction, hence, the surface has a positive slope which accelerates the flow on the boundary. The outcome of such is the high momentum flow at the juncture observed in the wake survey. The combined effect of the acceleration and the shifted away wake of the HSV yield a lower value when computing the momentum deficit.

Although the HSV strength is enhanced, it has to be said that the contours of the streamwise velocity and vortical structure for the antifairing does not differ considerably compared with the clean configuration around the wing. This finding suggests that the drag reduction effect has no relation with the flow features in the proximity of the junction, but has to do with

the beginning and the end of the dented surface. Referring to the works from Koers (2017), drag distribution over the clean and antifairing configuration is obtained with numerical analysis. The results show the drag coefficient is decreased for the antifairing in the beginning of the dent and increased in the rear end. For the section in between, where the wing model is located, minimum differences are observed. In such matter, the flow characterization performed in this work is not sufficient to understand the drag reduction effect, as the field of study is limited to around the wing-flat plate juncture. Nevertheless, the momentum deficit calculated in the wake can give a glimpse on the global effect of the antifairing.

Chapter 6

Conclusions and recommendations

When the flow on a flat surface encounters an obstacle, it yields an unsteady three-dimensional vortex at the fore part of the protuberance, which wraps around the object. This fluid phenomenon is known as Horseshoe vortex. Extensive studies have been conducted in order to understand and control it, as the apparition of the HSV comes accompanied with side effects, such as: increment in drag force and turbulence level in an aircraft fuselage-wing configuration, scouring of the riverbed around a bridge pier and more. Besides, the newly on-site developed seeder for large-scale PIV application is essentially a protuberance introduced in a wind tunnel, modifying hence the facility performance. For this reason, the present work aims to understanding the flow structures of a junction flow, and study the viability of passive flow control devices as means of corrective methods.

6.1 Conclusions

An experimental study is performed in order to achieve the project goals. A wing-flat plate junction is created in a wind tunnel and various passive flow control devices, leading edge fairing, vortex generators and antifairing, are tested. The flow field around the junction is captured with large-scale tomographic PTV measurement with the so called Helium Filled Soap Bubbles as seeding particles. The PTV data is processed with the Shake-The-Box algorithm. An auxiliary measurement in the wake region and posterior calculation of the momentum deficits assist the determination of the control devices with least drag force.

The measured velocity around the junction suggests that the fairing has the least distorted velocity contour across different streamwise planes. For the VG and the antifairing, the contours are strongly distorted due to the action of the HSV legs. The momentum deficit calculation at the wake indicates that the VG, regardless the configuration variants, show an increment in the drag force compared to the clean configuration. The VG in 1T spacing is the least compromised among its variants with only a 4% of increment. The fairing and the

antifairing show a drag reduction of 2% and almost 17% respectively.

The vorticity fields, with support of Q-criterion vortex identification method, show the vortical structures of the different configurations. The measured peak vorticity value and also the calculated circulations around the vortex core indicate that the fairing generates the weakest HSV. The corresponding circulation value is about 45% of the clean reference case. The VG and the antifairing present a stronger vortex, with circulation values of approximately 21% and 16% higher than the clean one.

Among the three control devices and at the wake region, the VG creates about 15% higher peak turbulence level than the clean configuration. The antifairing presents a streamwise turbulence level reduction of about 8% from the reference, and almost no improvement in the directions normal to it. The fairing has higher turbulence in the streamwise of roughly 4%, but about 7% less fluctuating level is observed in the other components in respect to the baseline.

To conclude, the HSV system associated with the junction flow can be reduced with the use of leading edge fairing, while the vortex is still present for the VG and the antifairing configurations. Although the HSV exists in the antifairing configuration, the calculated momentum deficit is lower than in the fairing configuration. The fairing is effective for reducing the turbulence level in the spanwise and normal to wing direction; while the antifairing reduces mostly the streamwise turbulence at the wake of the junction.

6.2   Recommendations

The use of large-scale tomographic PTV technique is proved applicable for the characterization of the wing-flat plate formed junction flow. With this technique, the junction region is studied as a whole and the visualization of the associated HSV is possible. This visualization allows the better interpretation of the flow behaviour when passive flow control devices are applied. Nevertheless, some limitations and flaws are found and the possible solutions are suggested.

It was observed in the results that the antifairing has an exceptionally low streamwise Reynolds stress close to the plate. A reason for this observation is that the flow inside the dent has lower velocity and is more steady. Nevertheless, it could also be the case that part of the dented region is within a blind zone of the cameras. Hence, to ensure the entire dented region is viewed by all cameras, they should be positioned with higher pitch angle than the current setup if a similar experiment is repeated to avoid ambiguity.

In connection with the antifairing, it was observed that it has a similar flow topology as the clean configuration. Thus the drag reduction mechanism might not be focused around the wing-plate junction itself but in the fore and rear position of the dent. In order to prove this hypothesis, high resolution measurements such as sPIV or classical tomo-PIV/PTV with fog particles should be performed to these regions. The reason for using such technique is to ensure the boundary layer is resolved, as it plays a strong role in the drag reduction effect of

the antifairing.

Moreover, if a more detailed drag analysis is intended, it should be further supported by other measurement techniques such as balance measurement. This practice is recommended because the FOV of the current wake measurement is relatively small, so it might not capture completely the wake of the junction. For instance, the wake of the antifairing configuration appears to drift away from the chord line.

Finally, as the junction flow system is highly dynamic, the possibility to obtain instantaneous field would give a better insight of the flow mechanism. It is not possible in the current work due to the seeding concentration is relatively low. Hence it cannot fully define the flow field with just a single snapshot. Nevertheless, this flaw might be overcame in the future when a new seeding system with higher production rate is developed.

A new perspective to the understanding of junction flow is explored in this project with the state-of-the-art large-scale PTV technique. Passive flow control devices are implemented to test their influences on the junction flow. A clear strength reduction of the HSV is found for the classical leading edge fairing but the working mechanisms of the novel antifairing is still unclear. With the according recommendations, this drawback is expected to be overcame and the flow topology is defined with greater details. In the end, the applicability of this control device in engineering applications could be possible if it is proved to be effective.

Bibliography

Nereida Agüera, Gioacchino Cafiero, Tommaso Astarita, and Stefano Discetti. Ensemble 3D PTV for high resolution turbulent statistics. *Measurement Science and Technology*, 27(12):124011, 2016. ISSN 0957-0233. doi: 10.1088/0957-0233/27/12/124011. URL http://stacks.iop.org/0957-0233/27/i=12/a=124011?key=crossref.6376417744346103686b803c83b6cb5b.

J. Anderson. *Fundamentals of Aerodynamics*. McGraw-Hill Education, 2010. ISBN 9780073398105.

Masaharu Andoh, Masahiro Motosuke, and Shinji Honami. Interaction of Longitudinal Vortex with Horseshoe Vortex Configuration Effect of Longitudinal Vortex. In *39th AIAA Fluid Dynamics Conference*, Fluid Dynamics and Co-located Conferences. American Institute of Aeronautics and Astronautics, San Antonio, 2009. doi: doi:10.2514/6.2009-4176. URL http://dx.doi.org/10.2514/6.2009-4176.

N. Apsilidis, P. Diplas, C. L. Dancey, and P. Bouratsis. Time-resolved flow dynamics and Reynolds number effects at a wallcylinder junction. *Journal of Fluid Mechanics*, 776(2015): 475–511, 2015. ISSN 0022-1120. doi: 10.1017/jfm.2015.341.

D. D. Apsley and M. A. Leschziner. Investigation of advanced turbulence models for the flow in a generic wing-body junction. *Flow, Turbulence and Combustion*, 67(1):25–55, 2002. ISSN 13866184. doi: 10.1023/A:1013598401276.

Callum Atkinson and Julio Soria. An efficient simultaneous reconstruction technique for tomographic particle image velocimetry. *Experiments in Fluids*, 47(4):553, Aug 2009. ISSN 1432-1114. doi: 10.1007/s00348-009-0728-0. URL https://doi.org/10.1007/s00348-009-0728-0.

C.J. Baker. The laminar horseshoe vortex. *Journal of Fluid Mech*, 95(2):347–367, 1978a. doi: 10.1017/S0022112079001506.

C.J. Baker. *Vortex flow around the bases of obstacles*. PhD thesis, University of Cambridge, 1978b.

C.J. Baker. The turbulent horseshoe vortex. *Journal of Wind Engineering and Industrial Aerodynamics*, 6(1):9–23, 1980. doi: 10.1016/0167-6105(80)90018-5.

C.J. Baker. The Oscillation of Horseshoe Vortex System. *Journal of Fluids Engineering*, 114 (March 1992):134, 1992.

T.J. Barber. An Investigation of Strut-Wall Intersection Losses. *Journal of Aircraft*, 15(10): 166–681, 1978. doi: http://dx.doi.org/10.2514/3.58427.

Zeno Belligoli. Optimization of a wing-body junction. Master's thesis, Delft University of Technology, 2015.

Matthew Bloxham, Jeffrey Bons, and Rebecca Hollis. Horseshoe Vortex Control with Leading Edge Endwall Boundary Layer Removal. In *4th Flow Control Conference*, number June, page 4319, Columbus, 2008. American Institute of Aeronautics and Astronautics. ISBN 978-1-60086-994-5. doi: 10.2514/6.2008-4319. URL http://arc.aiaa.org/doi/abs/10.2514/6.2008-4319.

Mehdi Bordji, Fabien Gand, Sébastien Deck, and Vincent Brunet. Investigation of a Nonlinear Reynolds-Averaged NavierStokes Closure for Corner Flows. *AIAA Journal*, 54(2):386–398, 2016. doi: 10.2514/1.J054313.

Johannes Bosbach, Matthias Kühn, and Claus Wagner. Large scale particle image velocimetry with helium filled soap bubbles. *Experiments in Fluids*, 46(3):539–547, 2009. ISSN 07234864. doi: 10.1007/s00348-008-0579-0. URL https://link.springer.com/content/pdf/10.1007{%}2Fs00348-008-0579-0.pdf.

G.E.P. Box and G.M. Jenkins. *Time series analysis: forecasting and control*. Holden-Day series in time series analysis and digital processing. Holden-Day, 1976. ISBN 9780816211043.

P. Bradshaw. Turbulent Secondary flows. *Annual Review of Fluid Mechanics*, 19(1):53–74, 1987. ISSN 00664189. doi: 10.1146/annurev.fluid.19.1.53.

Alp Caridi, Giuseppe Carlo and, Daniele Ragni, Andrea Sciacchitano, and Fulvio Scarano. A seeding system for large-scale Tomographic PIV in aerodynamics. 56(2):2015, 2015.

Giuseppe Carlo Alp Caridi, Daniele Ragni, Andrea Sciacchitano, and Fulvio Scarano. HFSB-seeding for large-scale tomographic PIV in wind tunnels. *Experiments in Fluids*, 57(12): 190, dec 2016. ISSN 0723-4864. doi: 10.1007/s00348-016-2277-7. URL http://link.springer.com/10.1007/s00348-016-2277-7.

Qigang Chen, Meilan Qi, Qiang Zhong, and Danxun Li. Experimental study on the multimodal dynamics of the turbulent horseshoe vortex system around a circular cylinder. *Physics of Fluids*, 29(1):015106, 2017. ISSN 1070-6631. doi: 10.1063/1.4974523.

J. Cho and K. Kim. Controlling the Horseshoe Vortex by Leading- Edge Chamfer at a Generic Wing-Body Junction. *Journal of the Korean Society of Propulsion Engineers*, 13(2):16–34, 2009.

Michael D Coon and Murray Tobak. Experimental Study of Saddle Point of Attachment in Laminar Junction Flow. *AIAA Journal*, 33(12):2288–2292, 1995.

W. J. Devenport, N. K. Agarwal, M. B. Dewitz, R. L. Simpson, and . PODDAR. Effects of a fillet on the flow past a wing-body junction. *AIAA Journal*, 28(12):2017–2024, 1990. ISSN 0001-1452. doi: 10.2514/3.10517.

William J. Devenport and Roger L. Simpson. Time-dependent and time-averaged turbulence structure near the nose of a wing-body junction. *Journal of Fluid Mechanics*, 210:23, 1990. ISSN 0022-1120. doi: 10.1017/S0022112090001215.

William J. Devenport, Roger L. Simpson, M. B. Dewitz, and N. K. Agarwal. Effects of a leading-edge fillet on the flow past an appendage-body junction. *AIAA Journal*, 30(9): 2177–2183, 1992. doi: 10.2514/3.11201.

G. E. Elsinga, F. Scarano, B. Wieneke, and B. W. Van Oudheusden. Tomographic particle image velocimetry. *Experiments in Fluids*, 41(6):933–947, 2006. ISSN 07234864. doi: 10.1007/s00348-006-0212-z.

Cristian Escauriaza and Fotis Sotiropoulos. Reynolds Number Effects on the Coherent Dynamics of the Turbulent Horseshoe Vortex System. *Flow, Turbulence and Combustion*, 86 (2):231–262, mar 2011. ISSN 1386-6184. doi: 10.1007/s10494-010-9315-y.

J. L. Fleming, R. L. Simpson, J. E. Cowling, and W. J. Devenport. An experimental study of a turbulent wing-body junction and wake flow. *Experiments in Fluids: Experimental Methods and their Applications to Fluid Flow*, 14(5):366–378, 1993. ISSN 14321114. doi: 10.1007/BF00189496.

J.L. Fleming, R.L. Simpson, and W.J. Devenport. An Experimental Study of a Turbulent Wing-Body Junction and Wake Flow. Technical report, Virginia Polytechnic Institute and State University, Blacksburg, 1991.

Song Fu, Zhixiang Xiao, Haixin Chen, Yufei Zhang, and Jingbo Huang. Simulation of wing-body junction flows with hybrid RANS/LES methods. *International Journal of Heat and Fluid Flow*, 28(6):1379–1390, 2007. ISSN 0142727X. doi: 10.1016/j.ijheatfluidflow.2007.05. 007.

F Gand, J.-C Monnier, J.-M Deluc, and A Choffat. Experimental Study of the Corner Flow Separation on a Simplified Junction. *AIAA Journal*, 53(10):2869–2877, 2015. doi: 10.2514/1.J053771.

Fabien Gand, Sébastien Deck, Vincent Brunet, and Pierre Sagaut. Flow dynamics past a simplified wing body junction. *Physics of Fluids*, 22(11):1–16, 2010a. ISSN 10706631. doi: 10.1063/1.3500697.

Fabien Gand, Vincent Brunet, and Sébastien Deck. Experimental and Numerical Investigation of a Wing-Body Junction Flow. *AIAA Journal*, 50(12), 2012. doi: 10.2514/1.J051462.

Fabiend Gand, Vincent Brunet, and Sébastien Deck. A Combined Experimental , RANS and LES Investigation of a Wing Body Junction Flow. *40th Fluid Dynamics Conference and Exhibit*, (July):1–18, 2010b. doi: 10.2514/6.2010-4753.

F. B. Gessner. The origin of secondary flow in turbulent flow along a corner. *Journal of Fluid Mechanics*, 58(01):1, 1973. ISSN 0022-1120. doi: 10.1017/S0022112073002090.

Sina Ghaemi and Fulvio Scarano. Multi-pass light amplification for tomographic particle image velocimetry applications. *Measurement Science and Technology*, 21(12):127002, dec 2010. ISSN 0957-0233. doi: 10.1088/0957-0233/21/12/

127002. URL http://stacks.iop.org/0957-0233/21/i=12/a=127002?key=crossref.71e55f43c09b0c711265ec7ac332e25a.

C Gray and Bernhard Wieneke. Volume self-calibration for stereo-piv and tomographic-piv. 1:135–145, 01 2007.

M A Z Hasan, M J Casarella, and E P Rood. An experimental study of the flow and wall pressure field around a wing-body junction. *Journal of Vibration, Acoustics, Stress, and Reliability in Design*, 108(3):308–314, 1986.

Bryan C. Hinson. *Parametric Exploration of Wing-Body Junction Flow Using Computational Fluid Dynamics*. PhD thesis, Wichita State University, 2012.

Bo Hu, Hua Zhang, Muhammad Yamin Younis, Yan Li, and Malik Shaheryar Raza. Experimental investigation on the transition of separation/attachment in steady laminar juncture flows. *Experiments in Fluids*, 56(4):74, apr 2015. ISSN 0723-4864. doi: 10.1007/s00348-015-1943-5.

Ching-Mao Hung, Chao-Ho Sung, and Chung-Lung Chen. Computation of saddle point of attachment. *AIAA Journal*, 30(6):1561–1569, 1992. ISSN 0001-1452. doi: 10.2514/3.11101. URL http://dx.doi.org/10.2514/3.11101.

J. C. R. Hunt, C. J. Abell, J. A. Peterka, and H. Woo. Kinematical studies of the flows around free or surface-mounted obstacles; applying topology to flow visualization. *Journal of Fluid Mechanics*, 86(01):179, 1978. ISSN 0022-1120. doi: 10.1017/S0022112078001068. URL http://www.journals.cambridge.org/abstract{_}S0022112078001068.

J. C. R. Hunt, A. A. Wray, and P Moin. Eddies, streams, and convergence zones in turbulent flows. In *Center for Turbulence Research, Proceedings of the Summer Program*, number 1970, pages 193–208, 1988. ISBN CTR-S88. doi: CTR-S88.

Constantin Jux. Robotic Volumetric Particle Tracking Velocimetry by Coaxial Imaging and Illumination. Master's thesis, Delft University of Technology, 2017.

K. J. Kang, T. Kim, and S. J. Song. Strengths of horseshoe vortices around a circular cylinder with an upstream cavity. *Journal of Mechanical Science and Technology*, 23(7):1773–1778, 2009. ISSN 1738494X. doi: 10.1007/s12206-009-0602-2.

Richard Keane and Ronald Adrian. Theory of cross-correlation analysis of piv images. 49: 191–215, 01 1992.

Annemiek J Koers. The Anti-Fairing: Reducing Drag in Junction Flows. Master's thesis, Delft University of Technology, 2017.

LaVision GmbH. *FlowMaster - Product Manual*. Document name: 1003005_FlowMaster_D84.pdf, november 2016 edition.

Matthias Macháček. *A quantitative Visualization tool for large wind tunnel experiments ETH Library*. PhD thesis, 2002.

B.W. Melville and S.E. Coleman. *Bridge scour*. Water Resources Publication, 2000.

Koen L L Morias, Giuseppe C A Caridi, Andrea Sciacchitano, and Fulvio Scarano. Statistical Characterization of Helium-Filled Soap Bubbles Tracing Fidelity for PIV. In *18th International Symposium on the Application of Laser and Imaging Techniques to Fluid Mechanics*, Lisbon, July 2016.

RHG Müller and H Flögel. PIV, Investigation of Large Scale Low Speed Condition Flow using. In *Proc. 9th Int. Symposium on Flow Visualization*, pages 218–1 – 218–12, 2000.

RS Norman. *On obstacle generated secondary flows in laminar boundary layers and transition to turbulence.* PhD thesis, Illinois Institute of Technology, 1972.

Y. Okuno, T. Fukuda, and Y. Miwata. Development of Three-Dimensional Air Flow Measuring Method Using Soap Bubbles. *JSAE Rev (Soc Automot Eng Jpn)*, 14(4):50–55, 1993.

Joongcheol Paik, Cristian Escauriaza, and Fotis Sotiropoulos. On the bimodal dynamics of the turbulent horseshoe vortex system in a wing-body junction. *Physics of Fluids*, 19(4), 2007. ISSN 10706631. doi: 10.1063/1.2716813.

Markus Raffel, C E Willert, S T Wereley, and Jürgen Kompenhans. *Particle Image Velocimetry*, volume 79. 2007. ISBN 9783540723073. doi: 10.1007/978-3-540-72308-0.

Edwin P. Rood. *Experimental Investigation of the Turbulent Large Scale Temporal Flow in the Wing-Body Junction.* PhD thesis, The Catholic University of America, 1984.

Ralf Rudnik, Martin Sitzmann, and Jean-luc Godard. Experimental Investigation of the Wing-Body Juncture Flow on the DLR-F6 Configuration in the ONERA S2MA Facility. *AIAA Journal*, (June):1–26, 2009. ISSN 10485953. doi: doi:10.2514/6.2009-4113.

S. Ryu, M. Emory, G. Iaccarino, A. Campos, and K. Duraisamy. Large-Eddy Simulation of a WingBody Junction Flow. *AIAA Journal*, pages 1–12, 2016. ISSN 0001-1452. doi: 10.2514/1.J054212.

M. Samimy and S. K. Lele. *Motion of particles with inertia in a compressible free shear layer.* PhD thesis, aug 1991. URL http://aip.scitation.org/doi/10.1063/1.857921.

Kuo Ching San, Ying Zong Lin, and Shun Chang Yen. Effects of sweep angles and angles of attack on junction-flow patterns. *Journal of Marine Science and Technology (Taiwan)*, 22 (2):204–210, 2014. ISSN 10232796. doi: 10.6119/JMST-013-0325-1.

F Scarano. Tomographic PIV: principles and practice. *Measurement Science and Technology*, 24(1):012001, 2013. ISSN 0957-0233. doi: 10.1088/0957-0233/24/1/012001.

Fulvio Scarano, Sina Ghaemi, Giuseppe Carlo Alp Caridi, Johannes Bosbach, Uwe Dierksheide, and Andrea Sciacchitano. On the use of helium-filled soap bubbles for large-scale tomographic PIV in wind tunnel experiments. *Experiments in Fluids*, 56(2), 2015. ISSN 07234864. doi: 10.1007/s00348-015-1909-7.

Daniel Schanz, Sebastian Gesemann, Andreas Schröder, Bernhard Wieneke, and Matteo Novara. Non-uniform optical transfer functions in particle imaging: calibration and application to tomographic reconstruction. *Measurement Science and Technology*, 24(2): 024009, 2013a. ISSN 0957-0233. doi: 10.1088/0957-0233/24/2/024009. URL http://stacks.iop.org/0957-0233/24/i=2/a=024009.

Daniel Schanz, Andreas Schröder, Sebastian Gesemann, Dirk Michaelis, and Bernhard Wieneke. Shake The Box: A highly efficient and accurate Tomographic Particle Tracking Velocimetry (TOMO-PTV) method using prediction of particle positions. *10th International Symposium on Particle Image Velocimetry - PIV13. Delft, The Netherlands, July 1-3.*, pages 1–13, 2013b.

Daniel Schanz, Andreas Schröder, and Sebastian Gesemann. 'Shake The Box' - a 4D PTV algorithm: Accurate and ghostless reconstruction of Lagrangian tracks in densely seeded flows. *17th International Symposium on Applications of Laser Techniques to Fluid Mechanics*, pages 7–10, 2014.

Daniel Schanz, Sebastian Gesemann, and Andreas Schröder. Shake-The-Box: Lagrangian particle tracking at high particle image densities. *Experiments in Fluids*, 57(5):1–27, 2016. ISSN 07234864. doi: 10.1007/s00348-016-2157-1. URL "http://dx.doi.org/10.1007/s00348-016-2157-1".

Hermann Schlichting, Klaus Gersten, Egon Krause, and Herbert Oertel. *Boundary-layer theory*, volume 7. Springer, 1955.

Andreas Schröder, Reinhard Geisler, Gerrit E Elsinga, Scarano Fulvio, and Uwe Dierksheide. Investigation of a turbulent spot and a tripped turbulent boundary layer flow using time-resolved tomographic PIV. 2007. doi: 10.1007/s00348-007-0403-2. URL https://link.springer.com/content/pdf/10.1007{%}2Fs00348-007-0403-2.pdf.

R.G. Schwind. *Three Dimensional Boundary Layer Near a Strut*. GTL report. Massachusetts Institute of Technology, 1962.

Andrea Sciacchitano. *Uncertainty quantification in particle image velocimetry and advances in time-resolved image data analysis*. PhD thesis, Delft University of Technology, 2014.

S. Scott Collis, Ronald D. Joslin, Avi Seifert, and Vassilis Theofilis. Issues in active flow control: theory, control, simulation, and experiment. *Progress in Aerospace Sciences*, 40 (4-5):237–289, may 2004. ISSN 03760421. doi: 10.1016/j.paerosci.2004.06.001. URL http://linkinghub.elsevier.com/retrieve/pii/S0376042104000405.

Mohammed T. Shukri. Experimental Study of Local Scour Depth around Cylindrical Bridge Pier. *International Journal of Civil, Environmental, Structural, Construction and Architectural Engineering*, 11(1), 2017.

Roger L Simpson. Junction Flows. *Annual Review of Fluid Mechanics*, 33(C):415–443, 2001. doi: 0066-4189/01/0115-0415.

Alan A. Thrift and Karen A. Thole. Influence of flow injection angle on a leading-edge horseshoe vortex. *International Journal of Heat and Mass Transfer*, 55(17):4651–4664, 2012. ISSN 00179310. doi: 10.1016/j.ijheatmasstransfer.2012.04.024.

Chengxu Tu, Zhaoqin Yin, Jianzhong Lin, and Fubing Bao. A Review of Experimental Techniques for Measuring Micro- to Nano-Particle-Laden Gas Flows. *Applied Sciences*, 7 (2):120, 2017. ISSN 2076-3417. doi: 10.3390/app7020120.

Owg van Campenhout, M van Nesselrooij, LLM Veldhuis, BW van Oudheusden, and FFJ Schrijer. Flow visualization over drag reducing dimpled surfaces in turbulent boundary layers using Particle Image Velocimetry. In *18th International Symposium on the Application of Laser and Imaging Techniques to Fluid Mechanics*, Lisbon, 2016.

Bas W. Van Oudheusden, Casper B. Steenaert, and Loek M. M. Boermans. Attachment-Line Approach for Design of a Wing-Body Leading-Edge Fairing. *Journal of Aircraft*, 41(2): 238–246, 2004. ISSN 0021-8669. doi: 10.2514/1.353. URL http://arc.aiaa.org/doi/10.2514/1.353.

Miguel R. Visbal. Structure of laminar juncture flows. *AIAA Journal*, 29(8):1273–1282, 1991. doi: https://doi.org/10.2514/3.10732.

X. Wang, H. Zhang, H. Wang, and L. Fu. New 3-D separation structure in juncture flows. *Journal of Beijing University of Aeronautics and Astronautics*, 36(12):1461–1464+1479, 2010.

Q D Wei, J M Wang, G Chen, Z B Lu, and W T Bi. Modification of junction flows by altering the section shapes of the cylinders. *Journal of Visualization*, 11(2):115–124, 2008. ISSN 1343-8875. doi: 10.1007/BF03181926.

Jerry Westerweel and Fulvio Scarano. Universal outlier detection for PIV data. *Experiments in Fluids*, 39(6):1096–1100, 2005. ISSN 07234864. doi: 10.1007/s00348-005-0016-6.

Jerry Westerweel, Gerrit E. Elsinga, and Ronald J. Adrian. Particle Image Velocimetry for Complex and Turbulent Flows. *Annual Review of Fluid Mechanics*, 45(1):409–436, jan 2013. ISSN 0066-4189. doi: 10.1146/annurev-fluid-120710-101204. URL http://www.annualreviews.org/doi/10.1146/annurev-fluid-120710-101204.

B. Wieneke. Volume self-calibration for 3D particle image velocimetry. *Experiments in Fluids*, 45(4):549–556, 2008. ISSN 07234864. doi: 10.1007/s00348-008-0521-5.

Bernhard Wieneke. Iterative reconstruction of volumetric particle distribution. *Measurement Science and Technology*, 24(2):024008, 2013. ISSN 0957-0233. doi: 10.1088/0957-0233/24/2/024008. URL http://iopscience.iop.org/0957-0233/24/2/024008/article/$\delimiter"026E30F$nhttp://stacks.iop.org/0957-0233/24/i=2/a=024008?key=crossref.5e3934ecb319e35681230d09fec6a1f6.

Christian Willert. Stereoscopic digital particle image velocimetry for application in wind tunnel flows High-speed scanning stereoscopic PIV for 3D vorticity measurement in liquids Stereoscopic digital particle image velocimetry for application in wind tunnel flows. *Meas. Sci. Technol. Meas. Sci. Technol*, 8(8):1465–1479, 1997. URL http://iopscience.iop.org/0957-0233/8/12/010.

Xiangnan Xu, Hua Zhang, and Bo Hu. Numerical study of DBD vortex generator and application in junction flow control. *Acta Aeronautica et Astronautica Sinica*, 37(6):1743–1752, 2016. doi: 10.7527/S1000-6893.2016.0006.

Kazuomi Yamamoto, Kentaro Tanaka, and Mitsuhiro Murayama. Effect of a Nonlinear Constitutive Relation for Turbulence Modeling on Predicting Flow Separation at Wing-Body Juncture of Transonic Commercial Aircraft. *30th AIAA Applied Aerodynamics Conference. AIAA Paper 2012-2895*, (June), 2012. doi: 10.2514/6.2012-2895.

Md Yamin Younis, Hua Zhang, Reiwei Zhu, and Zaka Muhammad. Horseshoe vortex control using streamwise vortices. *Procedia Engineering*, 126:139–144, 2015. doi: 10.1016/j.proeng. 2015.11.196.

Muhammad Yamin Younis, Hua Zhang, Bo Hu, Zaka Muhammad, and Saqib Mehmood. Investigation of different aspects of laminar horseshoe vortex system using PIV. *Journal of Mechanical Science and Technology*, 28(2):527–537, feb 2014. doi: 10.1007/ s12206-013-1120-9.

Hua Zhang, Muhammad Yamin Younis, Bo Hu, Hong Wang, and Xuee Wang. Investigation of attachment saddle point structure of 3-D steady separation in laminar juncture flow using PIV. *Journal of Visualization*, 15(3):241–252, 2012. ISSN 13438875. doi: 10.1007/ s12650-012-0133-2.

Appendix A

Momentum deficit in larger area

It is discussed in section that the calculated momentum deficit encloses only the wake of the HSV. In this way, it only accounts for the effects derived from the HSV. However, if the drag force exerted on the model is interested, a larger integration area should be considered. Hence, the momentum deficit is calculated for other regions, shown in figure A.1, and the corresponding momentum deficit, normalised with $\frac{1}{2}\rho U_\infty^2 S$ is displayed in table A.2, denoted as drag coefficient (C_d). The calculated values are represented as fraction of the clean configuration as well in the same table. S is the integration area of the different regions, summarized in table A.1. It can be see that the ratio of the drag coefficient to the reference case increases with larger integration region. In the end, the antifairing has a lower drag reduction effect than the discussed value in the results chapter.

Table A.1: Surface area of the various integration regions.

Region	A	B	C	D
Area $[cm^2]$	13.34	15.24	31.23	55.03

Table A.2: Drag coefficient of the wake and the relative value to the clean configuration for the different control devices and integration area.

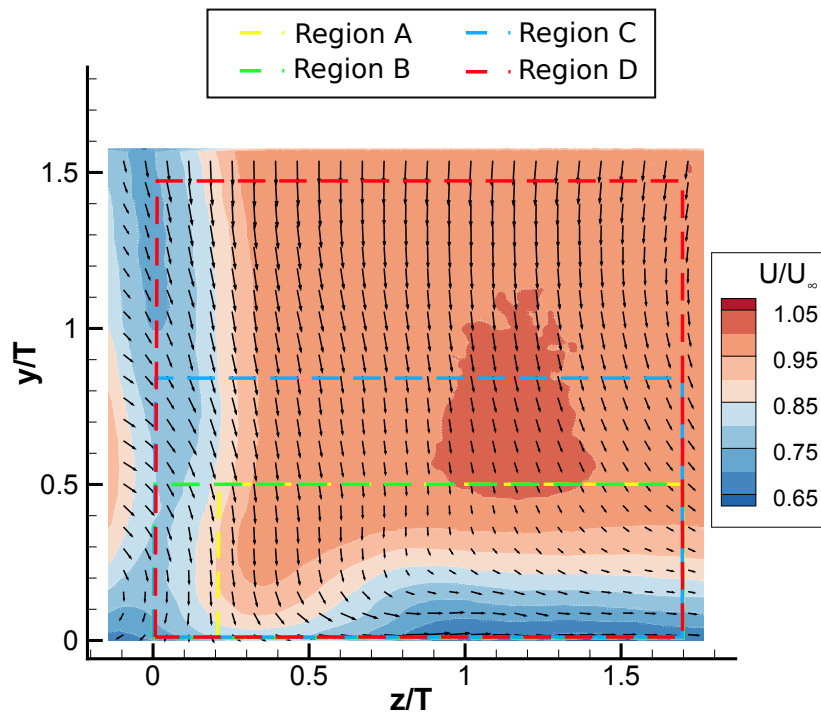|	C_d				Relative to the clean configuration			
	Region				Region			
Configuration	A	B	C	D	A	B	C	D
Clean	0.0222	0.0230	0.0144	0.0109	-	-	-	-
Fairing	0.0220	0.0225	0.0144	0.0116	0.99	0.98	1.00	1.06
Series	0.0244	0.0252	0.0159	0.0122	1.10	1.10	1.10	1.11
Spacing 1T	0.0231	0.0244	0.0164	0.0131	1.04	1.06	1.14	1.20
Spacing 1.5T	0.0239	0.0246	0.0162	0.0125	1.08	1.07	1.12	1.15
Antifairing	0.0183	0.0195	0.0126	0.0101	0.83	0.85	0.87	0.92

Figure A.1: Different integration regions.